Search for the QCD critical endpoint in high-statistics lattice simulations

Alexander Adam

Master Thesis
submitted in partial fulfillment of
the requirements to achieve the degree of
Master of Science

Theoretical particle physics
Faculty of mathematics and natural sciences
Bergische Universität Wuppertal

First supervisor:
Prof. Dr. Jana N. Günther

Second supervisor:
Prof. Dr Szabolcs Borsányi

Submission date:
September 05, 2025

Contents

III Results

IV Appendix

List of Figures

List of Tables

Acknowledgements

I would like to thank my supervisors, Dr. Jana Günther and Dr. Szabolcs Borsanyi, for their continued support and guidance since the beginning of my Master's studies and even before.
In addition, I extend my gratitude to all other members of the weekly meeting group: Dr. Attila Pasztor, Dr. Chik Him Wong, Dr. Ludovica Pirelli, Dr. Paolo Parotto and MSc Piyush Kumar, for their support and help in expanding my knowledge as well as the occasional hints on how to continue.
Furthermore, I would like to thank MSc Piyush Kumar and Dr. Fabian Frech for proofreading parts of this thesis, as well as MEd Anita Frech for her support during the writing phase.

1 Introduction

One of the fundamental interactions in nature is the strong force, which is responsible for the existence of matter as we know it. It is a short-range interaction that holds together the massive hadrons, most importantly protons and neutrons.

Quantum Chromodynamics (QCD) is the theory that explains a wide range of phenomena related to the strong force, including the masses and internal structures of the particles bound by it. It also accounts for color confinement, the mechanism by which quarks and gluons, which carry a type of charge known as color, are bound together to form hadrons [1]. Related to this is the phenomenon of asymptotic freedom, which describes how the strength of the interaction between quarks and gluons decreases as the energy scale increases [2].

As a result, at sufficiently high temperatures, the gluon fields lose the ability to bind hadrons together, leading to the formation of a quarkgluon plasma (QGP), a phase of strongly interacting matter that is thought to have existed during the first microseconds after the Big Bang [3].

Today, such extreme conditions can be recreated in the laboratory through collisions of heavy ions. Collisions of lead and gold nuclei at CERN and Brookhaven National Laboratory in the early 2000s reached temperatures exceeding 10^{12} K, providing direct experimental access to the QGP [4, 5].

Another important aspect of QCD is chiral symmetry breaking, which refers to the spontaneous breaking of a chiral symmetry associated with massless quarks [6]. This phenomenon is essential for understanding hadrons whose masses are significantly larger than the masses of their constituent quarks.

These various aspects come together in the study of the QCD phase diagram, which aims to identify and describe the different phases of strongly interacting matter and the transitions between them.

Of particular relevance to this thesis is the transition between the low-temperature hadronic phase, where a description in terms of hadrons is valid, and the high-temperature phase, which, although still non-perturbative, is dominated by light degrees of freedom. One theoretical approach to study this transition is Lattice QCD , which, at finite temperatures, can provide rigorous constraints on the structure of the QCD phase diagram[7]. However, it faces severe limitations at finite baryon density due to the sign problem.

Lattice QCD has already demonstrated that a broad transition exists between the two aforementioned phases at zero baryon density, occurring at a temperature of approximately $T_{\mathrm{PC}} \approx 157$ MeV [8]. This transition is identified as a crossover [9], marked by the restoration of chiral symmetry.

In the context of phase transitions, in terms of the Ehrenfest classification [10], a crossover refers to a smooth and continuous transformation between different phases, without latent heat or singular behavior in thermodynamic quantities. An everyday analogy is the gradual melting of butter. This stands in contrast to more abrupt transitions, such as first-order and second-order phase transitions. A first-order transition is characterized by a discontinuity in the first derivatives of the free energy and involves latent heat and phase coexistence. A second-order transition, or critical point, is defined by the continuity of the first derivatives but a divergence in the second derivatives and is governed by universal critical exponents [11].

At finite baryon density, it is believed that the crossover transition eventually turns into a first-order transition, implying the existence of a critical point marking this change [12] . Direct investigation of this critical endpoint via lattice QCD is currently hindered by the sign problem [13].

This thesis focuses on one approach to detecting possible signals of the chiral critical endpoint by using lattice QCD to extract information at small baryon densities, where simulations are still feasible, and then extrapolating these results. The extrapolation is based on the theory developed by Lee and Yang, which describes phase transitions through the analysis of the partition function and its singularities in finite systems. This theory was originally introduced in the 1950s and applied to the well-known Ising model [14, 15]. It was later extended by Fisher in the 1970s, leading, among other developments, to the concept of Fisher zeros [16].

In recent years, the Bielefeld-Parma collaboration has applied the Lee-Yang theory, combined with a mapping between the Ising model and QCD, to perform extrapolations toward the critical endpoint using lattice data. Specifically, they employed a Multi-Point Padé ansatz, which is a rational function constructed from polynomials and fitted simultaneously at multiple points [17, 18]. This approach enables not only the extrapolation of observables but also the crucial determination of the Lee-Yang zeros, as predicted by the Lee-Yang theory.

This work builds on that foundation by introducing a modified ansatz for the extrapolation and carefully incorporating various sources of systematic uncertainty that have not yet been fully addressed. The goal is to assess the feasibility and stability of this method in a more comprehensive manner. To be able to carry out the extrapolation and vary the systematics high statistics lattice QCD simulations are needed.

Furthermore, the simulated data used for this analysis is also employed without the ansatz to search for ripples of the QCD critical point via possible non-Gaussian contributions, as predicted by Stephanov [19].

The thesis is organized into three main parts: the theoretical foundations, the methods based on this theoretical framework, and the results obtained from their application.

Part I

Theory

2 Quantum Chromodynamics (QCD)

Motivated by the introduction, this chapter presents a selected list of relevant topics necessary to understand key aspects of the theory describing the strong force within the Standard Model: Quantum Chromodynamics (QCD). It is primarily based on the lecture notes by S. Borsányi [20], V. Koch [21], and C. Ratti and R. Bellwied [22].

2.1 Quantum field theory primer

Before introducing QCD, the framework that allows for its description should be briefly mentioned, namely quantum field theory (QFT).
QFT is usually written down in the Lagrangian formulation. Starting from the knowledge of classical mechanics, the equations of motion are obtained from the Hamilton's principle $\delta S = 0$ with $S = \int \mathrm{d}t\, L(q, \dot{q}, t)$ leading to the Euler-Lagrange equation

$$\frac{\mathrm{d}}{\mathrm{d}t}\frac{\partial L}{\partial \dot{q}} = \frac{\partial L}{\partial q} \tag{2.1}$$

where L is the Lagrange function and S the action. Going over to field theory, the fields $\phi(x)$ replace the coordinates q, with the derivatives of the fields $\partial_\mu \phi(x)$ replacing the velocities $\dot{q}$. The Lagrange function L is expressed via the integral over the Lagrangian density $\mathcal{L}(\phi, \partial_\mu \phi)$ with the action taking the form

$$S[\phi] = \int \mathrm{d}t\; L = \int \mathrm{d}^4x\, \mathcal{L}(\phi(x), \partial_\mu \phi(x), t) \tag{2.2}$$

The equations of motion are again obtained by demanding that the variation of the action S vanishes, resulting in

$$\frac{\partial \mathcal{L}}{\partial \phi_i} - \partial_\mu \left(\frac{\partial \mathcal{L}}{\partial(\partial_\mu \phi_i)} \right) = 0 \tag{2.3}$$

with the index i labeling different fields.
Performing the canonical quantization or the path integral quantization then leads to two equivalent formulations of QFT.
A fundamental advantage of the Lagrangian formulation is that continuous symmetries of the Lagrangian $\mathcal{L}$ imply conserved currents through Noether's theorem. This means that if $\mathcal{L}$ is symmetric under a transformation of the fields $\phi_i \to \phi_i + \delta\phi_i$, this directly leads to a corresponding conserved current

$$J_\mu = \frac{\partial \mathcal{L}}{\partial \partial_\mu \phi_i} \delta\phi_i \tag{2.4}$$

with $\partial^\mu J_\mu = 0$ and associated conserved charge

$$Q = \int \mathrm{d}^3x\, J_0(x) \quad \text{with} \quad \frac{\mathrm{d}}{\mathrm{d}t} Q = 0. \tag{2.5}$$

Breaking the symmetries with a symmetry breaking term $\mathcal{L}_\mathcal{B}$ implying $\delta\mathcal{L} = \delta\mathcal{L}_\mathcal{B} \neq 0$ leads directly to the non conserved current with $\partial^\mu J_\mu = \delta\mathcal{L}_\mathcal{B}$.

2.2 QCD Lagrange Density

The theory describing the strong interactions namely Quantum Chromodynamics (QCD) has the following Lagrangian

$$\mathcal{L}_{\text{QCD}} = -\frac{1}{4}F^a_{\mu\nu}F^{a,\mu\nu} + \sum_q \psi^i_q[\mathrm{i}\gamma^\mu D^{ij} - m_q]\psi^j_q \tag{2.6}$$

where $\mu, \nu \in \{0, 1, 2, 3\}$ denote space time indices, $i, j \in \{1, 2, 3\}$ are the indices of the three-dimensional color space and $a, b, c \in \{1, ..., 8\}$ denote the indices for the generators of the gauge group $SU(3)$.
ψ^i_q represent the fermionic quark field where q is the flavor index, running for various quark fields: u, d, s, c, t, b.
D_μ is the gauge covariant derivative and couples the quark and gluon fields with a coupling strength g, defined as

$$D^{ij}_\mu = \partial_\mu \delta^{ij} - ig(T^a)^{ij}A^a_\mu. \tag{2.7}$$

Here T_a are the generators of $SU(3)$. An explicit representation of generators can be given by the Gell-Mann matrices with $T_a = \lambda_a/2$.
A^a_μ is the gluonic field in the adjoint representation of the SU(3) gauge group with the dynamics described by the term $-\frac{1}{4}F^a_{\mu\nu}F^{a,\mu\nu}$.
$F^a_{\mu\nu}$ represents the gauge invariant gluon field strength tensor which reads

$$F^a_{\mu\nu} = \partial_\mu A^a_\nu - \partial_\nu A^a_\mu + gf^{abc}A^b_\mu A^c_\nu. \tag{2.8}$$

Because of the non-abelian nature of the group the f_{abc} structure constants are not zero resulting in self-interaction between the gauge fields. This can be seen by expanding the dynamic term:

$$\begin{aligned} -\frac{1}{4}F^a_{\mu\nu}F^{a,\mu\nu} = &-\frac{1}{4}(\partial_\mu A^a_\nu - \partial_\nu A^a_\mu)(\partial^\mu A^{a,\nu} - \partial^\nu A^{a,\mu}) \\ &- gf^{abc}\,\partial_\mu A^a_\nu\, A^{b,\mu}A^{c,\nu} \\ &- \frac{g^2}{4}f^{abc}f^{ade}\,A^b_\mu A^c_\nu A^{d,\mu}A^{e,\nu} \end{aligned}$$

A consequence of this is asymptotic freedom which means the theory is weakly coupled at very short distances or at high energy scales. Thus, at sufficiently high temperatures, gluon fields lose the strength to bind hadrons together.
Lastly the variables m_q represent the mass of the quark with flavor q. Putting everything together QCD has $6 \times 3 \times 4 = 72$ quark field components, since the quark fields come in six flavors, each flavor has three colors and each color has four components corresponding to the four dimensional spacetime.
From the phenomenon known as color confinement follows: At normal conditions, observable particles must be invariant under color transformation, i.e a color singlet with respect to the color group. Using the spinors f_i, g_i, h_i in the fundamental representation , $f_i g_i h_i \epsilon_{ijk}/3!$ denotes such a color singlet. These combinations out of three quarks are called baryons. Another way is to use a quark and an antiquark, then the combination $\bar{f}g$, where $\bar{f}$ is in the complex conjugate representation of the fundamental representation, transforms as a singlet. Such quark-antiquark combinations are called mesons.

2.3 Symmetries

QCD has many symmetries, a relevant selection for this thesis are stated here as well as their implications. Although some might not be exactly realized in nature, associated partially preserved currents still have significant impact.
Starting with a simple global symmetry, each flavor can be transformed independently:

$$q \longrightarrow \exp\bigl(-\mathrm{i}\Theta_q^{\mathrm{V}}\bigr)q, \quad \bar{q} \longrightarrow \bar{q}\exp\bigl(\mathrm{i}\Theta_q^{\mathrm{V}}\bigr) \tag{2.9}$$

with $\Theta_q^{\mathrm{V}} \in \mathbb{R}$ resulting in a vector current. This gives rise to the flavor number conservation as well as the conservation of the baryon number: $B = \frac{1}{3}(n_{\mathrm{q}} - n_{\overline{\mathrm{q}}})$. Another symmetry of massless $\mathcal{L}_{\mathrm{QCD}}$ is

$$q \longrightarrow \exp\bigl(-\mathrm{i}\gamma_5\Theta_q^{\mathrm{A}}\bigr)q, \quad \bar{q} \longrightarrow \bar{q}\exp\bigl(-\mathrm{i}\gamma_5\Theta_q^{\mathrm{A}}\bigr) \tag{2.10}$$

with $\Theta_q^{\mathrm{A}} \in \mathbb{R}$ which would give rise to a axial current if it where not broken by the quantization. This phenomenon is referred to as the $U(1)_A$ axial anomaly, which represents a genuine symmetry breaking, in contrast to the spontaneous breaking discussed later.
Proceeding further, the flavor symmetries are now considered, where it is assumed that N quarks possess degenerate masses. From Table 2.1, it is evident that this assumption cannot be applied to all six quark flavors simultaneously, but may remain valid for specific subgroups.

Name	**Symbol**	**Mass**	B	$Q[e]$	I_3	C	S	T	B'
up	u	2.16 ± 0.07 MeV	$\frac{1}{3}$	$+\frac{2}{3}$	$+\frac{1}{2}$	0	0	0	0
down	d	4.70 ± 0.07 MeV	$\frac{1}{3}$	$-\frac{1}{3}$	$-\frac{1}{2}$	0	0	0	0
strange	s	93.5 ± 0.8 MeV	$\frac{1}{3}$	$-\frac{1}{3}$	0	0	-1	0	0
charm	c	1.2730 ± 0.0046 GeV	$\frac{1}{3}$	$+\frac{2}{3}$	0	$+1$	0	0	0
bottom	b	4.183 ± 0.007 GeV	$\frac{1}{3}$	$-\frac{1}{3}$	0	0	0	0	-1
top	t	172.56 ± 0.31 GeV	$\frac{1}{3}$	$+\frac{2}{3}$	0	0	0	$+1$	0

Table 2.1 Quark flavor properties with masses obtained form the Particle Data Group (PDG) [23]

A clear distinction can be made between the light quarks (up, down, strange) and the heavy quarks (charm, bottom, top). Additionally, the up and down quarks are observed to have particularly close masses. Under the assumption of N_f quarks with the same mass, a N_f dimensional isospin vector ψ can be constructed. The transformation Λ_V

$$\begin{aligned} \Lambda_V : \psi &\longrightarrow \exp(-i\Theta^a T^a)\psi \\ : \bar{\psi} &\longrightarrow \exp(+i\Theta^a T^a)\bar{\psi} \end{aligned} \tag{2.11}$$

leaves the Lagrangian invariant and results in a conserved vector-current $J_\mu^a = \bar{\psi}\gamma_\mu T^a \psi$ where T^a are the generator's of the $SU(N_f)$ and ψ.
In the conservative approximation where the up and down quark masses are taken to be equal ($m_u = m_d$), the number of flavors reduces to $N_f = 2$ giving rise to the $SU(2)$ flavor symmetry. The generators are given by $T_a = \tau_a/2$ where the τ_a are the Pauli matrices. This symmetry is referred to as isospin symmetry. It should be noted that the same approximation may also be applied to spinor fields containing proton (p) and neutron (n) states, or to the pseudoscalar meson triplet consisting of the pions (π^+, π^0, π^-), all of which having simar masses due to $m_u \approx m_d$.
Going further one may also consider N_f quarks to have a mass of zero. To understand why this can be done, one has to take into account $\Lambda_{\mathrm{QCD}} \approx 200$ MeV which is a dimensionful coupling constant of pure QCD. With

respect to it, the up and down quark can approximately be considered to have vanishing quark masses. With this, Λ_A

$$\begin{aligned} \Lambda_A : \psi &\longrightarrow \exp(-i\gamma_5\Theta^a T^a)\psi \\ : \bar{\psi} &\longrightarrow \bar{\psi}\exp(-i\gamma_5\Theta^a T^a) \end{aligned} \tag{2.12}$$

becomes a axial-vector symmetry. To see that symmetry indeed requires the absence of any mass term, the following shows how Λ_A effects such a term:

$$\bar{\psi}\psi \xrightarrow{\Lambda_A} \bar{\psi}\psi - 2i\Theta\big(\bar{\psi}T\gamma_5\psi\big) + \mathcal{O}(\Theta^2). \tag{2.13}$$

In addition to being explicitly broken by the non-zero quark masses ($m_u \neq 0, m_d \neq 0$) observed in nature, this symmetry is also spontaneously broken. This means it is a symmetry of the Lagrangian that is not realized in the ground state, leading to the formation a quark condensate $\langle\bar{q}q\rangle \neq 0$.
This symmetry is referred to as *chiral symmetry* and the condensate is correspondingly called the *chiral condensate*. To see why this is the case on can decompose the spinor ψ into left and right components:

$$\begin{aligned} \psi_L = P_L\psi = \frac{1}{2}\left[1-\gamma_5\right]\psi \\ \psi_R = P_R\psi = \frac{1}{2}\left[1+\gamma_5\right]\psi \end{aligned} \tag{2.14}$$

with $\psi = \psi_L + \psi_R$. The chiral condensate can then be written as

$$\langle\bar{\psi}\psi\rangle = \langle\bar{\psi}_L\psi_R + \bar{\psi}_R\psi_L\rangle. \tag{2.15}$$

With regards to this parametrization the Lagrangian is invariant under two separate rotations:

$$\begin{aligned} \psi_L &\longrightarrow e^{-\mathrm{i}\frac{\tau^a}{2}\theta_{La}}\psi_L \\ \psi_R &\longrightarrow e^{-\mathrm{i}\frac{\tau^a}{2}\theta_{Ra}}\psi_R. \end{aligned} \tag{2.16}$$

Putting everything together the symmetry group of QCD with $m_u = m_d = 0$, excluding the $U(1)_A$ axial anomaly, is

$$SU(2)_L \times SU(2)_R \times U(1)_V. \tag{2.17}$$

Since the Λ_V and Λ_A transformations are simultaneous transformation of ψ_L and ψ_R with $\theta_L = \theta_R$ and with $\theta_L = -\theta_R$, respectively, the symmetry group can also be written as

$$SU(2)_V \times SU(2)_A \times U(1)_V \tag{2.18}$$

2.3.1 Center Symmetry

In addition to the chiral symmetry described above, there is another symmetry relevant to the later discussion of the QCD phase diagram. In the pure gluonic theory (or in QCD where the quark masses are taken to infinity) equivalent to pure SU(N) Yang-Mills (YM) theory with N=3 there also exist a $\mathbb{Z}_\mathbb{N}$ center symmetry. To observe the emergence of the center symmetry, the Kubo-Martin-Schwinger (KMS) condition must be recalled:

$$\phi(\vec{x}, 0) = \pm\phi(\vec{x}, \beta), \tag{2.19}$$

where the + sign applies to bosonic fields such as gluons, while the − sign applies to fermionic fields such as quarks. Here, β denotes the temporal extent, which is equal to the inverse of the temperature under

consideration, $\beta = 1/T$.
To ensure the periodicity of A_μ, the general gauge transformations

$$A_\mu \longrightarrow \Omega\,(A_\mu + \partial_\mu)\,\Omega^\dagger \tag{2.20}$$

must obey the KMS condition, i.e.

$$\Omega(\vec{x}, x_4 + \beta) = h\,\Omega(\vec{x}, x_4), \tag{2.21}$$

where h is required to commute with all elements $\Omega \in SU(N)$. This constraint implies that h must belong to the center of $SU(N)$. The center elements h can be written explicitly as

$$h = \exp\left(\frac{2\pi i n}{N}\right) \mathbb{1}_N, \tag{2.22}$$

with $n \in \{1, \ldots, N\}$ and $\mathbb{1}_N$ representing the $N \times N$ identity matrix.
The center symmetry is explicitly broken when quarks are introduced. The quark fields transform as

$$\psi \longrightarrow \Omega\psi, \tag{2.23}$$

but obey the minus sign in the KMS condition, which enforces the boundary condition

$$\psi(\vec{x}, x_4 + \beta) = -\psi(\vec{x}, x_4). \tag{2.24}$$

Under the twisted transformation, these fields transform as

$$\psi(\vec{x}, x_4 + \beta) = g(\vec{x}, x_4 + \beta)\psi(\vec{x}, x_4 + \beta) = -z\,g(\vec{x}, x_4)\psi(\vec{x}, x_4) = -z\,\psi(\vec{x}, x_4), \tag{2.25}$$

which leads to the condition $z = 1$. Therefore, the center symmetry disappears once quarks are introduced [24].
In the absence of fermions, the center symmetry is a symmetry of the ground state, while it is spontaneously broken at high temperatures. The breaking also has a profound impact which will become relevant in following section 2.4 but should also be mentioned here:
If the symmetry is unbroken, the energy of an isolated color charge is infinite, meaning the potential energy of e.g. a particle and antiparticle pair diverges to infinity as they separate. If however the symmetry is spontaneously broken, the potential energy is finite, and a the particle antiparticle pair can be separate [25]. To understand why this is the case, the following observable can be constructed

$$\Phi(\boldsymbol{x}) = \frac{1}{N}\mathrm{tr}\,\mathcal{P}\exp\left[\int_0^\beta dx_4\,A_4(\boldsymbol{x}, x_4)\right], \tag{2.26}$$

known as the *Polyakov loop*, which is sensitive to the transformation: $\Phi(\boldsymbol{x}) \to z\Phi(\boldsymbol{x})$. It has a non-vanishing expectation value $\langle\Phi\rangle \neq 0$ if the $Z(N_c)$ center symmetry is broken and vanished if it is unbroken.
With the the following proportionality [26]

$$e^{-\beta F_q} \propto \langle\Phi\rangle \tag{2.27}$$

where F_q is the free energy of a quark it directly follows that the free energy is infinite iff the Polyakov loop expectation value is zero.

2.3.2 Roberge-Weiss symmetry

Another discrete symmetry of QCD can be revealed when an imaginary chemical potential is introduced into the partition function.

$$Z(\theta) = Z(T, \mu = i\theta T) = \mathrm{Tr} e^{-\hat{H}\beta + i\theta\hat{N}} \tag{2.28}$$

with

$$\hat{N} = \int d^3x \; \psi^\dagger \psi \tag{2.29}$$

being the fermion number operator. With this notation it is clear there that the partition function $Z(\theta)$ is periodic with a period of 2π, as $\exp(2\pi\mathrm{i}) = 1$. This symmetry $\hat{\mu} \longrightarrow \hat{\mu} + 2\pi\mathrm{i}$ is called the symmetry of the free fermion partition function. However $Z(\theta)$ is also periodic with a period of $2\pi/N_C$, which can be shown by writing the partition function in the functional integral representation [27]:

$$Z(\theta) = \int \mathcal{D}\psi \, \mathcal{D}\bar{\psi} \, \mathcal{D}A_\mu \exp\left(- \int_0^\beta \mathrm{d}\tau \int \mathrm{d}^3x \left[\bar{\psi}(\gamma D - m)\psi - \frac{1}{4}F^2 - i\frac{\theta}{\beta}\psi^\dagger\psi \right] \right) \tag{2.30}$$

with boundary conditions following from KMS, for the quarks explicitly taking the form

$$\psi(\vec{x}, \beta) = -\psi(\vec{x}, 0). \tag{2.31}$$

The dependence of the partition function on θ can be removed from the action and incorporated into the boundary conditions by the transformation:

$$\psi(\vec{x}, \beta) \longrightarrow e^{2\pi\mathrm{i}\tau\theta/\beta}\psi(\vec{x}, \beta). \tag{2.32}$$

Of relevance is here is the term in the action

$$\bar{\psi}\gamma D\psi = \bar{\psi}(\gamma^0 D_0 + \gamma^i D_i)\psi \tag{2.33}$$

as the first term of $\not{D}$ leads to a non trivial addition to the action under the transformation:

$$\begin{aligned}
\bar{\psi}\gamma^0 D_0\psi &\longrightarrow e^{-\mathrm{i}\theta T\tau}\bar{\psi}\gamma^0(\partial_0 - igA_0)e^{\mathrm{i}\theta T\tau}\psi \\
&= e^{-\mathrm{i}\theta T\tau}\bar{\psi}\gamma^0\left[\partial_0(e^{\mathrm{i}\theta T\tau}\psi) - \mathrm{i}gA_0 e^{\mathrm{i}\theta T\tau}\psi\right] \\
&= e^{-\mathrm{i}\theta T\tau}\bar{\psi}\gamma^0\left[e^{\mathrm{i}\theta T\tau}\partial_0\psi + (\mathrm{i}\theta T)e^{\mathrm{i}\theta T\tau}\psi - igA_0 e^{\mathrm{i}\theta T\tau}\psi\right] \\
&= \bar{\psi}\gamma^0 D_0\psi + e^{-\mathrm{i}\theta T\tau}\bar{\psi}\gamma^0(\mathrm{i}\theta T)e^{\mathrm{i}\theta T\tau}\psi \\
&= \bar{\psi}\gamma^0 D_0\psi + \mathrm{i}\frac{\theta}{\beta}\psi^\dagger\psi
\end{aligned} \tag{2.34}$$

which removes the direct θ dependence of $Z(\theta)$. $Z(\theta)$ now has the form

$$Z(\theta) = \int \mathcal{D}\psi \, \mathcal{D}\bar{\psi} \, \mathcal{D}A_\mu \exp\left(- \int_0^\beta \mathrm{d}\tau \int \mathrm{d}^3x \left[\bar{\psi}(\gamma D - m)\psi - \frac{1}{4}F^2 \right] \right) \tag{2.35}$$

where the boundary condition now contain the θ dependence:

$$\psi(\vec{x}, \beta) = -e^{\mathrm{i}\theta}\psi(\vec{x}, 0). \tag{2.36}$$

Performing now another change of variable in the integral $\psi \longrightarrow z\psi$ with z in the center of $SU(N)$ leaving the action invariant, and therefore also $Z(\theta)$ but transforming the boundary condition into

$$\psi(\vec{x},\beta) = -e^{\mathrm{i}\theta}e^{2\pi \mathrm{i}k/N}\psi(\vec{x},0) = -e^{\mathrm{i}(\theta+2\pi k/N)}\psi(\vec{x},0). \tag{2.37}$$

Comparing Eq. 2.43 with (2.41 and 2.42), it can be concluded that [27] :

$$Z(T,\theta) = Z\left(T,\theta+\frac{2\pi}{N_c}k\right) \tag{2.38}$$

This is the Roberge-Weiss symmetry. For the three colors of QCD gives this a discrete symmetry $\hat{\mu} \longrightarrow \hat{\mu} + \frac{2\pi \mathrm{i}}{3}$
At the Roberge-Weiss (RW) points $\mu_{\mathrm{B}} = i\mu_{B,I} = \mathrm{i}k\pi T$ where k is an odd integer, QCD has an exact Z_2 symmetry, which is a leftover of the original Z_3 symmetry from the pure gauge case [28]. This symmetry gets spontaneously broken at a critical temperature T_{RW}, further discussed in section 2.4.

2.4 Phase transition and diagram

With the knowledge of the symmetries the phase diagram can be qualitatively described. However before the concept of phase transitions has to be introduced.
We can understand phase transition in the context of statistical physics. The partition function is defined as:

$$\mathcal{Z}(\mu,V,T) = \sum_i \exp\left(\frac{N_i\mu - E_i}{k_B T}\right) \tag{2.39}$$

where the symbols have the usual meanings. The thermodynamic free energy of the system is defined as the logarithm of the partition function (up to a proportionality). Phase transitions are then classified according to the lowest derivative of the free energy that exhibits non-analytic behavior. When a discontinuity appears in the first derivative of the free energy, the transition is called first-order. Conversely, if non-analyticities emerge only in the second or higher derivatives, the transition is characterized as second-order. Furthermore, if the free energy and all of its derivatives are continuous during the change from one phase to another, the transition is termed as an analytical crossover.
Central to phase transitions is the order parameter: an observable that vanishes exactly in one phase while assuming finite non-zero values in the other.
The phase diagram maps different phases of the system where the phase transitions represent the boundaries between these.
In section 2.3 two order parameters where introduced, the chiral condensate $\langle\bar{\psi}\psi\rangle$ and the Polyakov loop $\langle\Phi\rangle$. While these quantities are here referred to as order parameters, it should be noted that they are technically *pseudo-order parameters*, since in nature both symmetries are explicitly broken.
Both have an impact on the hadrons, with the Polyakov loop indication the color confinement of quarks to hadrons and the chiral condensate for example indicating where the pions would be massless in the chiral limit ($m_u = m_d \to 0$).
Figure 2.1 schematically depicts a part of the QCD phase diagram in terms of the temperature T and the baryon chemical potential μ_{B}. The temperature axis is given in units of MeV, where 1 eV corresponds to 11605 K. The baryon chemical potential axis measures the excess of baryonic matter over antimatter. The origin of the diagram corresponds to ($T = 0, \mu_{\mathrm{B}} = 0$). At this point, and more generally in the lower-left region of low temperatures and baryon densities, the system exists as a confined hadron gas. Here, the quarks are confined, and chiral symmetry is both spontaneously and explicitly broken. The phase is dominated by mesons (primarily π-mesons), with other mesons and baryons increasing their prevalence and influence as

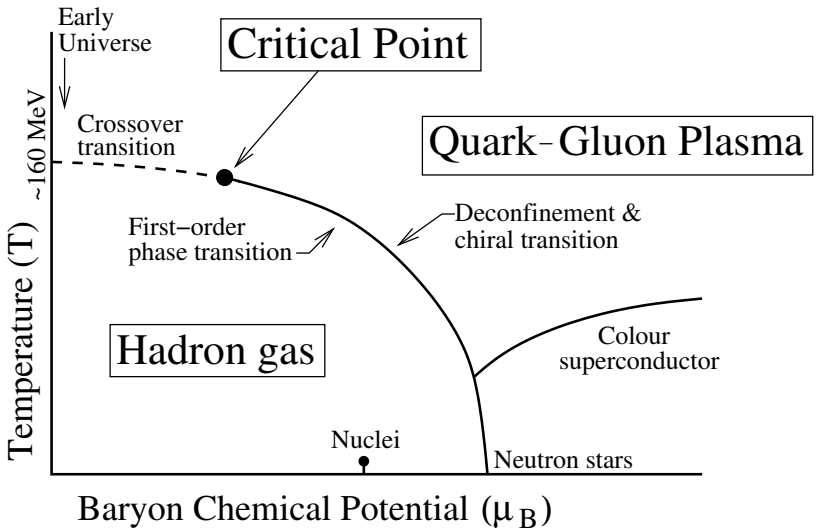

Figure 2.1 Schematic depiction of the QCD phase diagram. Taken from [29]

the temperature rises. This phase can be described by the so called Hadron Resonance Gas, introduced in section 2.7.

Moving up along the temperature axis with zero chemical potential one encounters the transitional crossover region which is difficult to describe or model analytically [30]. Above this crossover and extending well into the phase diagram, the approximation of the system as a gas of free quarks and gluons called quark-gluon plasma (QGP) becomes applicable. In this regime, chiral symmetry is restored in the chiral limit, and therefore one expects a transition from a system with broken chiral symmetry to a chirally symmetric one. Based on these considerations, two lines can be identified as extending from the temperature axis, each corresponding to a different order parameter: the chiral transition line and the (chemical) freeze-out line. The freeze-out line separates the hadronic phase from one dominated by quarks and gluons, namely the quark gluon plasma (QGP), while the chiral transition line marks the restoration of chiral symmetry.

Focusing on the chiral transition line: In QCD with $N_f = 3$ massless quark flavors, the chiral symmetry restoration transition must be of first order. For the case of two massless quarks, the transition can be either second order or first order, depending on the dynamics. In nature, however, the up and down quarks have small but finite physical masses. In this situation, the transition at vanishing baryon chemical potential is a crossover, which many predict to evolve into a first-order transition line via a second-order critical endpoint, extending down to zero temperature. Lattice QCD calculations place the crossover at a pseudo-critical temperature of approximately $T_c \approx 157$ MeV [31, 32], but they cannot confirm the existence of the proposed first-order transition due to the sign problem. Notably, at small to intermediate baryon chemical potentials where lattice data are available, the freeze-out line closely follows the chiral transition line.

The hypothetical QCD critical point is often referred to as the *chiral critical point*, to distinguish it from another well-known (nuclear) critical point: the endpoint of the liquid gas phase transition in nuclear matter. The latter occurs at a significantly lower temperature of 17.9 ± 0.4 MeV [33]. The shape of the chiral transition line can be understood from symmetry and thermodynamic considerations. Charge conjugation symmetry requires that, the partition function is invariant under the simultaneous sign flip in all chemical potentials. This implies that the phase diagram is mirrored around the temperature axis, which in turn requires the transition line to be orthogonal to the axis under the reasonable assumption of continuity and differentiability. On the other hand, the slope of the transition line at finite μ_B is determined by the Clausius-Clapeyron relation,

$$\frac{\mathrm{d}T}{\mathrm{d}\mu_B} = -\frac{\Delta n_B}{\Delta s}, \tag{2.40}$$

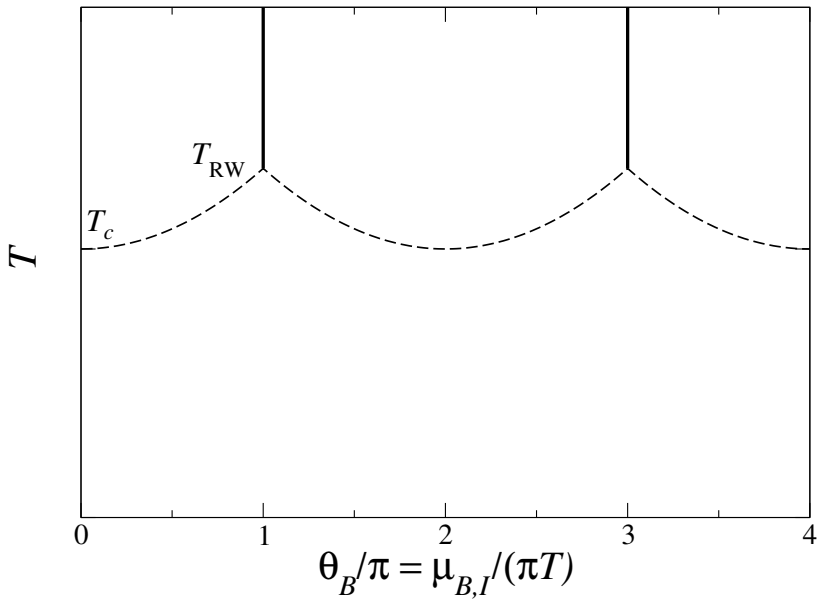

Figure 2.2 Schematic depiction of the QCD phase diagram for a purely imaginary baryon chemical potential. first order line at $\hat{\mu}_{\mathrm{B}} = \mathrm{i}\pi + \mathrm{i}2\pi n$. The vertical lines represent the first order Roberge-Weiss transitions taking place in the high-T regime at $\hat{\mu}_B = \mathrm{i}\pi + \mathrm{i}2\pi n$, while the dashed lines represent the analytic continuation of the pseudo critical line. The figure is taken from [35].

which follows from the equilibrium condition and the relation $dp = s\,dT + n_B\,d\mu_B$ [34]. As the temperature approaches zero, the entropy change Δs vanishes, leading to a large negative slope $dT/d\mu_B$ and thus a nearly orthogonal intercept with the μ_{B} axis.
As a side note for small intermediate chemical potentials, where lattice data are available, the freeze-out line closely follows the chiral transition line
This thesis focuses on the determination of the critical point and the temperature T_{CEP} at which it occurs, which has been a major motivation behind several collider experiments. To achieve this, the properties around the critical point, such as critical scaling, are studied, as well as its close connection to the Lee-Yang edge singularity (see chapter 3).

2.4.1 Imaginary chemical potential

The phase diagram for a purely imaginary baryon chemical potential can also be constructed and is constrained by the Roberge-Weiss (RW) symmetry, under which the chemical potential transforms as $\hat{\mu} \to \hat{\mu} + 2\pi\mathrm{i}/3$ [27]. A schematic depiction based on this symmetry is shown in Figure 2.2.
At high temperature, first-order RW transitions occur at $\hat{\mu}_B = \mathrm{i}\pi/T + \mathrm{i}2\pi n/T$, represented by the vertical lines. The dashed line indicates the analytic continuation of the pseudo-critical line from real chemical potentials. For physical quark masses, the endpoint of these first-order lines is the Roberge-Weiss critical point, located at $T_{\mathrm{RW}} = 208 \pm 5$ MeV [35], which belongs to the 3D-Ising model universality class.
A simplified diagram showing only the first-order Roberge-Weiss transitions was first presented in [27] in 1986, as at the time no evidence for a phase transition as a function of temperature existed.
Since the Roberge-Weiss critical point also belongs to the three-dimensional Ising universality class, a study of it using the Lee-Yang edge singularity, similar to the approach proposed for the chiral critical endpoint, can also be performed [36].

2.5 Equation of State and susceptibilities

The finite-density QCD equation of state can be used to describe the matter in various inserting scenarios, such as heavy-ion collisions or neutron star mergers and is therefore of high scientific interest. To access it, many approaches are available with two being of interest here. First, one may Taylor expand thermodynamic quantities in powers of μ_B/T around $\mu_\mathrm{B} = 0$[37]. Alternatively, simulations can be performed at imaginary chemical potential $\mu_\mathrm{B} = i\mu_B^\mathrm{Im}$, with results analytically continued to real μ_B values [38]. These methods are necessary because direct lattice QCD simulations at high baryon density become infeasible due to the sign problem[13] and QCD itself has not been solved at finite values of μ_B.
Using the Taylor expansion approach the pressure

$$p = T\frac{\partial \ln Z}{\partial V}\bigg|_T \tag{2.41}$$

can be written as a written as a Taylor series in μ_B at zero as [22]:

$$\frac{p(T,\mu_\mathrm{B})}{T^4} = \frac{p(T,0)}{T^4} + \sum_{n=1}^{\infty}\frac{1}{n!}\frac{\partial^n(p/T^4)}{\partial(\frac{\mu_B}{T})^n}\bigg|_{\mu_B=0} \tag{2.42}$$

Introduction the shorthand notation $\hat{\mu}_\mathrm{B} = \mu_B/T$ and $\hat{p} = p/T^4$, leads to

$$\hat{p} = \sum_{n=0}^{\infty} c_n(T)\Big(\frac{\mu_B}{T}\Big)^n \quad c_n = \frac{1}{n!}\frac{\partial^n \hat{p}}{\partial \hat{\mu}_B^n} \tag{2.43}$$

where the coefficients c_n can be calculated on the lattice. The equation for $\hat{p}$ can also be written using the susceptibilities of conserved charges χ_n, as they are related by a simple factor of $1/n!$. Due to this the susceptibilities share the same Taylor coefficients the pressure. This means that the calculation of the coefficients $c_n\,(= \chi_n/n!)$ allows for the extrapolation of the pressure and susceptibilities.
If one were to consider not only baryon chemical potentials but also the electric charge and strangeness chemical potentials, the Taylor expansion would take the form

$$\hat{p}(T,\mu_\mathrm{B},\mu_S,\mu_Q) = \sum_{i,j,k}\frac{1}{i!j!k!}\chi_{ijk}^{BQS}\left(\hat{\mu}_B\right)^i\left(\hat{\mu}_Q\right)^j\left(\hat{\mu}_S\right)^k \tag{2.44}$$

with

$$\chi_{ijk}^{BQS} = \frac{\partial^{i+j+k}\left(\hat{p}\right)}{\partial\left(\hat{\mu}_S\right)^i\partial\left(\hat{\mu}_Q\right)^j\partial\left(\hat{\mu}_S\right)^k}. \tag{2.45}$$

2.6 Critical Fluctuations

A possible approach to detect the critical Point in the QCD Phase Diagram are the so called critical fluctuations, first explained in [39] by Stephanov et al. . These refer to non-Gaussian moments (cumulants) of fluctuations induced by a possible QCD critical point, specificly for fluctuations of experimental observables in heavy-ion collisions
This is to be expected if a critical point exist, as it should lead to divergence of the correlation length ξ and of the magnitude of the fluctuations. While the correlation length diverges at the critical point in the thermodynamic limit, experimental and numerical systems exhibit only finite maximal values due to finite time and size considerations in the vicinity of the critical point [40]. The contribution of the critical point to these fluctuation should manifest in a non-monotonic dependence as the critical point is passed [41]. In [19] the contribution of the critical fluctuations (at tree level) to the cumulants of event-by-event particle

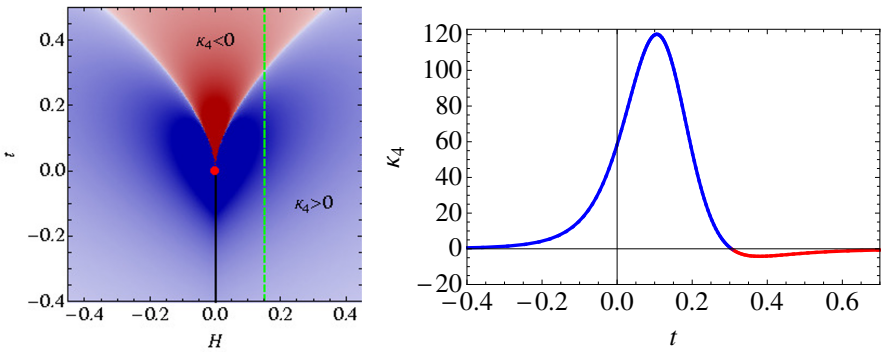

Figure 2.3 In the left is the density plot of the function κ_4(t,H) with the $\kappa_4 < 0$ region shaded in red and the $\kappa_4 > 0$ shaded in blue. On the right is the dependence of κ_4 on t along the vertical dashed green line on the density plot above where this indicates a simple approximation of the freezeout curve. Figures taken from [41].

multiplicities is given as

$$\kappa_2 = \frac{T}{V}\xi^2; \quad \kappa_3 = \frac{2\lambda_3 T}{V}\xi^6; \quad \kappa_4 = \frac{6T}{V}\left[2(\lambda_3\xi)^2 - \lambda_4\right]\xi^8. \tag{2.46}$$

To relate these to the susceptibilities of conserved charges χ_n from section 2.5 the pressure p can be identified with the cumulant generating function resulting in the fact that the χ_n, being derivatives of the pressure, are the non normalized cumulants. Using the relation between the cumulants and the normalized central moments the χ_n can be written as

$$\chi_1 = \frac{M}{VT^3}\ ,\ \chi_2 = \frac{\sigma^2}{VT^3}\ ,\ \chi_3 = \frac{S\sigma^3}{VT^3}\ ,\ \chi_4 = \frac{\kappa\sigma^4}{VT^3} \tag{2.47}$$

with M referring to the mean value, σ^2 the variance, S the skewness and κ the kurtosis. Taking the ratios one can remove volume and temperature:

$$\frac{\chi_3}{\chi_1} = \frac{S\sigma^3}{M} \quad \text{and} \quad \frac{\chi_4}{\chi_2} = \kappa\sigma^2. \tag{2.48}$$

It follows that the ratios have a high sensitivity to a possible critical point manifesting in non monotonic behavior.
In [41], Stephanov illustrated (see Figure 2.3) how, based on a mapping of the Ising critical point onto the QCD critical point, the behavior of the kurtosis is expected to change. In particular, it can be seen that the fourth cumulant, κ_4, becomes negative when the critical point is approached from the crossover side.

2.7 Hadron Resonance Gas (HRG) model

This section covers the most important aspects and formulas for the Hadron Resonance Gas model. As a basis and reference for all equation is the Book [22], which is part of the book series: Lecture Notes in Physics.
The HRG model was first introduced by Rolf Hagedorn in the paper [42] where he begins with "at high energies it is assumed that higher and higher resonances of strongly interacting particles occur and take part in the thermodynamics as if they were particles".
The HRG model therefore based on the fundamental assumption that hadrons and their corresponding resonances can be treated as free, non-interacting particles, enabling the system to be described using simple statistical mechanics, specifically via the ideal (quantum) gas partition function. Mesons and bosons are also treated separately, with regards to their bosonic/fermionic statistics.
Skipping over further historical motivation and derivations, the logarithm of the partition function can be

written as the sum of all hadrons and resonances, of one-particle, ideal quantum gas partition functions:

$$\ln Z^{\mathrm{HRG}}(T,V,\mu) = \sum_{\text{particle } i} \ln Z_i(T,V,\mu). \tag{2.49}$$

The individual partition functions take the form:

$$\ln Z_i(T,V,\mu) = \frac{V g_i T}{2\pi^2} \sum_{N=1}^{\infty} \frac{(\pm 1)^{N+1} \lambda_i^N}{N^2} m_i^2 K_2\left(\frac{N m_i}{T}\right) \tag{2.50}$$

with $+$ for bosons and $-$ for fermions, λ_i representing the particle fugacity

$$\lambda_i(T,\mu) = \exp\left[\frac{B_i \mu_{\mathrm{B}} + S_i \mu_S + Q_i \mu_Q}{T}\right] \tag{2.51}$$

and g_i the spin degeneracy factor for the respective baryons. The first term in the infinite sum for each particle corresponds to the Boltzmann approximation, so called as it corresponds to removing the bosonic and fermionic statistics. In the Boltzmann approximation, with the strangeness μ_S and charge μ_Q chemical potentials set to zero, the baryonic pressure divided by T^4 takes the form

$$\hat{p} = \frac{p_B}{T^4} = \sum_{\text{baryon } i} \frac{g_i}{\pi^2} \left(\frac{m_i}{T}\right)^2 K_2\left(\frac{m_i}{T}\right) \cosh\left(\frac{\mu_B}{T}\right). \tag{2.52}$$

The entire dependence on the used mass spectrum can be absorbed into a function $F(T)$ with pressure taking the form $\hat{p} = F(T) \cdot \cosh(\hat{\mu}_B)$
The fluctuations, defined as the partial derivatives of $\hat{p}$ with respect to $\hat{\mu}_B$, take the form

$$\chi_{2n} = F(T) \cdot \cosh(\hat{\mu}_B), \tag{2.53}$$

$$\chi_{2n+1} = F(T) \cdot \sinh(\hat{\mu}_B), \tag{2.54}$$

with $n \in \mathbb{N}_0$.
Taking ratios of these quantities, as motivated in section 2.6, gives

$$\frac{\chi_{2n}}{\chi_{2m}} = 1 \quad \text{(even/even)}, \tag{2.55}$$

$$\frac{\chi_{2n+1}}{\chi_{2m+1}} = 1 \quad \text{(odd/odd)}, \tag{2.56}$$

$$\frac{\chi_{2n+1}}{\chi_{2m}} = \tanh(\hat{\mu}_B) \quad \text{(odd/even)}, \tag{2.57}$$

$$\frac{\chi_{2n}}{\chi_{2m+1}} = \frac{1}{\tanh(\hat{\mu}_B)} \quad \text{(even/odd)}. \tag{2.58}$$

At $\hat{\mu}_B = 0$, 1 is obtained for (even/even) and (odd/odd) ratios, while vanishing or divergence is observed for (odd/even) and (even/odd) ratios, respectively.

3 Lee-Yang theory

An alternative approach to the study of phase transitions in a system has gained increasing attention in recent years. This method originates from two seminal papers published in 1952 by Tsung-Dao Lee and Chen-Ning Yang [14, 15]. The following discussion is based on these papers, the lecture notes of V. Skokov [43], and the summary chapter in [44].
In this approach, the grand-canonical partition function (introduced in section 2.4) is expressed as

$$Z_{\mathrm{GC}}^{N} = \mathcal{Z}(z, V, T) = \sum_{N_i} Z(N_i, V, T)\, z^{N_i}, \tag{3.1}$$

where $z = \exp(\mu/k_{\mathrm{B}}T)$ is the fugacity and $Z(N_i, V, T)$ denotes the canonical partition function. The latter can be interpreted as the statistical weight associated with the corresponding canonical ensemble.
For real values of μ (or equivalently $\hat{\mu} = \mu/T$), the fugacity z is a positive real number. Furthermore, the canonical partition function is strictly positive, since it consists of a sum of exponentials. As a result, in a finite volume, the sum in Equation 3.1 contains only finitely many positive contributions. Therefore, Z_{GC}^{N} is strictly positive and cannot possess zeros as long as $\hat{\mu}$ is real. Additionally, its logarithm, i.e. the corresponding free energy ($F = T/V \cdot \ln Z$), is an analytic function of the control parameters, which implies that no phase transition can occur in this case. In order for a nonanalyticity to arise, the partition function must necessarily vanish for some value of the control parameter.
However, as argued above, such nonanalytic behavior cannot occur in a finite system and only emerges in the thermodynamic limit, i.e., when the number of constituents $N \to \infty$. Despite this, the partition function, being a polynomial in the fugacity, still possesses zeros at complex values of μ, which are called Lee-Yang zeros (LYZ). Additionally, in a paper by M. E. Fisher [45], inspired by the work of Kortman and Griffiths, the singularities closest to the real axis, i.e. the LYZ, were identified as *Lee–Yang edge* (LYE) singularities.
In the thermodynamic limit, all LYZ condense into continuous lines that form branch cuts, with their endpoints identified as the Lee-Yang edge singularities. A phase transition occurs when such a cut pinches (second order) or crosses (first order) the real axis [46]. In other words, at a critical point, the LYE singularities approach and eventually pinch the real axis, thereby inducing a nonanalyticity in the free energy. This in turn means the LYE singularity is continuously connected to the critical point.
So far all consideration where performed for a given temperature. By tracing the trajectory of this singularity as a function of temperature, one can establish both the existence and the location of the corresponding critical point. The LYE itself is an algebraic branch-point singularity, whose position, when expressed in terms of the appropriate scaling variable, is universal. Furthermore, when the singularity is the closest to the expansion point, it determines the radius of convergence of a series, thereby setting a fundamental limit on expansion-based approaches.
While it is true that every finite-temperature critical point is associated with a pair of LYE singularities, the mere existence of LYE singularities does not necessarily imply the presence of a finite-temperature critical point. This can be demonstrated by considering the one-dimensional Ising model, as discussed in the lecture notes by Skokov [43].
To search for the Lee-Yang zeros (LYZ), one requires observables that encode their location in some way. Natural candidates for such observables are the pressure and its derivatives, since the pressure is defined as

$$p = T \frac{\partial \ln Z(V,T)}{\partial V}\bigg|_{T}, \tag{3.2}$$

which, in the case of a homogeneous system, simplifies to $p = \frac{T}{V} \ln Z = F$. Since F develops a pole at the

LYZ, the pressure and its derivatives with respect to the chemical potential, namely the baryon number fluctuations, also exhibit poles at the LYZ.
The simplest approach is to compute the Taylor expansion of these observables via lattice simulations and estimate the LYZ location from the radius of convergence. However, this procedure faces two major issues: First, the radius of convergence only provides the distance to the closest singularity, not its direction, so multiple estimates from different expansion points must be combined to reconstruct the full location. Second, only a limited number of derivatives can be calculated in practice, which leads to significant uncertainties, both statistical and systematic.
An alternative approach is to adopt a functional form for the baryon number susceptibilities that allows for poles. The simplest option is a rational function, i.e. a ratio of polynomials. This ansatz is known as the Padé ansatz. chapter 5 discusses this method in detail, including how it can be fitted to data, while chapter 4 explains how the input data, namely the Taylor coefficients of the pressure, are generated.
Additional constraints on the ansatz can already be imposed based on the known properties of QCD discussed in chapter 2, such as the Roberge-Weiss symmetry and the successful description of QCD below T_c by the hadron resonance gas (HRG) model. From the HRG perspective, the functional form of the pressure and its even derivatives is well described at leading order by $\cosh(\hat{\mu}_B)$, while the odd derivatives are captured by $\sinh(\hat{\mu}_B)$. The form of pressure has a manifest charge conjugation symmetry since the $\cosh(\hat{\mu}_B)$ is an even function of $\hat{\mu}_B$. It is therefore well motivated to choose the expansion variable for the Padé ansatz as

$$x = \cosh(\hat{\mu}_B) - 1 = \tfrac{1}{2}\hat{\mu}_B^2 + \mathcal{O}(\hat{\mu}_B^4)\,, \tag{3.3}$$

which, in the hadronic phase of interest, ensures faster convergence compared to a naive Taylor expansion in $\hat{\mu}_B$.
Moreover, this parametrization allows the Taylor coefficients to be associated with a clear physical meaning: the first term corresponds to the baryon density, the next order accounts for repulsive baryon-baryon interactions, and in general, the nth term encodes information about genuine n-baryon correlations. Furthermore, the ansatz automatically respects the Roberge-Weiss symmetry, i.e. the periodicity of the QCD free energy as a function of imaginary chemical potential.
It should be noted that in the literature, different strategies for constructing such rational approximations have been pursued. For instance, some works employ a straightforward Padé ansatz without further modifications [17], while others incorporate conformal maps prior to applying the Padé approximation [47].

3.1 Scaling

After the emergence of Lee-Yang zeros (LYZ) and possible strategies for their determination have been discussed, attention is turned to their role in the localization of the critical end point (CEP) through scaling relations. The QCD critical end point is expected to be in the same universality class as the three-dimensional Ising model. For this reason, the Lee-Yang edge singularity is briefly examined within the framework of the Ising model. In this model, two relevant operators are encountered: the energy density and the spin, with the corresponding couplings given by the reduced temperature r and the external magnetic field h, respectively. The critical point in the phase diagram is located at $r = h = 0$. A convenient scaling variable can be introduced as $x = hr^{-1/\beta\delta}$, in terms of which the location of the LYE singularity is simply along the pure imaginary axis [45]:

$$x = \pm \mathrm{i} x_{\mathrm{LY}} = \pm \mathrm{i}(z_c)^{-\beta\delta}. \tag{3.4}$$

The exponents β and δ appearing in x are critical exponents, which can be computed from the scaling dimensions of the local operators σ and ϵ in the conformal field theory that describes the phase transition [48]. With

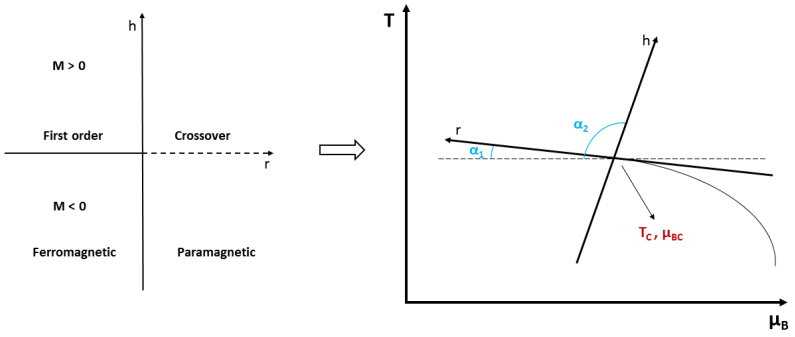

Figure 3.1 Non-universal linear map from Ising variables (r, h) to QCD coordinates (T, μ_B) [50].

the determination of these scaling dimensions given in [49], $(\Delta_\sigma, \Delta_\epsilon) = (0.518148806(24), 1.41262528(29))$, and using the relations

$$\beta = \frac{\Delta_\sigma}{d - \Delta_\epsilon}, \qquad \delta = \frac{d - \Delta_\sigma}{\Delta_\sigma}, \tag{3.5}$$

the product $\beta\delta$ takes the value ≈ 1.5631.

With this knowledge of the three-dimensional Ising model, one can construct a mapping onto QCD such that the critical point of the Ising model corresponds to the QCD critical end point (CEP), and the lines of first-order phase transition and crossover in the Ising model are mapped onto those of QCD.

To relate the two systems, the simplest choice is a linear mapping at the level of the critical point [50]:

$$\frac{T - T_{\mathrm{CEP}}}{T_{\mathrm{CEP}}} = w\left(r\rho \sin\alpha_1 + h \sin\alpha_2\right), \tag{3.6}$$

$$\frac{\mu - \mu_{\mathrm{CEP}}}{T_{\mathrm{CEP}}} = w\left(-r\rho \cos\alpha_1 - h \cos\alpha_2\right). \tag{3.7}$$

The effect of this mapping is illustrated in Figure 3.1. Here, T_{CEP} and μ_{CEP} denote the location of the QCD critical point, while α_1 and α_2 are the angles that the r- and h-axes make with respect to the constant-temperature line in the QCD phase diagram. The parameters w and ρ act as scale factors, providing the overall normalization as well as the relative scaling between r and h.

It is also common to express the map in the inverse direction, i.e., from QCD variables to Ising variables [17, 47]:

$$r = A_r\,\Delta T + B_r\,\Delta\mu, \tag{3.8}$$

$$h = A_h\,\Delta T + B_h\,\Delta\mu, \tag{3.9}$$

where $\Delta T \equiv T - T_{\mathrm{CEP}}$ and $\Delta\mu \equiv \mu - \mu_{\mathrm{CEP}}$, and A_i, B_i are non-universal constants.

Inserting this mapping into the Ising expression for the location of the LYE singularity, Equation 3.4, yields

$$\begin{aligned} h = \pm \mathrm{i} z_c^{-\beta\delta}\, r^{\beta\delta} \implies \\ \left(A_h\,\Delta T + B_h\,\Delta\mu\right) = \pm \mathrm{i} z_c^{-\beta\delta} \left(A_r\,\Delta T + B_r\,\Delta\mu\right)^{\beta\delta}. \end{aligned} \tag{3.10}$$

Since ΔT and $\Delta\mu$ are small near the CEP and $\beta\delta > 1$, the right-hand side can be approximated as zero in leading order. This immediately gives the leading-order expression for the real part of $\Delta\mu$:

$$\mathrm{Re}(\Delta\mu_{\mathrm{LO}}) = -\frac{A_h}{B_h}\,\Delta T. \tag{3.11}$$

Substituting Equation 3.11 back into Equation 3.10, one finds

$$\Delta T(A_h - A_h) + \mathrm{i}B_h \mathrm{Im}(\Delta\mu_{\mathrm{LO}}) = \pm \mathrm{i} z_c^{-\beta\delta} \Big[\Delta T\Big(A_r - \frac{B_r A_h}{B_h}\Big) + \mathrm{i}\,\mathrm{Im}(\Delta\mu_{\mathrm{LO}})\Big]^{\beta\delta}. \tag{3.12}$$

To expand the parenthesis on the r.h.s the binomial theorem is considers for this case

$$(a+ib)^{\beta\delta} = \sum_{n=0}^{\infty} b^n \mathrm{i}^n\, a^{\beta\delta - n} \binom{\beta\delta}{n} \tag{3.13}$$

leading to the following approximation:

$$(a + \mathrm{i}b)^{\beta\delta} \approx a^{\beta\delta} + \mathrm{i}b a^{\beta\delta-1}\beta\delta - \frac{b^2}{a^{2-\beta\delta}} \frac{\beta\delta(\beta\delta-1)}{2} + ... \tag{3.14}$$

At this stage, the assumption has to be made that the imaginary part of the parentheses is smaller than the real part (i.e., it vanishes more rapidly) in order for the sum to converge and the approximation to remain valid. Isolating the imaginary part and considering only the leading order leads to the following leading-order expression for the imaginary part of $\Delta\mu$:

$$\mathrm{Im}(\Delta\mu_{\mathrm{LO}}) = \frac{1}{B_h}\, z_c^{-\beta\delta} \Big(A_r - \frac{B_r A_h}{B_h}\Big)^{\beta\delta} (\Delta T)^{\beta\delta}. \tag{3.15}$$

Only the term $a^{\beta\delta}$ from the approximation was considered, because the second term $\mathrm{i}\, b\, a^{\beta\delta-1}\, \beta\delta$ does not contribute to the imaginary part (due to the overall pre-factor i). Additionally, the third term scales as $(\Delta T)^{3\beta\delta-2}$, which is of higher order than $(\Delta T)^{\beta\delta}$ since $\beta\delta > 1$, and can therefore be neglected, leading to a self consistent approximation. Together with Equation 3.11, one thus arrives at the scaling relations for the location of the LYE singularity near the CEP:

$$\mathrm{Im}(\mu_{\mathrm{LY}}) = c_1\, (\Delta T)^{\beta\delta}, \tag{3.16}$$

$$\mathrm{Re}(\mu_{\mathrm{LY}}) = \mu_{\mathrm{CEP}} + c_2\, \Delta T, \tag{3.17}$$

where c_1 and c_2 are non-universal constants. Using these approximations, the scaling of the imaginary part of μ_{LY} raised to arbitrary powers can be determined to leading order. Up to the fourth power, one finds

$$\begin{aligned} \mathrm{Im}\,\mu_{\mathrm{LY}}^2 &\sim 2\mu_{\mathrm{CEP}}\ \mathrm{Im}\,\mu_{\mathrm{LY}}, \\ \mathrm{Im}\,\mu_{\mathrm{LY}}^3 &\sim 3\mu_{\mathrm{CEP}}^2\ \mathrm{Im}\,\mu_{\mathrm{LY}} - \big(\mathrm{Im}\,\mu_{\mathrm{LY}}\big)^3, \\ \mathrm{Im}\,\mu_{\mathrm{LY}}^4 &\sim 4\mu_{\mathrm{CEP}}^3\ \mathrm{Im}\,\mu_{\mathrm{LY}} - 4\mu_{\mathrm{CEP}}\ \big(\mathrm{Im}\,\mu_{\mathrm{LY}}\big)^3. \end{aligned} \tag{3.18}$$

Since all of these functions exhibit the same asymptotic scaling behavior close to the critical endpoint, there is no fundamental reason to prefer one over the others. Consequently, four equally valid scaling ansätze can be constructed:

$$\begin{aligned} T - T_{\mathrm{CEP}} &\approx A\, \big(\mathrm{Im}\,\mu_{\mathrm{LY}}\big)^{\frac{1}{\beta\delta}}, \\ T - T_{\mathrm{CEP}} &\approx B\, \big(\mathrm{Im}\,\mu_{\mathrm{LY}}^2\big)^{\frac{1}{\beta\delta}}, \\ T - T_{\mathrm{CEP}} &\approx C\, \big(\mathrm{Im}\,\mu_{\mathrm{LY}}^3\big)^{\frac{1}{\beta\delta}}, \\ T - T_{\mathrm{CEP}} &\approx D\, \big(\mathrm{Im}\,\mu_{\mathrm{LY}}^4\big)^{\frac{1}{\beta\delta}}, \end{aligned} \tag{3.19}$$

with non-universal coefficients A, B, C, D. It should be noted that only these scaling ansätze are considered, while alternatives involving terms such as $(\mu_{\mathrm{LY}}/T)^n$ are excluded, since they would impose $T_{\mathrm{CEP}} \neq 0$.

3.2 Finite-Size Scaling

A more in-depth approach for deriving the scaling relations can be obtained using finite-size scaling (FSS), i.e., by studying how a statistical system changes its behavior as the system size is varied, particularly near the critical points of phase transitions. This chapter is based extensively on the paper by Itzykson, Pearson, and Zuber [51], titled "Distribution of zeros in Ising and gauge models".
To begin, consider the following compact expression for the partition function of the Ising model on a regular lattice of linear dimension L:

$$\sum_{(\sigma)=\pm 1} \exp\left\{\beta \sum_{\langle ij\rangle}(\sigma_i\sigma_j - 1) + h\sum_i(\sigma_i - 1)\right\} = Z_L = \sum_{m=0}^{M}\sum_{n=0}^{N} C_{m,n}\, y^m t^n. \tag{3.20}$$

This abstracts the usual sum over all possible spin configurations by dividing them into classes characterized by a fixed number of spins with $\sigma_i = -1$ and a fixed number of nearest-neighbor pairs with $\sigma_i\sigma_j = -1$. Here M and N denote the total number of sites and bonds in the lattice, respectively, and $C_{m,n}$ counts the number of configurations in each class. The variable y corresponds to the external magnetic field via $y = \exp(-2h)$, and t to the inverse temperature via $t = \exp(-2\beta)$.
Fixing t (i.e., β) makes Z_L a polynomial of degree M in y, with its zeros (roots) referred to as Lee-Yang zeros (LYZ). Conversely, fixing y (i.e., h) makes Z_L a polynomial of degree N in t, with its zeros called Fisher zeros. Assuming the system lies in a region of phase space where the finite lattice exhibits the same scaling behavior as the infinite system (up to rounding effects), well-known scaling relations can be applied [16]. Since Z_L is completely determined by its zeros, these zeros themselves must also obey FSS.
The scaling in this context implies that the Hamiltonian of the system of size L,

$$H_L = H_L^* + K_1 O_1^L + K_2 O_2^L + \dots, \tag{3.21}$$

transforms under a rescaling of the length scale by a factor b as

$$H_{L/b}^* + b^{y_1} K_1 O_1^{L/b} + b^{y_2} K_2 O_2^{L/b} + \dots + \epsilon_0, \tag{3.22}$$

where O_i^l denotes a local operator evaluated on a lattice of size l, ϵ_0 is a constant offset, and the factors $b^{y_i}K_i$ are the scaling variables of the system. From this relation it follows, via the scaling of the free energy, that the partition function scales as

$$Z_L(K_1, K_2, \dots) \overset{L\to L/b}{=} Z_{L/b}(K_1 b^{y_1}, K_2 b^{y_2}, \dots)\, e^{\epsilon_0}. \tag{3.23}$$

Introducing the scaling variables $x_i = K_i L^{y_i}$ and setting $L/b = 1/\lambda$, the following statement about the zeros of Z_L can be made:

$$\text{zeros}[Z_L] = \text{zeros}[Z_{1/\lambda}(K_1 L^{y_1}\lambda^{y_1}, K_2 L^{y_2}\lambda^{y_2}, \dots)e^{\epsilon_0}] = \text{zeros}[Q(x_1, x_2, \dots)], \tag{3.24}$$

where Q is shorthand for $Z_{1/\lambda}$. The prefactor e^{ϵ_0} can be dropped, since it never vanishes and thus does not affect the zeros.
Taking into account only the leading thermal and magnetic operators, i.e. only K_1 and K_2, with respective scaling dimensions $y_t = 1/\nu$ and $y_h = \beta\delta/\nu$, the scaling variables take the form

$$x_t = KL^{1/\nu}, \qquad x_h = hL^{\beta\delta/\nu}, \tag{3.25}$$

with $K = (t^2 - t_c^2)$ measuring the distance to the critical temperature. The condition for the zeros of Z_L then reads

$$Q(x_t, x_h) = Q(KL^{1/\nu}, hL^{\beta\delta/\nu}) = 0. \tag{3.26}$$

Considering now the LYZ, i.e., fixing the temperature, the zeros can be written formally as

$$x_h^2 = f_i(x_t) \quad \Longrightarrow \quad h^2 L^{2\beta\delta/\nu} = f_i(KL^{1/\nu}), \tag{3.27}$$

where f_i denotes the solution for the location of the i-th root depending on x_t. Since Z_L is even in h, the zeros are expressed in terms of h^2.
At $t = t_c$ and for large L, the closest LYZ (the Lee-Yang edge singularity) behaves as

$$h^2 = L^{-2\beta\delta/\nu} f_i(0). \tag{3.28}$$

The original work of Lee and Yang [15] shows, via the famous Yang-Lee circle theorem (see also [52]), that the zeros are distributed along the unit circle $z = \exp(i\theta)$, where $\theta = 2i\beta H$ and H is the (imaginary) magnetic field.
Depending on the temperature, one can distinguish different scenarios. For $t < t_c$, the zeros cross the positive real z-axis at $z = 1$ ($\theta = 0$). For $t > t_c$, there exists a finite gap in the distribution of zeros, with $g(\theta) = 0$ for $|\theta| < \theta_g$. This gap closes exactly at $t = t_c$, i.e., the zeros pinch the axis.
Thus, below t_c a first-order phase transition is present, at t_c a second-order critical point is located, and above t_c no phase transition occurs, all on the real axis of H.
Above t_c, the gap in the distribution of the LYZ translates into imaginary values of the magnetic field, $H = \pm i|H_c(T)|$ at these zeros. Kortman and Griffiths [53] showed that the distribution of zeros near the gap behaves as $(|\theta| - \theta_g)^\sigma$. Fisher [45] then pointed out that the magnetization around the Lee-Yang edge singularity behaves as

$$M - M_c \sim (H - iH_c(T))^\sigma, \tag{3.29}$$

where M_c denotes the critical value of the magnetization.
This then leads, according to [51], to the scaling relation

$$h_i^2 \longrightarrow -C\, K^{2\beta\delta}, \tag{3.30}$$

valid in the limit of large lattice size L or equivalently for fixed L and strong external field (so that $x_t \to \infty$). Inverting this expression, and using the fact that $-1 = \exp(i\pi)$, one obtains for K:

$$K \;=\; e^{\,i\pi/(2\beta\delta)} \left(\frac{h}{\sqrt{C}}\right)^{1/(\beta\delta)}. \tag{3.31}$$

Thus, for nonzero field h, the scaling relation implies that the trajectories of the zeros near the critical point approach the critical temperature along straight lines in the complex plane. Since K measures the (squared and shifted) temperature distance from t_c, the angle at which these trajectories intersect the critical point is given by

$$\psi = \frac{\pi}{2\beta\delta}. \tag{3.32}$$

Reformulation of Equation 3.30 and identifying K with r form the section 3.1 leads to the equation

$$\frac{h}{r^{\beta\delta}} = hr^{-\beta\delta} = -C \tag{3.33}$$

which started the section on the derivation of the scaling relation.

3.3 Roberge-Weiss scaling

Since the Roberge-Weiss critical point introduced in subsection 2.4.1 is also a second-order $\mathbb{Z}_2$ critical point, the scaling of the associated Lee-Yang zeros can be investigated analogously to the procedure already presented for the chiral critical point. Skipping over the derivation and directly quoting the result from [54]:

$$\mathrm{Re}\hat{\mu}_{\mathrm{LY}} = \pm\pi \left(\frac{z_0}{|z_c|}\right)^{\beta\delta} \left(\frac{T_{RW} - T}{T_{RW}}\right)^{\beta\delta}, \tag{3.34}$$

$$\mathrm{Im}\hat{\mu}_{\mathrm{LY}} = \pm\pi, \tag{3.35}$$

it is evident that, in contrast to the scaling of the chiral critical point, the real part of the Lee-Yang zeros is of importance. This is expected, as the imaginary part of the critical point is already known from theory, but it leads to the following leading-order scaling ansatz for the real part, which has exactly the same form as the ansatz used for the imaginary part of the chiral CEP:

$$\mathrm{Re}\mu_{\mathrm{LY}} = c_1 \left(\Delta T\right)^{\beta\delta}. \tag{3.36}$$

Here, ΔT refers to the difference with respect to the Roberge-Weiss transition temperature T_{RW}, which can be extracted from the Lee-Yang zeros using this ansatz.

Part II

Methods

4 Lattice QCD

Lattice gauge theory provides a non-perturbative approach for calculating observables in quantum field theories. In the continuum, such theories have an infinite number of degrees of freedom, namely one per coordinate, of which there are infinitely many. This makes direct numerical simulation impossible. The central idea of lattice QCD is to render the number of degrees of freedom finite by discretizing space-time, introducing a *UV cutoff*, and limiting the system to a finite extent, introducing an *IR cutoff*. This is achieved by placing equally spaced points in a four-dimensional cubic array, referred to as the *lattice*, with lattice spacing denoted by a. The boundaries of the lattice are typically equipped with periodic or anti-periodic boundary conditions (PBC or APBC) according to KMS[55]. Discretization of space-time has important consequences. For example, the differential operator ∂_μ must be replaced by a finite-difference operator, and integrals over the space-time volume must be replaced by sums over all lattice sites. To preserve gauge invariance when transitioning from the continuum to the lattice, *gauge links* $U_\mu(\mathbf{n})$ are introduced. Without these link variables, local gauge transformations would not leave the action invariant. This preservation of gauge invariance constitutes the central principle of any lattice gauge theory (LGT). With this foundation, the geometry of the lattice can be specified: the physical volume is given by $V = (N_s a)^3$, while the temperature is defined as $T = 1/(N_t a)$. The simulations used for the later analysis used a a fixed lattice size of $16^3 \times 8$, corresponding to a physical volume fixed in temperature units to $LT = 2$. Ensembles are generated using rooted staggered fermions with four steps of HEX smearing [56] ("4HEX"), physical quark masses, and the DBW2 gauge action [57]. The 4HEX procedure has been shown to suppress taste-breaking effects more effectively than any other action currently available in the literature [58]. Before quantitative results are extracted, the action is parameterized by tuning the dependence of the bare quark masses on the gauge coupling so that the theory is renormalized in the parameter range of interest. The scale is set using the pion decay constant f_π, as well as a modified version of the Wilson-flow-based method [59].

4.1 Calculation of fluctuations

To see how the quark number susceptibilities and higher cumulants are calculated, the partition function of lattice gauge theory is first written as

$$Z(T,\mu) = \int \mathcal{D}U \, \det \mathbf{M}(U,\mu)\, e^{-S_g(U)}. \tag{4.1}$$

In the case of staggered fermions with 3 flavors, the partition function takes the form

$$Z(T,\mu) = \int \mathcal{D}U \, e^{-S_g} \left(\det M_1\right)^{1/4} \left(\det M_2\right)^{1/4} \left(\det M_3\right)^{1/4}, \tag{4.2}$$

where the fermion matrix with the chemical potential μ is given by [13]

$$M(\mu) = \gamma^\mu D_\mu + m + \mu\gamma_0. \tag{4.3}$$

As discussed in the section on the Roberge-Weiss symmetry, this dependence can also be absorbed into the gauge links through weighted temporal links, leading to

$$U_0(\mu) = e^{\mu} U_0, \qquad U_0^\dagger(\mu) = e^{-\mu} U_0^\dagger. \tag{4.4}$$

The case of $2+1$ staggered fermions is realized by combining the appropriate fermionic determinants.
The fourth root is taken for each fermion determinant because the staggered action generates four degenerate

flavors in the continuum limit, which are then taken care of by rooting.
The derivatives of the fermionic matrices take the form

$$\begin{aligned}\frac{dM}{d\mu}\psi(x) &= \eta_0(x)\left[U_0(x)\psi(x+\hat{0}) + U_0^\dagger(x-\hat{0})\psi(x-\hat{0})\right],\\ \frac{d^2M}{d\mu^2}\psi(x) &= \eta_0(x)\left[U_0(x)\psi(x+\hat{0}) - U_0^\dagger(x-\hat{0})\psi(x-\hat{0})\right],\end{aligned} \tag{4.5}$$

which are relevant since the fluctuations require derivatives of the partition function.
The baryon derivative can be expressed in terms of the flavor derivatives as

$$\frac{d}{d\mu_B} = \frac{1}{3}\partial_u + \frac{1}{3}\partial_d + \frac{1}{3}\partial_s \tag{4.6}$$

Using this relation, the dimensionless baryon susceptibility c_2^B takes the form

$$c_2^B = \frac{1}{VT}\frac{1}{9}\left[\partial_u^2 + \partial_d^2 + \partial_s^2 + 2\partial_u\partial_d + 2\partial_u\partial_s + 2\partial_d\partial_s\right]\log Z. \tag{4.7}$$

Thus, the evaluation of fluctuations requires derivatives of the logarithm of the partition function with respect to all distinct quark flavors. These derivatives, in turn, depend on derivatives of the fermionic matrices.
For convenience, the shorthand notation

$$F = (\partial_i M_i)M_i^{-1}, \qquad S = (\partial_i^2 M_i)M_i^{-1}$$

is introduced. With this, the following expressions are obtained:

$$\begin{aligned}A &= \frac{d}{d\mu}\log(\det M)^{1/4} = \tfrac{1}{4}\mathrm{Tr}F,\\ B &= \frac{d^2}{(d\mu)^2}\log(\det M)^{1/4} = \tfrac{1}{4}\mathrm{Tr}\left[S - F^2\right],\\ C &= \frac{d^3}{(d\mu)^3}\log(\det M)^{1/4} = \tfrac{1}{4}\mathrm{Tr}\left[F - 3SF + 2F^3\right],\\ D &= \frac{d^4}{(d\mu)^4}\log(\det M)^{1/4} = \tfrac{1}{4}\mathrm{Tr}\left[S - 4F^2 - 3S^2 + 12SF^2 - 6F^4\right].\end{aligned} \tag{4.8}$$

By construction, these coefficients are precisely the expansion coefficients of the determinant:

$$\log\det M_j^{1/4}(U, m_j, \hat{\mu}_j) = \log\det M_j^{1/4}(U, m_j, 0) + A_j\hat{\mu}_j + \frac{1}{2!}B_j\hat{\mu}_j^2 + \frac{1}{3!}C_j\hat{\mu}_j^3 + \ldots \tag{4.9}$$

With these expansion coefficients, a general expression for the derivative of an arbitrary observable X can be written, following [60] and its interpretation in [61]:

$$\partial_j\langle X\rangle = \langle XA_j\rangle - \langle X\rangle\langle A_j\rangle + \langle\partial_j X\rangle. \tag{4.10}$$

In particular, if $X = \ln Z$, the required derivatives for the baryon susceptibilities are obtained.
The first derivative is

$$\partial_i \log Z = \frac{1}{Z}\int \mathcal{D}U\,\partial_i e^{-S_{\text{eff}}} = \langle A_i\rangle, \tag{4.11}$$

and by application of the chain rule, the second derivative follows directly:

$$\partial_i\partial_j \log Z = \partial_i\langle A_j\rangle = \langle A_iA_j\rangle - \langle A_i\rangle\langle A_j\rangle + \delta_{ij}\langle B_i\rangle \overset{\mu_i=0}{=} \langle A_iA_j\rangle + \delta_{ij}\langle B_i\rangle. \tag{4.12}$$

Here the term $\langle B_i \rangle$ appears due to the relation $\partial_i A_j = \delta_{ij} B_i$, which follows directly from the expansion of $\log\det M_j^{1/4}(U, m_j, \mu_j)$. The construction of further derivatives and the corresponding higher-order susceptibilities c_n^B follows recursively. These are, however, omitted in the present discussion for reasons of brevity.

To actually determine the configuration-specific expansion coefficients $A_i, B_i, C_i, D_i, ...$ either the traces from Equation 4.8 can be evaluated using random sources or the reduced matrix formalism introduced in [62] can be used. Since the reduced matrix formalism was used in the determination it is briefly stated here. The formalism describes how a dense matrix, with size $(2 \times 3 \times L^3)^2$ can be defined instead of the propagator matrix , a sparse matrix of size $(2 \times 3 \times L^3 \times N_t)^2$, whose eigenvalues still give complete insight into the fermion determinant.

These eigenvalues ξ_i allow for the evaluation of the fermion determinant[63]:

$$\frac{\det M(\hat{\mu}, m, U)}{\det M(0, m, U)} = e^{-3N_s^3 \hat{\mu}} \prod_{i=1}^{6N_s^3} \frac{\xi_i[m, U] - e^{\hat{\mu}}}{\xi_i[m, U] - 1}. \tag{4.13}$$

Taking the fourth root and logarithm leads to

$$\log\det M_j^{1/4}(U, m_j, \hat{\mu}_j) = \log\det M_j^{1/4}(U, m_j, 0) + (-3N_s^3 \hat{\mu}/4) + \frac{1}{4} \sum_{i=1}^{6N_s^3} \log\left[\frac{\xi_i[m, U] - e^{\hat{\mu}}}{\xi_i[m, U] - 1}\right] \tag{4.14}$$

Now taking derivatives with respect to $\hat{\mu}$ at zero leads to the expansion coefficients, by also taking into account Equation 4.9. As an example, a expression of A in terms of eigenvalues ξ_i is obtained by taking the first derivative at $\hat{\mu} = 0$:

$$\begin{aligned}
\frac{\partial}{\partial\hat{\mu}}\bigg|_{\hat{\mu}=0} \log\det M_j^{1/4}(U, m_j, \hat{\mu}_j) &= (-3N_s^3/4) + \frac{1}{4} \sum_{i=1}^{6N_s^3} \frac{\partial}{\partial\hat{\mu}}\bigg|_{\hat{\mu}=0} \log\left[\frac{\xi_i[m, U] - e^{\hat{\mu}}}{\xi_i[m, U] - 1}\right] \\
A &= (-3N_s^3/4) + \frac{1}{4} \sum_{i=1}^{6N_s^3} \left[\left(\frac{-e^{\hat{\mu}}}{\xi_i[m, U] - 1}\right)\left(\frac{\xi_i[m, U] - e^{\hat{\mu}}}{\xi_i[m, U] - 1}\right)^{-1}\right]_{\hat{\mu}=0} \\
A &= (-3N_s^3/T) + \frac{1}{4} \sum_{i=1}^{6N_s^3} \left[\frac{-1}{\xi_i[m, U] - 1}\right]
\end{aligned}$$

With the knowledge that A is purely imaginary, due to charge conjugation, one can take the imaginary part of the r.h.s and multiply it with i to arrive at the final expression for A:

$$A = \frac{\mathrm{i}}{4} \mathrm{Im} \sum_i \frac{1}{(1 - \xi_i)} \tag{4.15}$$

Taking higher derivatives leads to the expressions for B, C, D which are relevant for higher order derivatives of $\ln Z$. The derivation of which are shown in section A.1.

4.2 Complex determinant

An important issue arises when a finite chemical potential is introduced. For $\mu > 0$, the fermion matrix takes the form shown in Equation 4.3, whose determinant directly contributes to the fermionic part of the partition function. Introducing a finite chemical potential therefore favors quarks over anti-quarks, explicitly breaking charge-conjugation symmetry. Since charge conjugation is directly related to complex conjugation, it follows that

$$\det(M(\mu)) \neq \overline{\det(M(\mu))} \qquad (\mu > 0). \tag{4.16}$$

In a more formal way, a finite μ breaks the γ^5-hermiticity, namely:

$$M(\mu)^\dagger = \gamma^5 M(-\mu)\gamma^5, \tag{4.17}$$

which implies

$$\overline{\det(M(\mu))} = \det(M(-\mu)). \tag{4.18}$$

For $\mu > 0$ this directly leads to a complex fermion determinant with a non-vanishing imaginary part.
The necessity of a complex fermion determinant can be illustrated by considering the relation between the expectation value of the Polyakov loop, $\langle\Phi\rangle$, and the free energy of a static color charge or anti-charge, as introduced in subsection 2.3.1. When expressed using the integration measure $d\varpi$, which includes the fermion determinant, as done in [13], one finds

$$\begin{aligned} \langle\Phi\rangle &= \exp\left(-\frac{1}{T}F_q\right) = \int \mathrm{Re}(\Phi)\times\mathrm{Re}(d\varpi) - \mathrm{Im}(\Phi)\times\mathrm{Im}(d\varpi) \\ \langle\Phi^*\rangle &= \exp\left(-\frac{1}{T}F_{\bar{q}}\right) = \int \mathrm{Re}(\Phi)\times\mathrm{Re}(d\varpi) + \mathrm{Im}(\Phi)\times\mathrm{Im}(d\varpi). \end{aligned} \tag{4.19}$$

This shows that a difference in the free energy of a quark and an anti-quark can only arise, as expected for a nonzero chemical potential, if the integration measure is complex; that is, if the fermion determinant is complex. This, however, leads to the important observation that the probabilistic interpretation of the Boltzmann weight is lost, which is required for importance-sampling methods such as the Metropolis algorithm. While taking the real part of the determinant would formally restore a probability interpretation, it introduces oscillations in the path integral, since $\mathrm{Re}(e^{\mathrm{i}\theta}) = \cos(\theta)$.
This oscillatory behavior can be illustrated with the simple example[13]

$$Z(\lambda) = \int_{-\infty}^{\infty} \exp\bigl(-x^2 + \mathrm{i}\lambda x\bigr)\,dx, \qquad \mathrm{Re}\,Z(\lambda) = \int_{-\infty}^{\infty} \exp\bigl(-x^2\bigr)\cos(\lambda x)\,dx. \tag{4.20}$$

Here, an imaginary contribution proportional to λ is added to a standard Gaussian distribution. By symmetry, the real part of Z vanishes for $\lambda > 0$. However, when plotting the actual integrand (see Figure 4.1), it becomes evident that in the numerical evaluation many positive and negative contributions arise, in stark contrast to the smooth case $\lambda = 0$.
This cancellation between oscillating contributions makes the evaluation of Z increasingly difficult for growing λ. The same mechanism underlies the QCD partition function Z_{QCD}, where the complex fermion determinant at $\mu > 0$ leads to the so-called *sign problem*, rendering direct simulations at finite chemical potential unfeasible.
A further manifestation of the sign problem can be observed in the computation of fluctuations. Figure 4.2 shows that higher-order fluctuations involve an increasing number of terms, many of which contribute with alternating signs. The ratio of positive to negative terms rapidly approaches 50%, which demonstrates how the physically relevant result emerges only as a small difference of two large contributions. This highlights the exponentially growing computational cost required to determine higher-order fluctuations reliably.

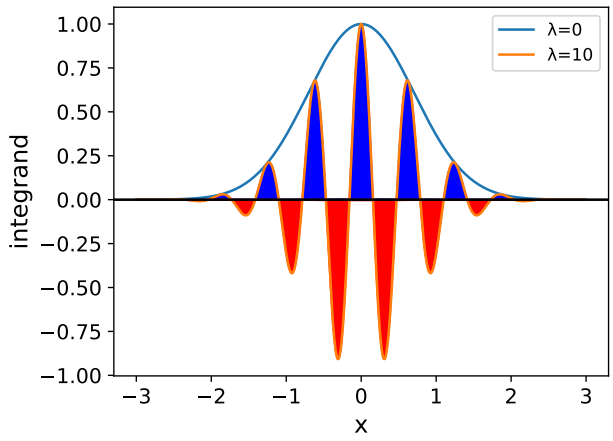

Figure 4.1 Schematic illustration of the sign problem, showing the integrand of Equation 4.20 for $\lambda = 0$ and $\lambda > 0$. Inspired by [64].

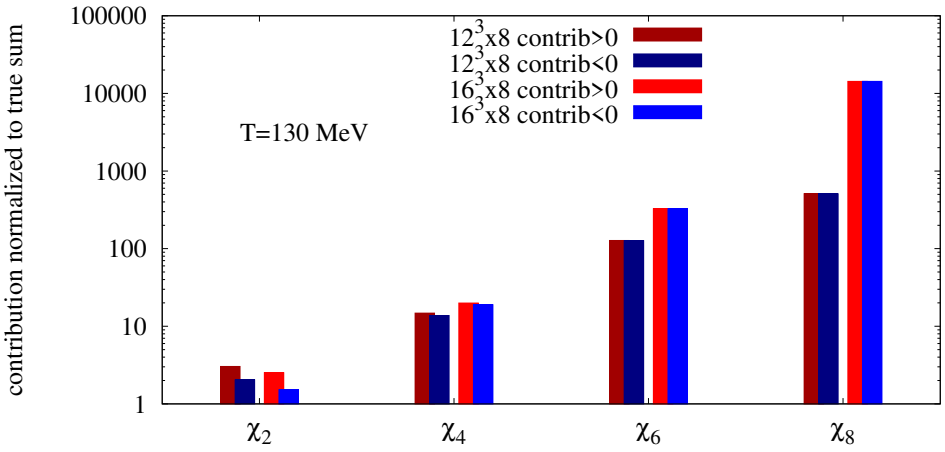

Figure 4.2 Cancellations between positive (red) and negative (blue) terms for the Taylor coefficients χ_n up to eighth order at $T = 130$ MeV. Results are shown for two volumes ($12^3 \times 8$ and a larger reference volume) to illustrate the volume dependence of the cancellations. Figure and caption adapted from [65].

5 Pade Fits

The motivation for employing rational approximations has already been discussed in chapter 3. In particular, Padé approximants allow the direct incorporation of Taylor series coefficients while providing a more powerful framework for studying functions with non-analytic features. Unlike ordinary Taylor expansions, rational functions are capable of capturing non-analyticities, which makes them especially suitable for the study of critical phenomena.

The use of Padé approximations in the context of phase transitions dates back to the pioneering work of M. E. Fisher in 1965. Since then, Padé approximants have become a standard tool in many areas of physics and applied mathematics. A thorough overview of Padé approximations, along with numerous applications and insights, is provided in [44], while a comprehensive introduction can be found in the classic reference [66]. This chapter does not attempt to reproduce these complete treatments. Instead, it summarizes and derives only the essential aspects of Padé approximations that are relevant for the present work, with a focus on their practical construction and application.

5.1 Construction

Beginning with the notation used in this thesis before beginning with the construction from Taylor coefficients: A [m,n]-Padé is a rational function with the numerator being a polynomial of O(m) and denominator a polynomial of O(n).
With one coefficient normalized to one, namely the leading coefficient of the denominator, the $[m, n]$-Padé has $m+n+1$ degrees of freedom. Therefore, at least a Taylor expansion up to $\mathcal{O}(x^{m+n})$ is required for the determination of theses free coefficients. When the degrees of freedom match, the Padé coefficients can be obtained from the Taylor coefficients through a algebraic transformation. When more Taylor coefficients are available than required for the Padé approximation, the coefficients can be determined via a least-squares fit, which also provides an estimate of the goodness of fit. In either approach, the necessary Taylor coefficients may be obtained from multiple distinct points, resulting in a multi-point Padé approximation rather than the conventional single-point Padé.

5.1.1 Algebraic transformation

To begin the construction, Equation 5.1 depicts both a Taylor series expansion truncated at order $\mathcal{O}(x^l)$ and a general [m,n]-Padé approximation

$$T_l(x) = \sum_{i=0}^{l} c_i x^i \qquad \text{Padé}[m,n] : R_n^m(x) = \frac{P_m(x)}{1+Q_n(x)} = \frac{\sum_{i=0}^{m} a_i x^i}{1+\sum_{i=1}^{n} b_i x^i} \tag{5.1}$$

For simplicity, the expansion point is taken to be zero in this construction. A nonzero expansion point would introduce only linear factors with respect to both the Taylor and Padé coefficients, which are accounted for in the actual implementation.
The algebraic transformation can be constructed by equating the Taylor series $T_l(x)$ to the Padé approximation of the form $P_m(x)/(1+Q_n(x))$ which can be rearranged as

$$P_m(x) - T_l(x) \cdot Q_n(x) = T_l(x). \tag{5.2}$$

The coefficients of the Padé approximation are then determined by matching the appropriate number of derivatives at the expansion point of the Taylor series. This approach to the determination is called approximation through order.
Carrying out this procedure leads to the following equations for the first three derivatives [44]:

$$\begin{aligned}
P_m(x) - T_l(x)Q_n(x)\Big|_{x=x_0} &= T_l(x_0) \\
P_m^{(1)}(x) - T_l^{(1)}(x)Q_n(x) - T_l(x)Q_n^{(1)}(x)\Big|_{x=x_0} &= T_l^{(1)}(x_0) \\
P_m^{(2)}(x) - T_l^{(2)}(x)Q_n(x) - 2T_l^{(1)}(x)Q_n^{(1)}(x) - T_l(x)Q_n^{(2)}(x)\Big|_{x=x_0} &= T_l^{(2)}(x_0)
\end{aligned} \tag{5.3}$$

Since these equations involve only polynomial expressions, at most multiplied by constants from the chain rule and Taylor coefficients $T_l^{(n)}(x_0)$, the entire left-hand side remains linear in the Padé coefficients. This linearity permits representation as a matrix equation:

$$M \cdot \vec{v} = \vec{c} \tag{5.4}$$

where $\vec{v}$ contains the Padé coefficients, $\vec{c}$ the Taylor coefficients and M is a matrix consisting of integers and

Taylor coefficients. The Padé coefficients are then determined by solving this linear system through matrix inversion.
Extension to multi-point expansions is straightforward: the relation in Equation 5.3 can be evaluated at each expansion point, with all resulting equations combined into an augmented matrix system M_{total} that incorporates information from all points. A source code generating the Matrix written in the Julia programming language is shown in source code B.1.

5.1.2 Least squares method

For the least-squares approach, only the χ^2 expression needs derivation, as its minimization directly yields the Padé coefficients.
Normally, when the coefficients of a function are to be determined by fitting to data points, the χ^2 is defined via the sum of the residuals, i.e., the differences between the function evaluated using a set of coefficients and the data points.
In this case however not only the value at the points are relevant but also the derivatives. To account for this, an additional term over the sum of derivatives (Taylor coefficients) is introduced into the χ^2. The residuals are redefined as the difference between the j^{th} derivative of the Padé approximation $R_n^m(x)$ evaluated at the k^{th} expansion point and the corresponding Taylor coefficient $T_k^{(j)}$:

$$\chi^2 = \sum_k \sum_j \left(\frac{\partial^j R_n^m}{\partial x^j}\bigg|_{x=x_k} - c_j^{(k)} \right)^2 \left(\sigma_j^{(k)}\right)^{-2} \tag{5.5}$$

5.1.3 Expansion variable

If the Padé approximation is constructed using an expansion variable other than x, some care must be taken in both cases. When the algebraic transformation is used, additional factors arising from the chain rule must be accounted for, whereas in the least-squares method, the derivative of the rational function may increase considerably in complexity.
Using, for example, the transformation $y = x^2$ can be accounted for by mapping the computed Taylor coefficients to a polynomial in x^2, taking into consideration the changing combinatorial factors, and subsequently taking the square root of, for example, the roots. However, employing the transformation $y = \cosh(x) - 1$ would complicate the determination of the matrix elements in M. Nevertheless, this modified expansion variable is used exclusively with the least-squares method, where the appearing complex derivatives can be taken care of by modern symbolic programming languages.

5.2 Comparison

The effectiveness of Padé approximations compared to Taylor expansions can be demonstrated through analysis of the function

$$f(z) = \frac{1}{\cosh(z)},$$

which possesses singularities at $z = i\pi(n - 1/2)$ for $n \in \mathbb{Z}$. It therefor follows that a Taylor series expansion of f at the origin will only converge within the radius of $\pi/2$ Performing the Taylor series expansion of f at 0 up to the six order (third order in z^2) yields:

$$\frac{1}{\cosh(z)} \approx 1 - \frac{z^2}{2} + \frac{5z^4}{25} - \frac{61z^6}{720} =: f_{\text{Taylor}}(z).$$

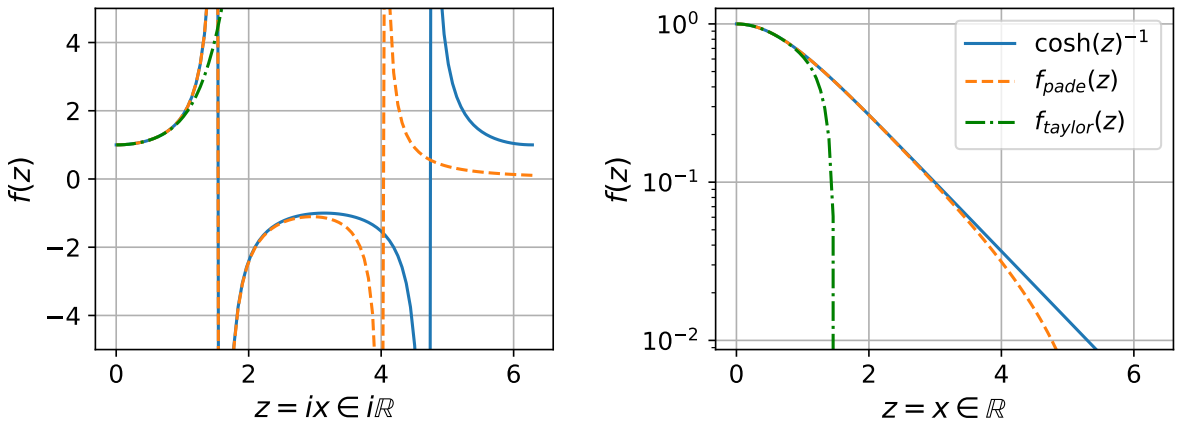

Figure 5.1 Comparison between a Taylor approximation and a Padé approximation performed at the origin of the function $1/\cosh(z)$. The behavior along both the real and imaginary axes over the interval $[0, 2\pi]$ is shown.

Since the function $\cosh(z)$ and consequently its reciprocal $1/\cosh(z)$ are even, only even-order terms z^{2n} appear in the series expansions. Applying the algebraic methods to construct a $[2,4]$-Padé approximation in z (equivalent to a $[1,2]$-Padé approximation in the variable z^2) yields the rational approximation:

$$\frac{1}{\cosh(z)} \approx \frac{1 - \frac{1}{30}z^2}{1 + \frac{7}{15}z^2 + \frac{1}{40}z^4} =: f_{\text{Pad}}(z).$$

Figure 5.1 compares the two expansions against the function f along the real and imaginary axis. The Padé approximation, even though it uses the same underlying information as the Taylor series, is able to reproduce the actual function significantly more accurately than the Taylor series. While the Taylor series, as expected, diverges after the radius of convergence, the Padé approximation is able to represent the function even beyond $\pi/2$.

5.3 Singularity Structure

Using the terminology introduced in [44], the term *singularity structure* refers to zero-pole structure found by the Padé approximant. Especially the pole structure will be needed for the whole analysis of Lee-Yang Zeros. Figure 5.2 shows the full singularity structure for two Padé fits of different order, both approximating $1/\cosh(x)$. In both figures the observed poles occur in complex conjugate pairs, a direct consequence of the complex conjugate root theorem [67] combined with the even parity of the Padé denominator. Additionally, since the zeros and poles do not align, it can be concluded that all poles describe not removable singularities. When the closest analytical singularity is examined, it becomes apparent that, as the order of the Padé approximation increases, truncation effects on the position of the poles are reduced. Moreover, the $[3,4]$ Padé approximation is able to resolve a singularity beyond the closest one.
So far, all calculations of derivatives in the $1/\cosh(x)$ example have been performed analytically, without any impact from noise. When 3% noise is added to the derivatives and the Padé fit is repeated one hundred times, a noisy singularity structure is obtained; see Figure 5.3. While the poles of the [1,2]-Padé shift only slightly and stay clustered together, the pole and zero structure in the [3,4]-Padé scatter significantly. In this noisy singularity structure, as well as in all singularity structures used throughout the thesis, close zeros and poles have been canceled out to eliminate removable singularities. The $[3,4]$ Padé approximation is also unable to detect singularities beyond the closest one, which itself can only be resolved under a high level of noise.

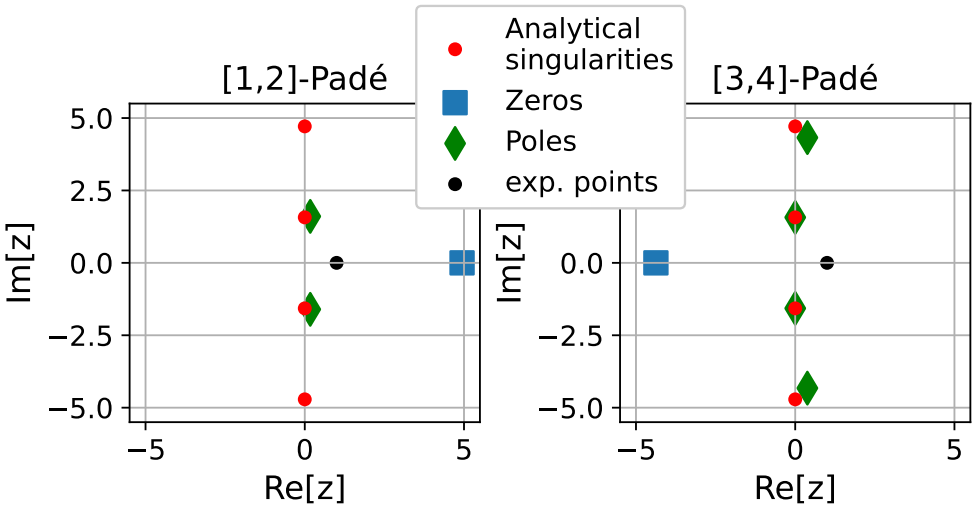

Figure 5.2 Depiction of the singularity structure for the simple $1/\cosh(z)$ example in the complex plane for two different Padé orders. The actual analytical singularities at $z = i(\mathbb{Z} + 1/2)\pi$ are shown in red, the estimated zeros and poles are shown in blue and green, respectively, and the point of expansion is indicated in black.

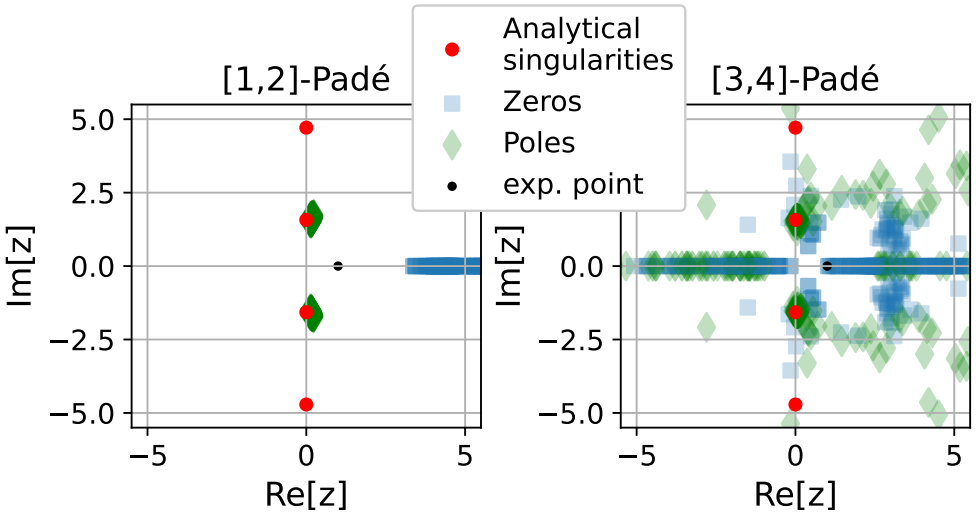

Figure 5.3 Depiction of the singularity structure for the simple $1/\cosh(z)$ with a relative noise of 3% applied to all derivatives. The fitting procedure is repeated 100 times. Each individual zero and pole is plotted with reduced transparency, so that areas of aggregation become visible through increased opacity.

6 Statistical methods

Many statistical methods are used throughout the analysis with two important ones being highlighted in this chapter. Section 6.1 elaborates how most statistical uncertainties of observables are computed while section 6.2 discusses the smoothing of data.

6.1 Jackknife analysis

To calculate the statistical uncertainties for all observables derived from simulations, Jackknife resampling is employed. This method is required because the propagation of errors and particularly the treatment of correlations through analysis techniques such as fitting procedures is often very complicated. Additionally, if the data is blocked, the autocorrelation of observables is accounted for.
The blocked leave-one-out Jackknife method for mean estimation starts with partitioning the complete dataset, referred to as the central sample, into N_J equally sized blocks [68]. From these blocks, a series of N_J estimates is generated by successively excluding each block and computing the mean of the observable θ using the remaining $N_J - 1$ blocks, this is also called the Jackknife Replicate. This step is shown in Equation 6.1, where $\bar{\theta}_{(i)}$ represents the i'th Jackknife samples and θ_j the value of θ on the j'th block.
This procedure is illustrated in Equation 6.1, where $\bar{\theta}_{(i)}$ denotes the i^{th} Jackknife sample mean and θ_j represents the observable's value in the j^{th} block.

$$\bar{\theta}_{(i)} = \frac{1}{N_J - 1} \sum_{j \neq i} \theta_j, \qquad i = 1, \ldots, N_j. \tag{6.1}$$

Of note is that before these Jackknife samples are used to compute the estimator of the uncertainty of θ, different other observables can be computed based on these samples with all there variance and covariance computable by the following method. Especially helpful is the fact that complex procedures such as fit need only be done N_J times instead of on each measurement of an observable.
The variance of a observable with $\bar{\theta}_{\text{Jack}} = \frac{1}{n} \sum_{i=1}^{n} \bar{\theta}_{(i)}$ is then given by

$$\widehat{\text{var}}(\bar{\theta})_{\text{Jack}} = \frac{N_J - 1}{N_J} \sum_{i=1}^{N_J} (\bar{\theta}_{(i)} - \bar{\theta}_{\text{Jack}})^2 \tag{6.2}$$

The correlation Matrix C of a set of observables θ_k with Jackknife samples can be computed via[69]

$$C_{lm} = \frac{N_J - 1}{N_J} \sum_{i=1}^{N_J} (\bar{\theta}_{l,(i)} - \bar{\theta}_{l,\text{Jack}})(\bar{\theta}_{m,(i)} - \bar{\theta}_{m,\text{Jack}}) \tag{6.3}$$

Therefore, an efficient and thorough calculation and estimation of the statistical uncertainties and covariances of observables is enabled by this method.
In the computation of fits, not only the values of the observable are required, but also the variance, and in the case of correlated fits, the covariance matrix. In theory, the covariance matrix can be computed independently by performing a leave-one-out Jackknife analysis on the sample. However, this procedure significantly reduces the underlying block size and increases the statistical noise, to which the covariance matrix is particularly sensitive. Therefore, Equation 6.3 is employed to compute the covariance matrix on the central sample, which is then repeatedly used for each individual fit of the Jackknife samples.
One limitation of the Jackknife method is the requirement of a smooth estimator for the observable θ. This

limitation can be overcome by employing the generalization of the Jackknife method, namely the bootstrap method, as it allows access to the complete underlying distribution [70].

6.2 Least-squares spline approximation

In order to produce smooth curves from discrete data points, which is particularly useful for visualizations such as heatmaps, a general interpolation method is required when no *a priori* knowledge of an underlying fit model is available or should be imposed. One such method is the so-called spline interpolation using basis splines (B-splines), which is, for example, considered superior to polynomial interpolation, as Runge's phenomenon is avoided. As described in detail by De Boor [71], B-splines enable the construction of a general spline function of order n, as a linear combination of B-splines:

$$S_{n,\mathbf{t}}(x) = \sum_i \beta_i B_{i,n}(x). \tag{6.4}$$

The B-Splines themselves are piecewise polynomial function of degree $n-1$ defined on the interval containing $n+1$ breakpoints (or knots) $\vec{t}$. These breakpoints therefor play the important role of determining the amount of B-splines used and which area should be given more or less focus. Combining this ansatz with the method of weighted least squares produces this objective function U which has to be minimized for the values of $\vec{\beta}$

$$U = \sum_j \left\{ W \left[y_j - \sum_i \beta_i B_{i,k,\mathbf{t}}(x_j) \right] \right\}^2. \tag{6.5}$$

The summation over the index j iterates through all observed data points (x_j, y_j), and W represents the weight matrix defined as the inverse of the covariance matrix $W = \Omega^1$. The summation over the index j iterates through all the observed data points (x_j, y_j), and W represents the weight matrix, which is the inverse of the covariance matrix $W = \Omega^1$. Since the ansatz S is linear in β, the Parameter and associated covariance matrix can exactly be solved for. Defining the basismatrix $B_{i,j} = B_{i,k,\mathbf{t}}(x_j)$ leads to the following analytical solutions:

$$\begin{aligned} \hat{\beta} &= (B^T \cdot W \cdot B)^{-1} B^T \cdot W \cdot \vec{y} \\ M^\beta &= \left(B^T \cdot W \cdot B\right)^{-1}. \end{aligned} \tag{6.6}$$

Via the residuals $\vec{r} = B \cdot \vec{\beta} - \vec{y}$ the expression for χ^2 can also be written as $\chi^2 = \vec{r}^T \cdot W \cdot \vec{r}$. Here it should be said, that the construction of the B-Splines and calculation of basismatrix is carried out via the Julia package `BSplines.jl`[72].
The primary challenge clearly lies in determining optimal breakpoint locations. These should generally be placed with higher density in regions where the underlying data varies. While this analysis usu manual breakpoint selection, automated algorithms exist to determine optimal positions [73].
To determine the error of the approximation at any given point, Jackknife resampling is used in the usual.

Part III

Results

Introduction

This part summarizes all results obtained from the analysis of baryon fluctuations, defined as the Taylor expansion coefficients of the pressure with respect to the baryochemical potential (μ_B). These results are derived by applying the methods described in Part II and are interpreted within the theoretical framework presented in chapter 3. Many of the results presented here originate from the co-authorship of the publication [65].

7 The fluctuations

The basis for the entire analysis consists of the baryon number fluctuations introduced in section 2.5. While fluctuations at both zero and imaginary chemical potential (μ_B) contribute to different aspects of the study, the $\mu_{\mathrm{B}} = 0$ results are initially analyzed separately due to their extended temperature range and superior statistics. These zero chemical potential fluctuations alone provide significant insight into the $\mu_{\mathrm{B}} > 0$ region. Subsequently, both datasets are combined for the final comprehensive analysis. The details of the algorithm used to generate the configurations from which the fluctuations were calculated are described in chapter 4. The most essential features of the lattice setup are summarized as follows: The configurations are generated on a $16^3 \times 8$ lattice using 4HEX-smeared staggered fermions, corresponding to a fixed physical volume of $LT = 2$ in temperature units. Further details of the implementation are provided in chapter 4.

7.1 Fluctuations at zero chemical potential

In previous works by the Wuppertal-Budapest collaboration [58, 74], which provided the configurations used in this analysis, the same lattice setup was employed but with lower statistics. The current analysis benefits from approximately 2 million configurations per temperature at zero chemical potential, covering a temperature range from 100 MeV to 300 MeV with 5 MeV steps between 100-210 MeV and 10 MeV steps from 210-300 MeV. This temperature scanning enables a thorough investigation of the entire region while particularly focusing on the regime below the Roberge-Weiss transition [35]. The extensive dataset allows calculation of Taylor coefficients for the pressure (i.e., baryon number fluctuations) up to tenth order in μ_{B}. The fixed-volume approach permits determination of the sixth and eighth derivatives with unprecedented precision, while this work also presents the first calculation of the tenth-order coefficient in the literature. Figure 7.1 depicts the mentioned results with black data points, alongside a Least-squares spline approximation. The technical details of the spline approximation are elaborated on in section 6.2. In the plots, the orange band surrounding the data points represents the one-sigma uncertainty envelope derived from the spline approximation. Purple crosses denote the positions of the breakpoints used in the spline construction Below each main plot, an auxiliary plot displays the corresponding residuals. Since the correlations between different temperatures are negligible, no correlated fitting procedure was necessary for the spline construction. The breakpoint positions were optimized to yield an acceptable reduced χ^2 for each spline fit. The location of the breakpoint positions has been hand tuned such that each spline fit yield an acceptable reduced χ^2. This, of course, is a possible source of systematic error alongside the introduction of a correlation of the fluctuations with regard to the temperature. The heatmap visualization of extrapolation to real μ_{B}, which will be introduced soon, is unaffected due to its qualitative nature. However, the Lee-Yang zero analysis uses only raw data points to prevent spline artifacts and enable straightforward computation of the correlation matrix.
For completeness in data representation, the ratio of fluctuations to the susceptibility χ_2 is also shown in Figure 7.2. This conventional presentation, frequently adopted in the literature, facilitates direct comparison with established models such as the HRG model introduced in section 2.7.

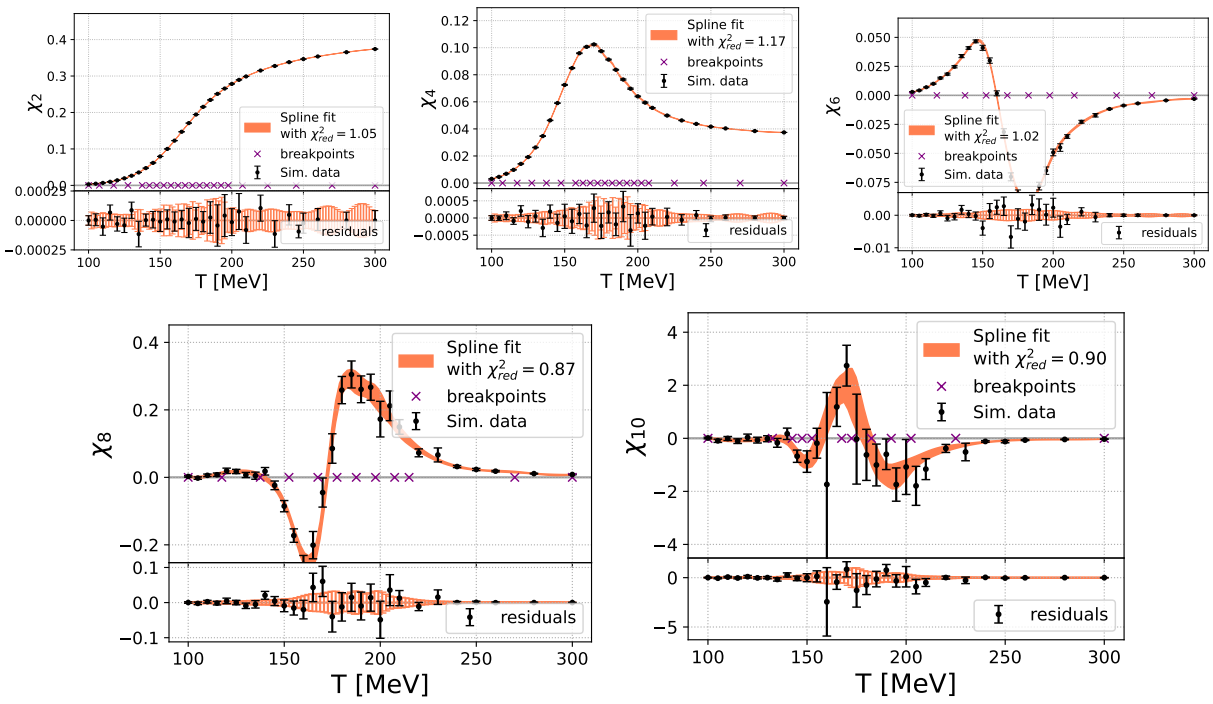

Figure 7.1 Temperature dependence of the pressure derivatives $\partial^n \hat{p}/\partial \mu_B^n|_{\mu_B=0}$, showing numerical results with 5 MeV spacing ($T < 210$ MeV) and 10 MeV spacing ($T > 210$ MeV). The spline interpolation (solid curve) provides a description of the data, as evidenced by the reduced $\chi^2 \approx 1.0$ of the fit.

For a minimal consistency check, the ratio of even fluctuations should equal one, which the data supports. It should be noted that since Figure 7.1 and Figure 7.2 do not include imaginary μ_B data, no analytic continuation contributes to these results.

7.2 Taylor extrapolations to non-zero chemical potential

The splined data depicted in Figure 7.1 allows us without the assumption of any further model to extrapolate to positive, real, non-zero chemical potential. As a reminder from section 2.5, the Taylor expressions for even and odd derivatives take the following from, respectively,

$$\chi^B_{2n}(T,\mu_B) = \left(\frac{\partial^{2n}(p/T^4)}{\partial(\mu_B/T)^{2n}}\right)_{\mu_B} = \chi_{2n} + \chi_{2n+2}\frac{\hat{\mu}_B^2}{2!} + \chi_{2n+4}\frac{\hat{\mu}_B^4}{4!} + \dots \tag{7.1}$$

$$\chi^B_{2n-1}(T,\mu_B) = \left(\frac{\partial^{2n-1}(p/T^4)}{\partial(\mu_B/T)^{2n-1}}\right)_{\mu_B} = \chi_{2n}\hat{\mu}_B + \chi_{2n+2}\frac{\hat{\mu}_B^3}{6} + \chi_{2n+4}\frac{\hat{\mu}_B^5}{5!} + \dots, \tag{7.2}$$

where n always represents a non zero integer and the sum may only go up to the highest considered expansion coefficient. When the expansion is truncated at $\mathcal{O}(\mu_B^8)$, the second-order baryon fluctuation $\chi_2^B(T,\mu_B)$ depends on $\{\chi_2,\chi_4,\chi_6,\chi_8\}$, while the fourth-order fluctuation $\chi_4^B(T,\mu_B)$ is determined solely by $\{\chi_4,\chi_6,\chi_8\}$. A comprehensive visualization of the phase diagram region is generated using this approach. The methodology is partially inspired by [75, 76], with a bicolor heatmap scheme being employed where deep blue represents -5 and deep red $+5$ of the target observable. The temperature range $T \in [100, 250]$ MeV is displayed in all heatmaps of this analysis, with extrapolation being performed up to $\mu_B \in [0, 750]$ MeV while the aforementioned color scale is maintained. Each visualization includes a yellow freeze-out curve from [77], the QCD crossover line (T_C line) from [78], and black dotted lines indicating constant dimensionless chemical

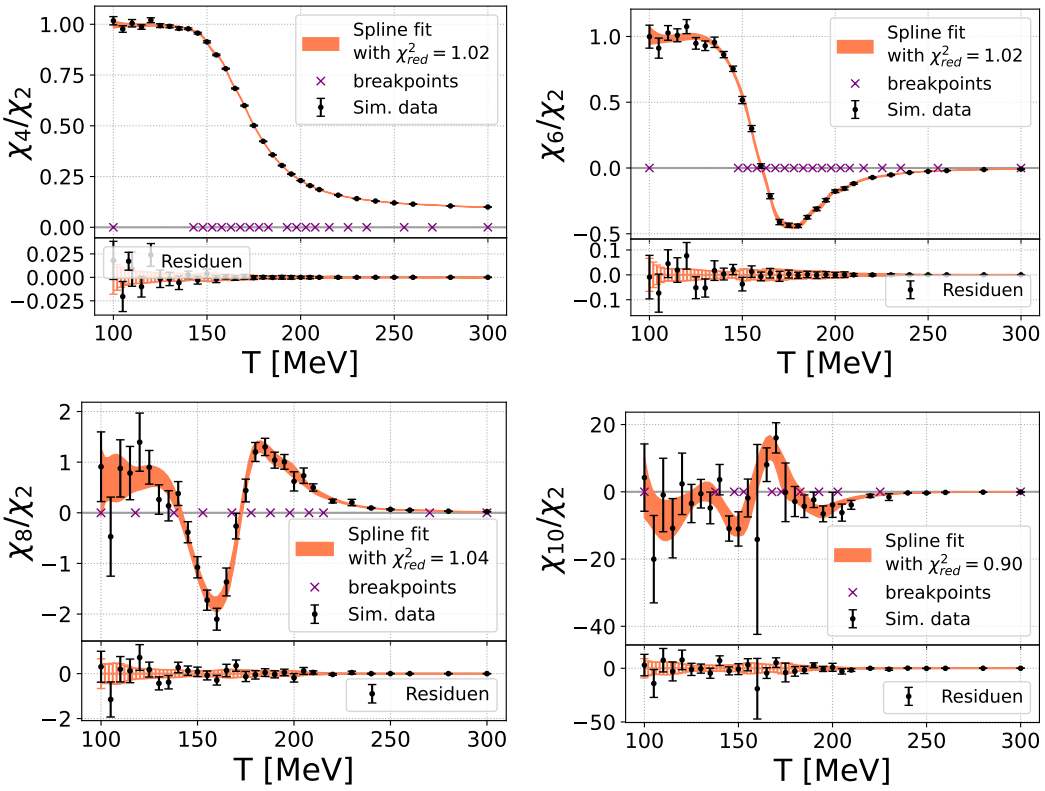

Figure 7.2 Ratios of fluctuations at $\mu_B = 0$ as functions of the temperature T on our $16^3 \times 8$ 4HEX ensembles, together with a spline interpolation of the data points. Temperature dependence of the Ratios of pressure derivatives, showing numerical results with 5 MeV spacing ($T < 210$ MeV) and 10 MeV spacing ($T > 210$ MeV). The spline interpolation (solid curve) provides again a description of the data, as evidenced by the reduced $\chi^2 \approx 1.0$ of the fit.

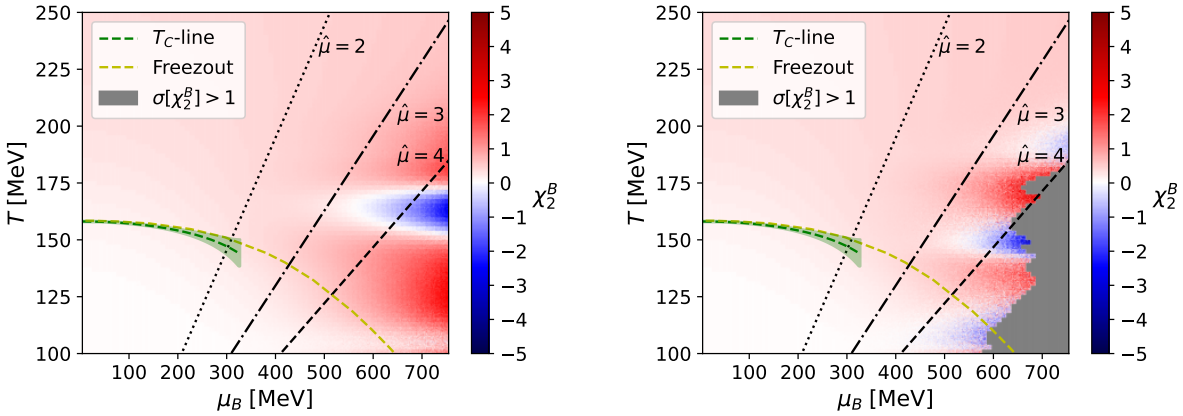

Figure 7.3 $\chi_2^B(T, \mu_B)$ from a Taylor expansion up to χ_8 (left) and χ_{10} (right), using the splined Taylor coefficients form Figure 7.1. Also depicted is the chemical freezeout line from [77], the crossover line from [78] and three black lines for a constant $\hat{\mu}$. The statistical error is indicated by the noise in the image and the region of a greater absolute standard deviation of one is masked in gray.

potentials $\hat{\mu}_B = \{2, 3, 4\}$ as a reference. Additionally, regions where the absolute error of the observable reaches unity are shaded in gray. This visual indicator denotes reduced extrapolation reliability, although it does not represent a formal convergence assessment, which would require more Taylor coefficients than are currently available in this analysis to yield reliable results. To properly represent statistical uncertainties, the heatmap is constructed using both the central sample values and their associated errors, rather than simply the central values. For each small region, a Gaussian probability density function (PDF) is built from the central value and its jackknife error estimate. Individual pixel values are then sampled from this distribution, ensuring that the visualization fully incorporates the statistical uncertainty structure.

Figure 7.3 displays the susceptibility $\chi_2^B(T, \mu_B)$ using the heatmap methodology described above. The left panel shows results from the Taylor expansion truncated at $\mathcal{O}(\mu_B^6)$ (incorporating χ_8), while the right panel shows the expansion up to $\mathcal{O}(\mu_B^8)$ (incorporating χ_{10}).

The Taylor expansion incorporating χ_8 exhibits predominantly positive values with a well-defined negative peak in the region $T \in [150, 175]$ MeV for $\mu_B \geq 550$ MeV. Comparison with the χ_{10}-inclusive expansion reveals three key modifications: the negative peak shifts downward in temperature, additional susceptibility structures emerge, and statistical noise increases (manifested through more actual noise in the heatmap and gray uncertainty regions at high μ_B). These multiple peaks in the full expansion reflect the characteristic sign structure of χ_{10}, demonstrating that the highest-order coefficient dominates the estimate at large chemical potentials ($\mu_B \gtrsim 550$ MeV). This implies that the validity of the extrapolation at large chemical potentials cannot be rigorously verified without including higher-order terms in the expansion. To identify potential critical behavior, fluctuation ratios should be examined due to their enhanced sensitivity [19]. Two construction methods are available: either Taylor-expanding the ratio directly, or computing the ratio of pre-expanded Taylor series.

While direct Taylor expansion of ratios has been implemented in previously, this approach becomes problematic for high chemical potential extrapolations. For instance, consider $\chi_4^B(T, \mu_B)/\chi_2^B(T, \mu_B)$ at low temperatures: the denominator $\chi_2^B(T, \mu_B)$ exhibits a zero crossing near $\mu_B/T = \pi/2$ (up to deviations from HRG), which fundamentally limits the convergence radius of the expanded ratio.

Therefore, the more robust approach is to first compute separate Taylor expansions for both numerator and denominator, then combine them to form the ratio.

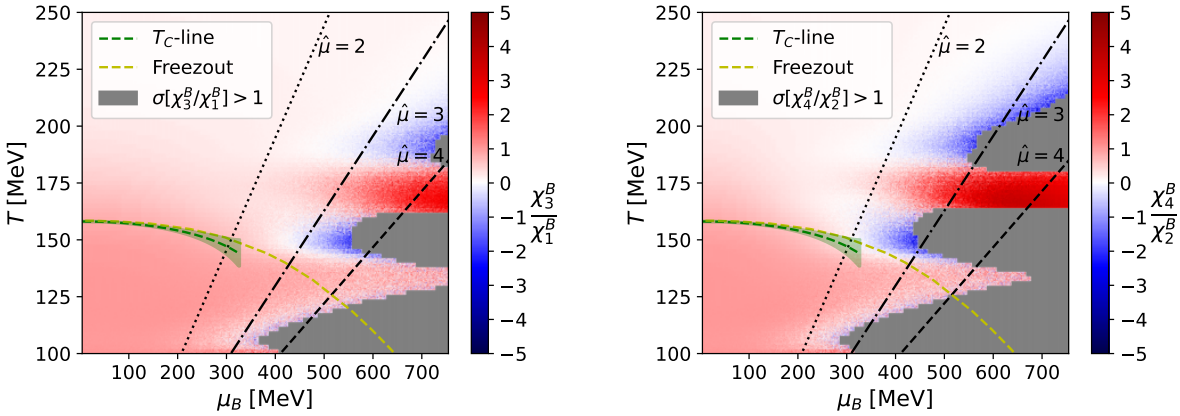

Figure 7.4 The ratio $\chi_3^B(T,\mu_B)/\chi_1^B(T,\mu_B)$ (left) and $\chi_4^B(T,\mu_B)/\chi_2^B(T,\mu_B)$ obtained by using the Taylor coefficients up to χ_{10} form Figure 7.1 in conjunction with Equation 7.4 and Equation 7.3 respectively. Further legend information from Figure 7.3 applies.

For the aforementioned example would this result in the following expression.

$$\frac{\chi_4^B(T,\mu_B)}{\chi_2^B(T,\mu_B)} \approx \frac{\chi_4 + \chi_6\frac{\hat{\mu}_\mathrm{B}^2}{2} + \chi_8\frac{\hat{\mu}_\mathrm{B}^4}{4!} + \chi_{10}\frac{\hat{\mu}_\mathrm{B}^6}{6!},}{\chi_2 + \chi_4\frac{\hat{\mu}_\mathrm{B}^2}{2} + \chi_6\frac{\hat{\mu}_\mathrm{B}^4}{4!} + \chi_8\frac{\hat{\mu}_\mathrm{B}^6}{6!} + \chi_{10}\frac{\hat{\mu}_\mathrm{B}^8}{8!}} \tag{7.3}$$

For $\chi_3^B(T,\mu_B)/\chi_1^B(T,\mu_B)$ this takes the form:

$$\frac{\chi_3^B(T,\mu_B)}{\chi_1^B(T,\mu_B)} \approx \frac{\chi_4\hat{\mu}_\mathrm{B} + \chi_6\frac{\hat{\mu}_\mathrm{B}^3}{3!} + \chi_8\frac{\hat{\mu}_\mathrm{B}^5}{5!} + \chi_{10}\frac{\hat{\mu}_\mathrm{B}^7}{7!},}{\chi_2\hat{\mu}_\mathrm{B} + \chi_4\frac{\hat{\mu}_\mathrm{B}^3}{3!} + \chi_6\frac{\hat{\mu}_\mathrm{B}^5}{5!} + \chi_8\frac{\hat{\mu}_\mathrm{B}^7}{7!} + \chi_{10}\frac{\hat{\mu}_\mathrm{B}^9}{9!}} \tag{7.4}$$

Figure 7.4 show both of these expansions side by side. Both figures exhibit structures similar to χ_2^B, with the highest-order term dominating at large chemical potentials. The ratio χ_3^B/χ_1^B remains monotonic along both the transition and freeze-out lines up to the gray-shaded region where statistical errors exceed one. In contrast, χ_4^B/χ_2^B displays non-monotonic behavior, as the negative peak observed in the χ_2^B heatmap extends to lower μ_B values and into the path of the freeze-out line. The absence of non-monotonic behavior in χ_3^B/χ_1^B compared to its presence in χ_4^B/χ_2^B does not match the expected signatures of chiral criticality. This indicates the effect likely arises from Taylor series truncation, particularly due to the sign structure of χ_{10} dominating at large chemical potentials ($\mu_\mathrm{B} \gtrsim 550$ MeV). While the ratio χ_4^B/χ_2^B is theoretically more sensitive to critical behavior than χ_3^B/χ_1^B [19], the current analysis demonstrates the limitations of Taylor expansions with the present dataset. For a more quantitative analysis of the phase diagram, a model-based study employing Lee-Yang zeros is carried out in the following chapters.

8 Rational approximations

To determine the Lee-Yang zeros, a functional form for the baryon number susceptibilities is required. In the present work, this role is fulfilled by a rational approximation (Padé fits), whose motivation is provided in chapter 3, with its application demonstrated in chapter 9, and whose theoretical background is explained in detail in chapter 5. The direct results of these rational fits are presented in this chapter, where the imaginary data are explicitly incorporated into the fitting procedure. Fits at different temperatures are performed independently, and this independence is maintained by omission of spline interpolation. In addition, a heatmap of the phase diagram is constructed on the basis of this extrapolation method.

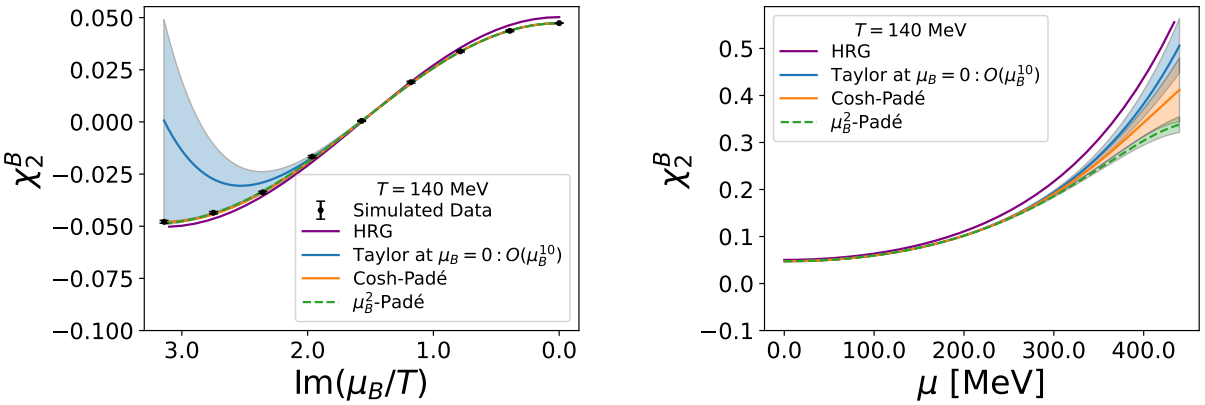

Figure 8.1 The result of the fitting of the $\Delta\hat{p}$ model in Equation 9.1 (orange) with a general Padé in $x = \mu_B^2$ (green) with $m = 1$ and $n = 2$ at $T = 140$ MeV and plotting the results χ_2^B

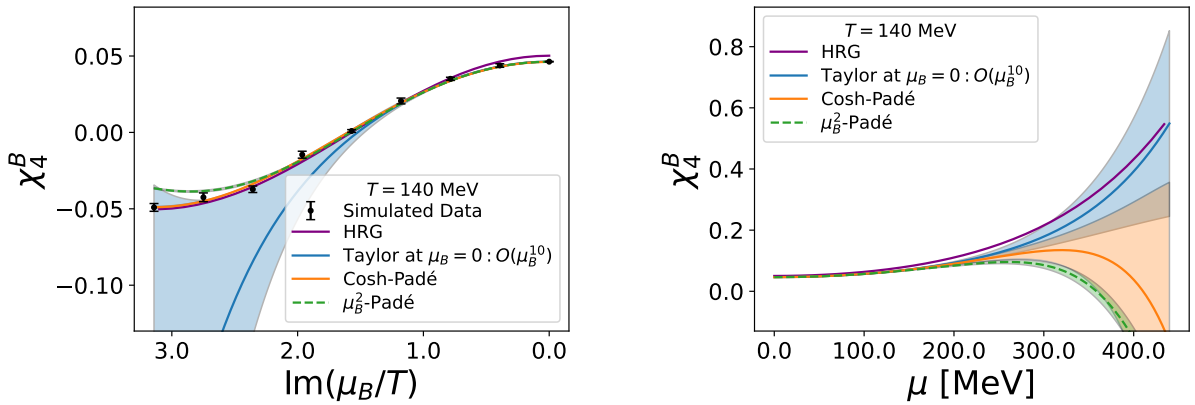

Figure 8.2 The result of the fitting of the $\Delta\hat{p}$ model in Equation 9.1 (orange) with a general Padé in $x = \mu_B^2$ (green) with $m = 1$ and $n = 2$ at $T = 140$ MeV and plotting the results χ_4^B

8.1 Exemplary fit at $T = 140\,\mathrm{MeV}$

The rational approximation procedure is illustrated at $T = 140\,\mathrm{MeV}$ using Padé fits of order $[1, 2]$ with two expansion variables: $x = \mu_\mathrm{B}^2$ and $x = \cosh(\mu_B) - 1$. In Figure 8.1, the observable χ_2^B is compared using the $\Delta\hat{p}$ ansatz, both expansion schemes, the HRG baseline, the standard Taylor expansion about $\mu_\mathrm{B} = 0$, and the simulated imaginary-μ_B data. The left figure displays the results along the imaginary μ_B axis where simulated data are available, while the right figure shows the expansion along the real μ_B axis. All curves, except for the HRG baseline, are accompanied by one-standard-deviation error bands calculated through jackknife analysis. The Taylor expansion exhibits rapidly growing uncertainties along the imaginary μ_B axis when compared to the Padé fits, as expected since the latter incorporate information from simulated data points. Along the real μ_B axis, however, the Taylor expansion demonstrates slower error growth than the Cosh-Padé approximation. All expansions generally reproduce the simulated χ_2^B values within uncertainties. A notable exception occurs for χ_4^B, as shown in Figure 8.2, where the μ_B^2-Padé approximation shows significant deviations at large $\mathrm{Im}\,\mu_B$ values, while the Cosh-Padé results remain consistent with the expected behavior. To demonstrate the difference of the approximations, the differences between the simulated data and the fits for both χ_2^B and χ_4^B are computed for each expansion variable and presented in Figure 8.3. Each data point represents the deviation from the simulated data, with uncertainties properly calculated through jackknife

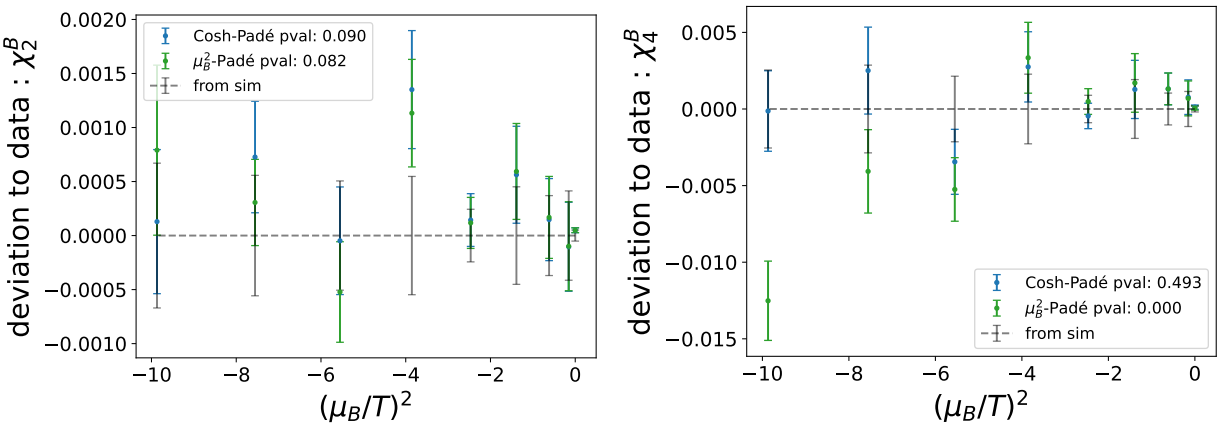

Figure 8.3 Plot indicating the difference of the fitted results to the simulated data for the Cosh-Padé and μ_B^2-Padé at at $T = 140$ MeV with $\Delta\hat{p}$ ansatz The p-value in the legend indicates the agreement of the displayed estimated coefficient to the simulated data.

analysis. The intrinsic error of each data point is additionally displayed as an error bar centered at zero for reference. To quantitatively assess the agreement between models and observables, a χ^2 test is performed to evaluate their consistency with zero deviation, from which a corresponding p-value is derived and displayed in the legend. For χ_2^B, both expansion methods yield p-values exceeding 5%, indicating statistically consistent results. However, for χ_4^B, only the Cosh-Padé approximation maintains a good p-value, confirming the initial qualitative assessment.

8.2 Overview of all performed fits

The fit quality of all models can be assessed through their p-values. Under ideal conditions where the χ^2 values follow their theoretical distribution, these p-values should be uniformly distributed, resulting in a linear cumulative distribution function (CDF).

Since the analysis employs jackknife resampling, the χ^2 values and corresponding p-values for the Padé fits include calculable uncertainties that must be considered when evaluating fit quality. Figure 8.4 displays the empirical CDF (ECDF) of these p-values. The left panel corresponds to Cosh-Padé fits of $\mu_\mathrm{B} = 0$ data ($T \in [100, 170]$ MeV), used to regenerate section 7.2's heatmaps via Cosh-Padé extrapolation, while the right panel includes all data (imaginary μ_B results for $\chi_{1,2,3,4}$) across $T \in [130, 155]$ MeV. The blue line corresponds to the ECDF of the central sample p-value, while the orange and green lines correspond to the p-value plus or minus one standard deviation. An additional ideal linear CDF is drawn in black. For fits using only zero μ_B data, the larger number of available fits produces an empirical cumulative distribution function (ECDF) that closely follows the expected linear cumulative distribution. In contrast, fits incorporating imaginary μ_B data yield noisier ECDF estimates due to the smaller sample size. Notably, while the central sample's p-value ECDF deviates from linearity, the ECDF including $+1\sigma$ variations aligns with expectations, containing only a single p-value below 5%.

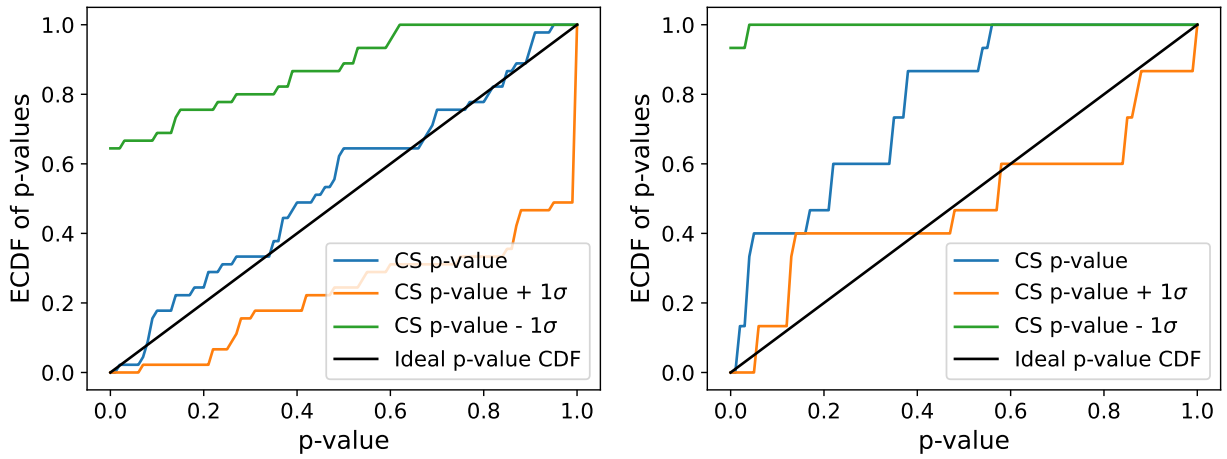

Figure 8.4 The empirical distribution function of the p-values is shown for both cases of excluding the imaginary μ_B data (left panel, as used in the following heatmaps) and including the imaginary μ_B data (right panel, as used in the Lee-Yang zero estimation), with three curves displayed in each case: the p-values from the central sample and the p-values from the central sample plus or minus one standard deviation as obtained from the jackknife analysis.

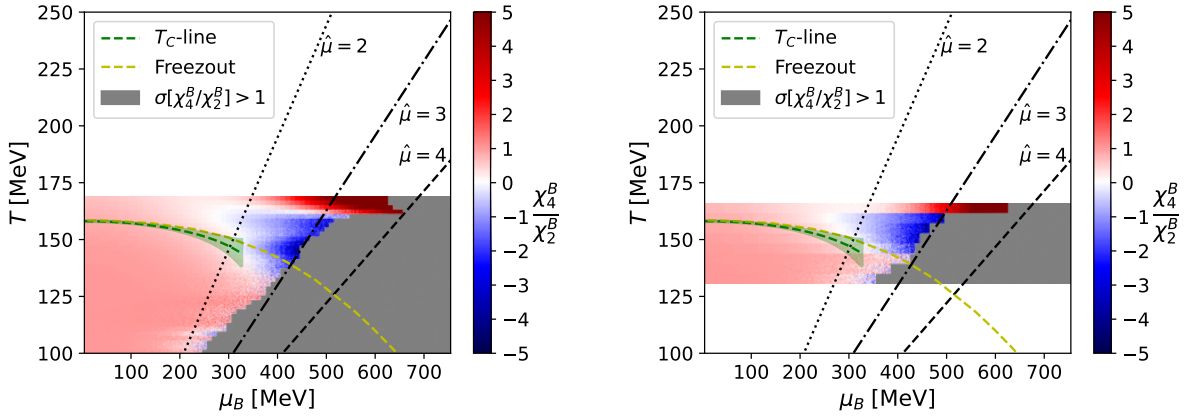

Figure 8.5 $\chi_4^B(T,\mu_B)/\chi_2^B(T,\mu_B)$ Extrapolation via Cosh-Padé using only the splined $\mu_B = 0$ data on the left and the unsplined full dataset on the right.Further legend information from Figure 7.3 applies.

8.3 Cosh-Padé Extrapolations to non-zero chemical potential

Using the Cosh-Padé as discussed in the previous section and the heatmap visualization introduced in section 7.2 a extrapolations to non-zero real chemical potential can again be performed. In Figure 8.5, the left panel displays extrapolation results obtained using spline-interpolated data at zero chemical potential ($\mu_B = 0$). The temperature range $T \in [100, 170]$ MeV is selected based on an acceptable p-value criterion. The right panel utilizes the complete dataset, comprising both imaginary and zero-μ_B data, where spline interpolation is intentionally omitted to avoid complications arising from the increased correlations. Both extrapolation methods demonstrate non-monotonic behavior, although the non-spline approach produces substantially less conclusive results due to its reduced temperature resolution. Furthermore, the inherent model dependence introduces additional systematic uncertainties that are not currently accounted for. Collectively, these findings suggest potential limitations in the reliability of the qualitative analysis.

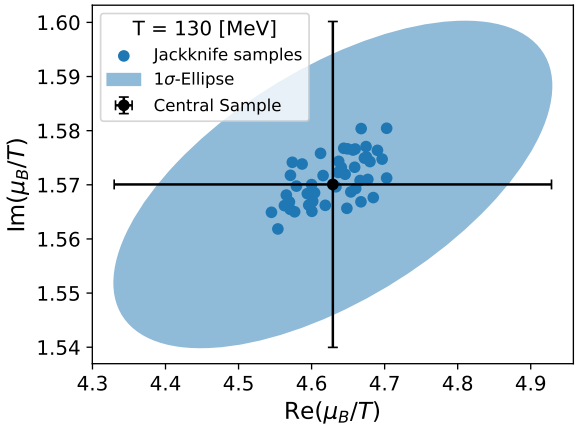

Figure 9.1 Exemplary plot of the extracted Lee-Yang zeroes obtained by the Cosh-Padé for the temperature of 130 MeV & $\Delta\hat{p}$ ansatz (left). The ellipses represent the 1σ-confidence interval.

9 Lee-Yang Zero analysis

While the Cosh-Padé method provides an alternative approach for direct extrapolation to non-zero chemical potential, its primary motivation and benefit lie in its ability to identify potential signals of Lee-Yang edge (LYE) singularity via the determination of the Lee-Yang zeroes (LYZ) and there scaling relations. For further theoretical discussion, see chapter 3. section 9.1 details the methodology for extracting LYZ, while section 9.2 and section 9.5 discuss the differential ansatz approach and systematic uncertainties in the analysis. section 9.3 establishes the non-critical baseline using the hadron resonance gas (HRG) model, identifying the applicable range of lattice data. Finally, section 9.6 combines these components to present the final results for critical points.

9.1 Determination of LYZ

The extraction of the Lee-Yang zeros (LYZ) is performed using the Padé ansatz. As a reminder, this ansatz is a rational approximation in which both the numerator and the denominator are expressed as polynomials in the expansion variable x. The roots of the denominator polynomial correspond to potential singularities of the fitted function, and when the approximation is valid, these singularities are expected to coincide with the LYZ. To determine the roots and therefore the LYZ, first the complex roots of $1 + q_1 x + q_2 x^2$ are taken then the location of the LYZ in terms of μ_{B} can then be calculated with the inversion the relation $x = \cosh(\mu_B) - 1$. Due to charge conjugation symmetry and Roberge-Weiss periodicity, only roots satisfying $\mathrm{Re}(z) > 0$ and $\mathrm{Im}(z) \in (0, \pi)$ need to be considered. When multiple roots meet these criteria, the one closest to the origin is selected for extrapolation to the Lee-Yang edge (LYE) singularity. Figure 9.1 displays the estimated Lee-Yang zero (LYZ) locations at $T = 130$ MeV, showing both the central value and the distribution of corresponding jackknife samples. Additionally, a one-standard-deviation confidence ellipse and individual error bars along both the real and imaginary axes are drawn for the Lee-Yang zero estimate, based on the covariance matrix constructed from the Jackknife analysis.

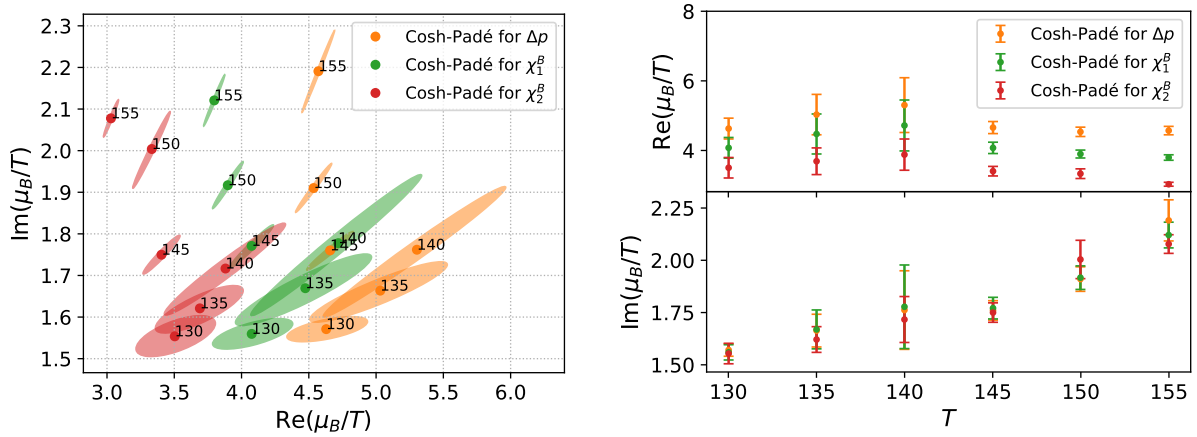

Figure 9.2 Overview plot for all used temperatures and ansätze The colors indicate the different ansatz while the temperature in MeV is shown beside the corresponding ellipse in the left.

9.2 Different ansätze

Before implementing the scaling ansatz for LYZ's across multiple temperatures to determine the LYE singularity location, the possible systematic uncertainties inherent in the Cosh-Padé analytic continuation should be examined. While varying the degrees of freedom in both numerator and denominator could in principle provide systematic error estimation, statistical limitations constrain the ansatz to at most a quadratic denominator. Furthermore, as demonstrated in section 9.3, a minimum quadratic order is required for the denominator to allow singularities to span the entire phase space. These dual constraints consequently fix the Padé order, preventing variation in the approximation scheme.

To still be able to estimate to systematically estimate uncertainties, multiple observables can be fitted using the identical [1,2]-Cosh-Padé ansatz.

For this purpose, the quantities $\Delta\hat{p}$, χ_1, and χ_2 are chosen, all of which are related to the free energy and therefore follow the scaling behavior described in chapter 3. In the Padé ansatz, the denominator polynomial is kept fixed, while the numerator is adjusted slightly to account for the available statistics and to respect charge-conjugation symmetry.

In the Padé ansatz, the numerator for $\Delta\hat{p}$ contains only the term $a(\cosh(\hat{\mu})-1)$, since it represents the offset to the pressure and no constant term is present. The numerator for χ_1 is expressed using $\sinh(\hat{\mu})$, as it is an odd function under charge conjugation, while χ_2 is even, like $\Delta\hat{p}$, but includes a constant offset.

Equation 9.1 shows the exact form of the fit ansatz.

$$\begin{aligned}
\Delta\hat{p} &: (a(\cosh(\hat{\mu})-1))/(1+c(\cosh(\hat{\mu})-1)+d(\cosh(\hat{\mu})-1)^2) \\
\chi_1 &: (a(\sinh(\hat{\mu})))/(1+c(\cosh(\hat{\mu})-1)+d(\cosh(\hat{\mu})-1)^2) \\
\chi_2 &: (a+b(\cosh(\hat{\mu})-1))/(1+c(\cosh(\hat{\mu})-1)+d(\cosh(\hat{\mu})-1)^2)
\end{aligned} \tag{9.1}$$

Figure 9.2 presents a comparison of the Lee-Yang zero estimates obtained from all three ansätze at various temperatures, where the extraction was performed as described in section 9.1. From this figure, it can be concluded that, while the imaginary part of the Lee-Yang zeros remains stable across different choices of for the observable while the real part exhibits noticeable variation.

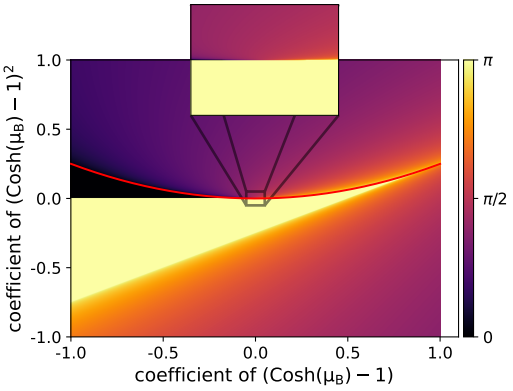

Figure 9.3 Imaginary part of the roots of the denominator, Equation 9.3, is shown. Since the ansatz preserves Roberge-Weiss symmetry, $\mathrm{Im}(\mu_B/T)$ is limited to $[0, \pi]$. The red line marks the boundary beyond which $x_{1/2} = (-q_1 \pm \sqrt{q_1^2 - 4q_2})/2$ itself becomes complex-valued (where $x \equiv \cosh(\hat{\mu}_B) - 1$).

9.3 Hadron resonance gas baseline via nHRG

The standard non-critical baseline for QCD at temperatures below the crossover transition is provided by the Hadron Resonance Gas (HRG) model, as detailed in section 2.7. When applying the Cosh-Padé approximation to the Boltzmann HRG model, all free coefficients in the denominator polynomial vanish, reducing it to 1. The numerator would then consequently simplifies to:

$$p = p_0(T) + p_1(T)\cosh(\mu_\mathrm{B}/T) \tag{9.2}$$

With noise however the roots of the denominator, whose functional form is shown in Equation 9.3, will be able to take on values, as apposed to the case where q_1 and q_2 are zero. When noise is included, the denominator roots (see denominator form in Equation 9.3) can attain values, in contrast to the $q_1 = q_2 = 0$ case where no roots can be determined.

$$1 + q_1(\cosh(\hat{\mu}_\mathrm{B}) - 1) + q_2(\cosh(\hat{\mu}_\mathrm{B}) - 1)^2 \tag{9.3}$$

The resulting roots are however dominated by statistical noise, leading to instability. The dependence of the imaginary part of the root closest to the origin on the denominator coefficients q_1 and q_2 is shown in Figure 9.3. When both q_1 and q_2 are small and fluctuating, the imaginary part of the root is constrained to values near either $\pi/2$ or π, with the specific case being determined by the sign of q_2. Additionally, it can be observed that the model permits the imaginary part of the Lee-Yang zeros to take any value within the full range from 0 to π. This is further supported by the zoomed-in region centered at $q_1 = q_2 = 0$, where the entire interval from 0 to π is also accessible. Consequently, the model is theoretically capable of resolving Lee-Yang zeros in proximity to the origin. To obtain predictions from the noisy Hadron Resonance Gas (nHRG) model, standard jackknife analysis cannot be employed due to inherent instabilities. These instabilities cause the jackknife samples for the imaginary parts of the zeros to cluster around $\pi/2$ and π, not allowing for a rigorous analysis with jackknife. For these reasons, the nHRG model is analyzed using bootstrap sampling. The procedure consists of taking HRG predictions for fluctuations at a given temperature, combining them with the relative errors observed in lattice calculations, and generating viable values for the Taylor coefficients $\chi_2, \chi_4, \chi_6, \chi_8, \chi_{10}$ The Lee-Yang zeros calculated from the bootstrapped coefficients still exhibit clustering behavior, but this bootstrap approach now enables proper statistical analysis of the individual clusters through conventional bootstrap error estimation techniques. Figure 9.4 shows the result for the imaginary part of LYZ the using the nHRG alongside the results obtained from the full QCD lattice data. The two distinct clusters are represented by green and purple points. The clustering criterion is defined

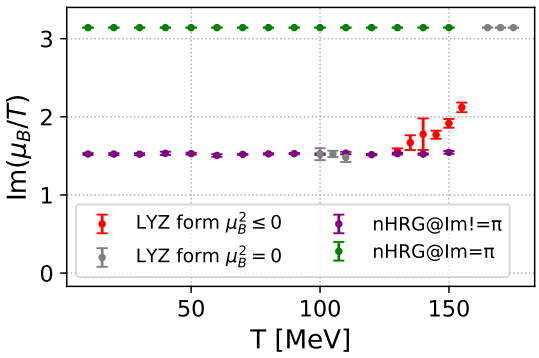

Figure 9.4 Estimates of $\mathrm{Im}(\mu_B/T)$ for Lee-Yang zeros using Cosh-Padé approximations: green/purple points show nHRG results, while red points use lattice data form $\mu_\mathrm{B}^2 \leq 0$. Additionally, the gray points outside the red points indicate the location of the LYZ when only $\mu_\mathrm{B} = 0$ data is used. All points depicted from the lattice data have an acceptable p-value for the underlying Cosh-Padé and all jackknife samples that are in the same cluster.

Configs Used	**Real Part of μ/T**	**Imaginary Part of μ/T**
2.5M/1	4.65 ± 0.17	1.76 ± 0.04
2.5M/2	5.11 ± 0.55	1.92 ± 0.22
2.5M/4	4.45 ± 0.32	3.14 ± 0
2.5M/8	4.96 ± 1.42	3.14 ± 0
2.5M/16	4.53 ± 0.70	3.14 ± 0

Table 9.1 Locations of Lee-Yang zeros (LYZ) at $T = 145\,\mathrm{MeV}$ computed with progressively reduced statistics. The number of configurations used for fluctuation calculations was successively halved in each case, demonstrating the approach to the non critical base line in case of the low statistics. 3.14 ± 0 indicates the value is compatible with π up to machine precision ($\mathrm{Im}(x) = 0$).

by whether the values are exactly equal to π or not. This brute-force clustering condition can be employed because, as observed in Figure 9.3, the yellow π-region exhibits homogeneous constancy. This behavior is a direct consequence of the absence of an imaginary component in x within this domain. The minor errors observed in the data points belonging to each cluster further confirm that the clustering procedure was successfully applied at every temperature. The temperature independence of the imaginary part emerges as a natural consequence of the nHRG model's non-critical baseline character.

A comparison between the non-critical baseline and the LYZ extracted from lattice data reveals that outside the temperature range of 130-155 MeV, where the imaginary data is present, the lattice result is consistent with the baseline. The observation of lattice results consistent with such a noisy HRG baseline does not permit the exclusion of a critical endpoint (CEP). However, it may be interpreted as an indication that the limits of applicability of the current ansatz have been reached. It is also apparent that when insufficient statistics are available to distinguish from HRG, the extracted Lee-Yang zeros do not exhibit increasing errors but rather approach the non-critical baseline with minimal deviations. This phenomenon can be directly observed through progressive reduction of statistics, as demonstrated in Table 9.1.

If one where to use a [1,3]-Cosh-Padé the non-critical baseline would indeed drop to $\pi/3$ as can be seen in the histogram of all LYZ extracted from nHRG Figure 9.5. However, precise determination of the coefficient q_3 appearing in the term $(\cosh(\hat{\mu}_\mathrm{B}) - 1)^3$ would be required, which currently lies beyond what can be achieved with existing state-of-the-art lattice QCD simulations.

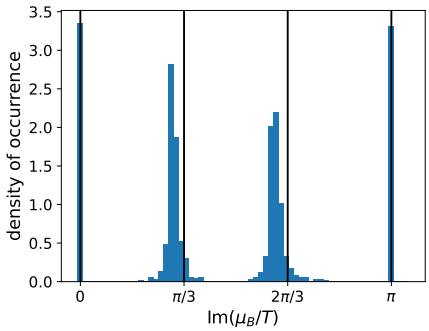

Figure 9.5 Histogram of the estimated LYZ location based only on the nHRG non critical Model with a [1,3]-Cosh-Padé fit.

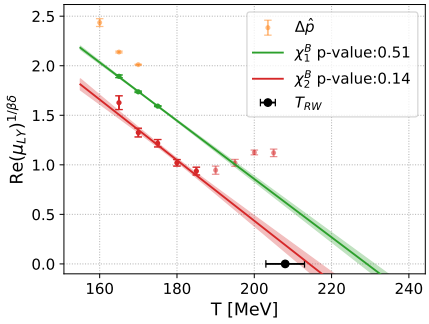

Figure 9.6 Extrapolations towards the Roberge-Weiss endpoint are shown based on the models of χ_1^B and χ_2^B, which, in contrast to the $\Delta\hat{p}$ model, yield acceptable p-values. For the data points based on χ_2^B, an artificial cutoff at $T = 185$ MeV is imposed.

9.4 Proof of concept via Roberge-Weiss endpoint

Before searching for the chiral critical endpoint, the idea of using the scaling relations of LYZ, as derived in chapter 3, can be demonstrated at the Roberge-Weiss endpoint. More precisely, in section 3.3 it was summarized that the LYZ associated with the RW endpoint should have an imaginary value exactly equal to π, while their real part is expected to scale according to Equation 3.34:

$$\mathrm{Re}(\hat{\mu}_{\mathrm{LY}}) = c\,(T_{RW} - T)^{\beta\delta}, \tag{9.4}$$

where c is a non-universal constant and T_{RW} denotes the temperature of the RW endpoint.
Indeed, the cosh-Padé ansatz yields an exact value of π for the imaginary part at high temperatures. Figure 9.6 shows the values of $\mathrm{Re}(\mu_{LY})^{1/\beta\delta}$ for high temperatures, where the underlying cosh-Padé ansatz could be successfully fitted to the $\mu_B = 0$ data. Furthermore, based on the scaling relation in Equation 9.4, the extrapolations used to extract T_{RW} are displayed.
Among these extrapolations, only those based the LYZ based on the modeling of χ_1^B and χ_2^B yield acceptable p-values. For χ_2^B, an additional cutoff at $T = 185$ MeV is imposed, corresponding to the first temperature at which the LYZ cease to decrease monotonically. This demonstrates the possibility of extracting the location of a critical point from the LYZ, but it also highlights the presence of systematic uncertainties as well as finite-size effects. Careful treatment of these systematics is therefore essential for a reliable analysis.

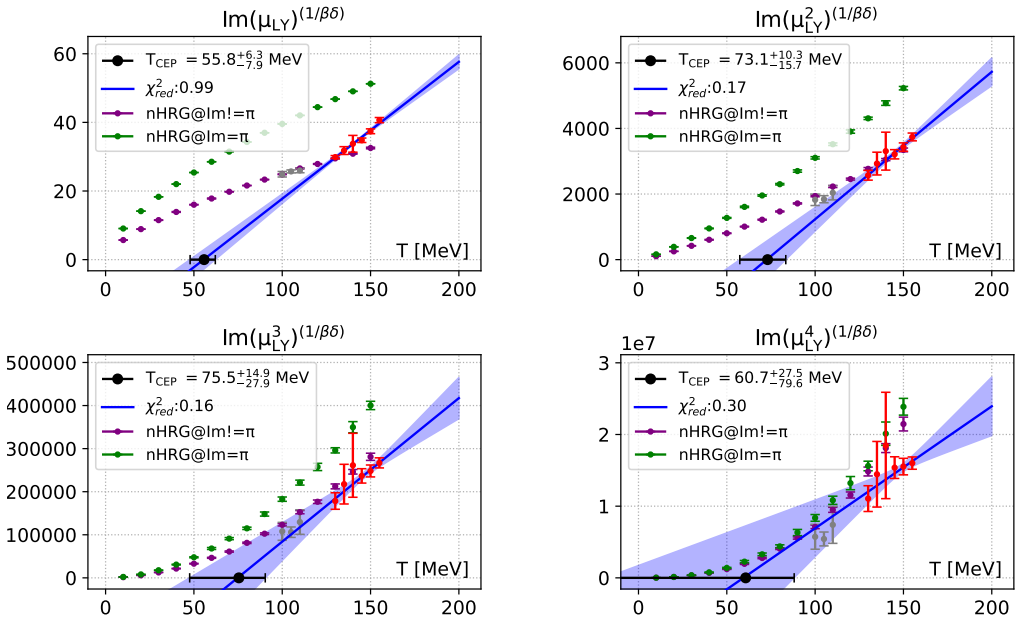

Figure 9.7 The critical endpoint temperature (T_{CEP}) is extrapolated using the four distinct ansätze from Eq. (3.19). All fits are found to yield high p-values, though different values for T_{CEP} are obtained. The non-critical baseline from the nHRG model is also included.

9.5 Systematics of the extrapolation to the CEP

Continuing on the chiral critical endpoint, if it exsit, the predicted scaling behavior of the LYZ near this critical point is given by Equation 3.16 and can be used for the extrapolation. However, current lattice data are restricted to regions far from the CEP, where Lee-Yang zeros remain distant from the real axis. To estimate the CEP location, an extrapolation to significantly lower temperatures is required. Given the substantial systematic uncertainties inherent in this long-range extrapolation, four distinct ansätze are employed and the temperature range is systematically varied.

9.5.1 Different scaling variables

The four distinct ansätze mentioned above are shown in Equation 3.19 and motivated in the containing section 3.1. While all ansätze share identical asymptotic critical behavior, their functional forms diverge in non-asymptotic regions, with no a priori justification for preferring any particular form.
Figure 9.7 show the four different extrapolation on the same data, with the nHRG baseline for reference. As discussed in section 9.3, the gray points corresponding to the non-critical baseline are excluded from the analysis. Across the entire remaining temperature range, the extrapolated critical endpoint temperature T_{CEP} and its corresponding uncertainties demonstrate significant sensitivity to the selected scaling variable. The obtained results indicate potential consistency with both the nuclear liquid-gas phase transition scenario and a high-temperature chiral critical endpoint. The restriction to four scaling variables, rather than including $\mathrm{Im}(\mu_{\mathrm{LY}}^5)$, is justified by the results shown in Figure 9.8. In this case, the fifth power amplifies the uncertainties to such a degree such that the extrapolation loses practical utility.

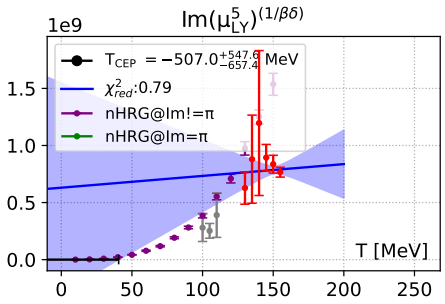

Figure 9.8 Extrapolation of the critical temperature using the a fifth ansatz, demonstrating the limit with regards to the exponent in the scaling variables based on the Noise of the LYZ's.

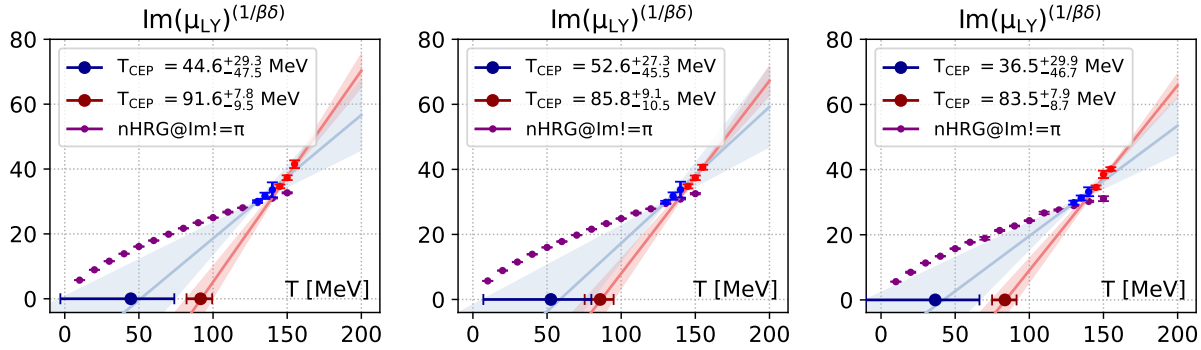

Figure 9.9 Impact of the selection of the temperature range on the location of T_{CEP} for the case of the three different ansätze $\Delta\hat{p}$ (left), χ_1 (middle) and χ_2 (right) from section 9.2 all with the scaling variable $\mathrm{Im}(\mu_B)$.

9.5.2 Temperature range

In addition to the systematic uncertainties from the scaling variables being taken into account, the impact of the temperature range is also considered. The maximum range from 130 to 155 MeV is divided into six intervals. Although only one degree of freedom is required by a linear fit, a minimum of two degrees of freedom is imposed for increased robustness. Consequently, at least four data points must be included in each fit. All possible connected ranges satisfying these criteria are examined, resulting in six ranges:
[130MeV, 145MeV], [135MeV, 150MeV], [140MeV, 155MeV], [130MeV, 150MeV], [135MeV, 155MeV], [130MeV, 155MeV].
This approach differs from conventional lattice field theory extrapolations, such as continuum limit determinations. In standard approaches, data points closer to the extrapolation target are systematically retained while more distant points are excluded, as proximity primarily increases statistical noise without introducing new systematic errors. In contrast, in the present analysis, each data point is itself derived from an extrapolation whose reliability is reduced at lower temperatures (i.e., greater proximity to the critical endpoint). This occurs because the extrapolation scheme is increasingly sensitive to baryon interactions as the temperature is decreased, thereby making the distinction between critical and non-critical behavior more difficult to establish. Consequently, while lower temperatures enable more reliable extrapolation toward the Lee-Yang edge singularity, significantly enhanced statistics are required to address the persistent sign problem in this regime. Without such improvements, systematic effects may occur in the analysis.
Taking this into account, Figure 9.9 depicts the influence of the fit range. Extrapolations are performed using both the three temperature points closest to the CEP and the three furthest data points, applied to all ansätze ($\Delta\hat{p}$, χ_1, and χ_2). Like the one from subsection 9.5.1, this source of systematics clearly introduces a significant amount of uncertainty and therefore also needs to be incorporated into the final analysis.

9.6 Final T_{CEP} analysis

In the final analysis, the systematic uncertainties introduced in the preceding sections are combined for determination of the critical temperature T_{CEP} at the Critical End Point (CEP)[79]. The following components are incorporated:

- 3 analytic continuation methods (Δp, χ_B^1, χ_B^2), see section 9.2
- 4 scaling ansätze ($\mathrm{Im}(\mu_{\mathrm{LY}}), \mathrm{Im}(\mu_{\mathrm{LY}}^2), \mathrm{Im}(\mu_{\mathrm{LY}}^3), \mathrm{Im}(\mu_{\mathrm{LY}}^4)$), see subsection 9.5.1
- 6 temperature ranges in the full range of [130MeV, 155MeV], see subsection 9.5.2

Each global fit with a specific combination of these choices constitutes an independent analysis. With k possible options for each choice, the total number of analyses scales by a factor of k. This results in $3 \times 4 \times 6 = 72$ distinct analyses. Additionally, each analysis incorporates $N_J + 1 = 49$ statistical samples through the Jackknife resampling method.
The multiple analysis variants can be combined to construct a unified probability distribution for the critical temperature T_{CEP}. While the jackknife resampling technique yields reliable uncertainty estimates for mean values, it does not provide direct access to the complete distribution of the mean. Consequently, each individual analysis result is modeled using a Gaussian distribution, a reasonable assumption due to the central limit theorem with the sufficiently large sample size of $N_J = 48$. The summation of individual CDFs from each analysis yields the combined CDF for T_{CEP}:

$$\mathrm{CDF}(T_{\mathrm{CEP}}) = \sum_i w_i N(T_{\mathrm{CEP}}; \mu_i, \sigma_i) = \sum_i w_i \frac{1}{2} \left(1 - \mathrm{erf} \left(\frac{\mu_i - T_{\mathrm{CEP}}}{\sqrt{2\sigma_i^2}} \right) \right), \tag{9.5}$$

with μ_j and σ_j being the mean and statistical uncertainty determined through jackknife analysis. The weight w_i associated with each analysis is taken as $w_i = 1/72$ (flat weighting), justified by all extrapolations producing acceptable p-values and the unnecessary complexity of alternative methods like the Akaike Information Criterion [80] for this study. To also incorporate statistics assuming Gaussian distributions for the individual fits with μ given by central sample and σ via jackknife error analysis.
Figure 9.10 displays the resulting CDF incorporating both statistical and systematic uncertainties (blue curve). The red curve shows the CDF considering only systematic variations, obtained by replacing the Gaussian distributions $N(T_{\mathrm{CEP}}; \mu_i, \sigma_i)$ with Heaviside step functions $\theta(\mu_i - T_{\mathrm{CEP}})$. The statistical error in the later CDF is indicated by the error bars. For visual reference, the left panel displays the corresponding histogram. It should be noted that the CDF is constructed independently from this histogram representation, thereby avoiding any binning artifacts. Both panels include markers indicating the location of the liquid-gas critical endpoint for comparison. The direct result obtained from the CDF is as follow:

$$T_{\mathrm{CEP}} = 68.8973 \pm 32.1451(\mathrm{stat.}) \pm 25.9845(\mathrm{sys.}) \tag{9.6}$$

This means based on the systematic part of the CDF that with 84% probability the critical endpoint either lies below $T = 103\,\mathrm{MeV}$ or does not exist. A non-negligible fraction of the T_{CEP} probability distribution is observed to lie within the very low-temperature region, indicating the possibility that the behavior of the LYZ could be a consequence of the nuclear liquid-gas critical endpoint.

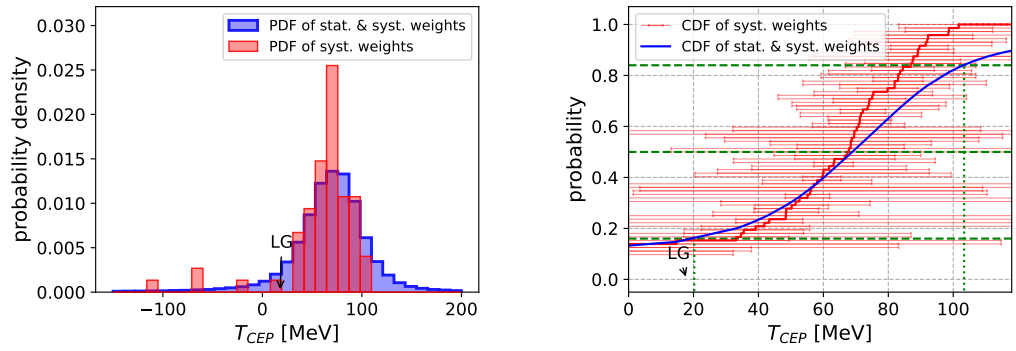

Figure 9.10 The histogram (left) indicating the probability density function and the cumulative distribution function (right) for the critical endpoint temperature T_{CEP} are shown, with the liquid-gas critical endpoint position marked as LG [33].

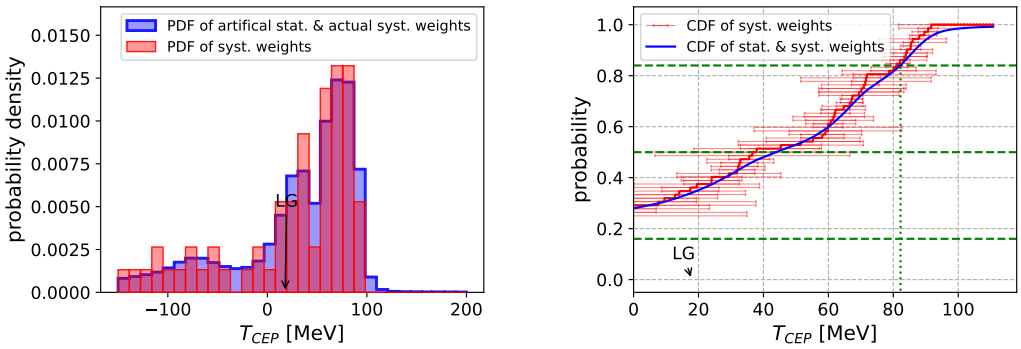

Figure 9.11 PDF and CDF of T_{CEP} with the same analysis as the on done for Figure 9.10 but with nHRG data using the relative error of the lattice.

9.6.1 Non-critical baseline

To estimate the significance of this result relative to a non-critical baseline, the complete analysis is repeated with the exact same sources of systematic uncertainty, but using data generated by the nHRG model. For this purpose, only the relative errors from the simulated fluctuation data at the corresponding temperatures were used in order to obtain a realistic statistical uncertainty. The probability density function (PDF) and cumulative distribution function (CDF) of T_{CEP} shown in Figure 9.10 are then reproduced, leading to Figure 9.11. The same limits on T_{CEP} are retained to allow for a direct comparison. One can clearly observe a wider spread in the systematic uncertainty but a reduced level of statistical noise. A significant peak at the same temperature as in the lattice data is, however, still present. This might suggest the conclusion that the peak observed in Figure 9.10 should not be trusted. Opposing this interpretation, however, is the significantly sharper distribution observed in the histogram.

To investigate whether specific systematic sources impact the analysis in unforeseen ways, a scatter plot is constructed in which the extracted values of T_{CEP} are shown against their corresponding p-values. Systematic variations are represented by the plotting style: the color encodes the choice of observable ansatz, while the marker shape denotes the scaling relation used for the extrapolation. For the nHRG distribution, a uniform spread with respect to the p-value can be observed. Concerning the contributions to negative values of T_{CEP}, only the $\mathrm{Im}(\mu^1)$ ansatz yields very low values, as expected from the investigation of the scaling variables in subsection 9.5.1. Apart from this, no further quantitative conclusions can be drawn regarding the nHRG case. In contrast, the scatter plot based on the real lattice data shows no apparent structure with respect to the

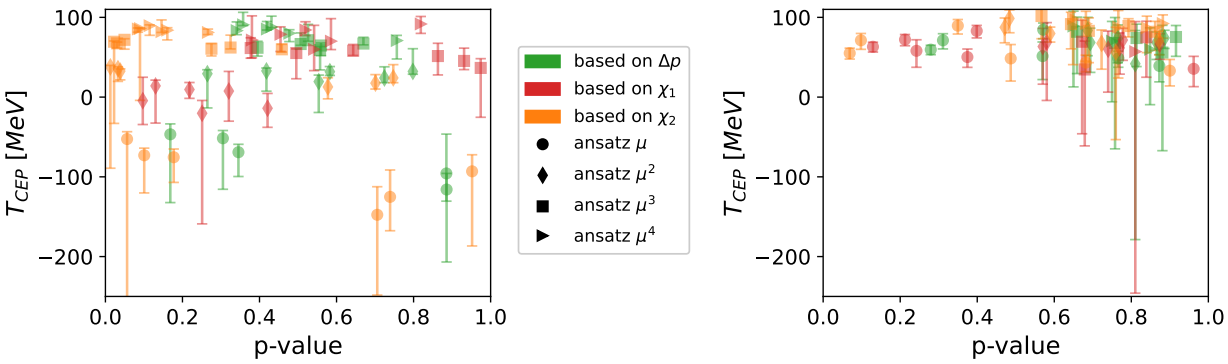

Figure 9.12 Scatter plots showing the location of each T_{CEP} obtained from the systematic analysis, with corresponding statistical errors, for both the analysis using lattice data (right) and the one using only nHRG data (left). The different sources of systematic are indicated using the marker and color, as described in the legend.

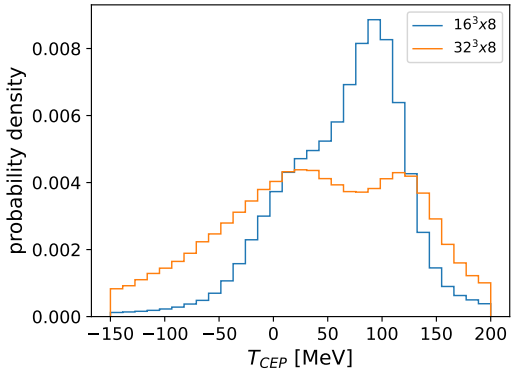

Figure 9.13 The histogram of critical endpoint temperature T_{CEP} based on using a $32^3 \times 8$ and $16^3 \times 8$ lattices with 4stout smearing. [33].

values of T_{CEP}. However, a significant shift of the p-values toward larger values is evident. Only the $\mathrm{Im}(\mu^1)$ ansatz yields p-values below 0.5, whereas all other scaling ansätze favor higher p-values. While this indicates that the fits were generally successful, it may also suggest that the statistical errors are overestimated for reasons not yet understood, resulting in a deviation from the expected uniform distribution.

9.6.2 Volume

To demonstrate why the volume dependence could not be incorporated into the systematic analyses, the analyses described thus far are performed on two datasets with reduced statistics and 4-stout smearing and lattice sizes of $32^3 \times 8$ and $16^3 \times 8$. Without going into details, challenges arose from the use of a dataset with reduced statistics. For example, the $16^3 \times 8$ lattice was unable to resolve the LYZ at a temperature of 155 MeV. Nonetheless Figure 9.13 depicts the smoothed PDF's of T_{CEP} , incorporating both statistical and systematic errors for both lattice volumes. It is clear that the $32^3 \times 8$ Lattice is unable to make any prediction on T_{CEP}.

10 Conclusion

This thesis aimed to identify potential signals of the chiral critical endpoint (CEP) in QCD. Using high-statistics lattice simulations provided by the Wuppertal-Budapest collaboration, employing 4HEX-improved staggered fermions on 16×8 lattices at zero and purely imaginary baryochemical potentials allowed for a reliable determination of baryon susceptibilities upto the tenth order for the first time. A successful splining using a χ^2 fitting procedure that properly accounted for statistical uncertainties via jackknife enabled extrapolations into the QCD phase diagram using the Equation of State.

This made possible a search for subtle signals in the QCD phase diagram, inspired by the critical fluctuations described by [19]. While the new data allowed for the observation of a possible signal indicating the presence of a CEP, the systematic uncertainty arising from the truncation of the Taylor expansion is too large to draw definitive conclusions.

Regarding the Lee-Yang theory analysis, a concise theoretical overview was presented, including a complete derivation of the leading-order scaling behavior of Lee-Yang zeros (LYZs) based on the finite-size scaling relations of the 3D Ising model. The method of Padé fits was discussed in detail, including their construction from Taylor series and their theoretical stability in the presence of statistical noise.

Using these Padé fits, the pressure difference between finite baryon density and zero density was successfully approximated over a temperature range starting from 130 MeV and extending beyond 200 MeV. Unlike traditional approaches, the rational approximation was performed not in μ_B or μ_B^2, but in the variable $\cosh(\mu_B) - 1$, which inherently respects charge conjugation and Roberge-Weiss symmetries.

With this ansatz, Lee-Yang zeros were successfully extracted. A comparison with a newly introduced non-critical baseline model, the nHRG (noisy Hadron Resonance Gas), revealed that only in the temperature range from 130 MeV to 155 MeV could the lattice data produce a discernible signal above the baseline. To further include systematic effects in the LYZ extraction, pressure derivatives were also fitted, though varying the Padé order was not feasible. This analysis showed that the real part of the LYZs is sensitive to systematic variations, while the imaginary part remains comparatively stable.

Using the derived scaling relations, the temperature of the CEP, T_CEP, was extracted from the LYZ data. Two additional sources of systematic uncertainty were incorporated: first, four different scaling variables were used, all of which exhibit the same asymptotic behavior near the critical point; second, six different temperature fit windows were employed, covering both high and low temperatures without bias.

Taking into account all 72 resulting ansätze, a combined cumulative distribution function (CDF) and corresponding probability density function (PDF) for T_CEP was produced. This distribution was then smeared further to incorporate statistical uncertainties into the systematic analysis. The main result is an upper limit on the value of T_CEP: Based on the CDF incorporating both statistical and systematic errors the T_CEP lies below approximately 103 MeV with 84% probability, or the CEP does not exist.

To get a reference for this result, the same analysis was repeated using the nHRG model, employing the relative errors from the corresponding lattice data. While the nHRG derived PDF for T_CEP differs from the lattice-based PDF, most notably by lacking a sharp peak and assigning a larger probability to unphysical (negative) T_CEP values, a significant probability is assigned to a non negative value of T_CEP Overall, this thesis demonstrates that the method is highly sensitive to systematic effects. The Padé expansion in the variable $\cosh(\mu_B) - 1$ underlines the importance of carefully comparing to a non-critical baseline when searching for signals of the CEP. As an outlook, successfully fitting higher-order Padé's could provide more systematic control and reduce the influence of the non-critical baseline. This may allow for the detection of CEP signals at temperatures closer to its theoretically expected location. However, achieving this would require significantly more computational resources than the currently state-of-the-art lattice simulations.

Part IV

Appendix

A Theory Appendix

A.1 Derivation ABCD

To derive expressions for A, B, C, D, rewrite the logarithm containing the eigenvalues $\xi_i = \xi_i[m, U]$ to make the derivatives easier to compute:

$$\log\left[\frac{\xi_i - e^{\hat{\mu}}}{\xi_i - 1}\right] = \log\left[\frac{\xi_i - 1 + 1 - e^{\hat{\mu}}}{\xi_i - 1}\right] = \log\left[1 - \frac{1 - e^{\hat{\mu}}}{\xi_i - 1}\right]. \tag{A.1}$$

With this it is strait forward to compute the derivatives at $\hat{\mu} = 0$:

$$\begin{aligned}
\frac{\partial}{\partial\hat{\mu}}\bigg|_{\hat{\mu}=0} \log\left[1 - \frac{1 - e^{\hat{\mu}}}{\xi_i - 1}\right] &= \frac{e^{\hat{\mu}}}{-\xi_i + e^{\hat{\mu}}}\bigg|_{\hat{\mu}=0} = \frac{1}{1 - \xi_i} \\
\frac{\partial^2}{\partial\hat{\mu}^2}\bigg|_{\hat{\mu}=0} \log\left[1 - \frac{1 - e^{\hat{\mu}}}{\xi_i - 1}\right] &= \frac{-\xi_i e^{\hat{\mu}}}{(-\xi_i + e^{\hat{\mu}})^2}\bigg|_{\hat{\mu}=0} = \frac{-\xi_i}{(1 - \xi_i)^2} \\
\frac{\partial^3}{\partial\hat{\mu}^3}\bigg|_{\hat{\mu}=0} \log\left[1 - \frac{1 - e^{\hat{\mu}}}{\xi_i - 1}\right] &= \frac{-\xi_i e^{\hat{\mu}}(\xi_i + e^{\hat{\mu}})}{(-\xi_i + e^{\hat{\mu}})^3}\bigg|_{\hat{\mu}=0} = \frac{\xi_i(\xi_i + 1)}{(1 - \xi_i)^3} \\
\frac{\partial^4}{\partial\hat{\mu}^4}\bigg|_{\hat{\mu}=0} \log\left[1 - \frac{1 - e^{\hat{\mu}}}{\xi_i - 1}\right] &= \frac{-\xi_i e^{\hat{\mu}}(\xi_i^2 + 4\xi_i e^{\hat{\mu}} + e^{2\hat{\mu}})}{(-\xi_i + e^{\hat{\mu}})^4}\bigg|_{\hat{\mu}=0} = \frac{-\xi_i(\xi_i^2 + 4\xi_i + 1)}{(1 - \xi_i)^4}
\end{aligned} \tag{A.2}$$

Considering now Equation 4.14, the n-th derivative of the left-hand side is directly identified as A, B, C, and D for $n = 1, 2, 3, 4$, respectively, as follows from Equation 4.9, where the factorial factors cancel with those from the power rule. On the right-hand side, only the sum of logarithms remains for $n \geq 2$ (the $n = 1$ case having been shown in the main text), with the derivatives of the individual summands already calculated above. Taking into account that the odd terms in the Taylor series of $\log\det M$ $(A, C, \dots)$ must be purely imaginary, while the even ones $(B, D, \dots)$ are real, the following explicit expressions are obtained:

$$\begin{aligned}
A &= \frac{i}{4}\mathrm{Im}\sum_i \frac{1}{(1 - \xi_i)} \\
B &= \frac{1}{4}\mathrm{Re}\sum_i \frac{-\xi_i}{(1 - \xi_i)^2}, \\
C &= \frac{i}{4}\mathrm{Im}\sum_i \frac{\xi_i(1 + \xi_i)}{(1 - \xi_i)^3}, \\
D &= \frac{1}{4}\mathrm{Re}\sum_i \frac{-\xi_i(\xi_i^2 + 4\xi_i + 1)}{(1 - \xi_i)^4}
\end{aligned} \tag{A.3}$$

These expressions agree with those reported in [61], except for a missing sign in D.

B Method Appendix

B.1 Statistics

T [MeV]	β	m_l	m_s	# configurations at $\mu_B = i\pi(j/8)$								
	$16^3 \times 8$ lattice			$j=0$	$j=1$	$j=2$	$j=3$	$j=4$	$j=5$	$j=6$	$j=7$	$j=8$
100	0.4846	0.00490631	0.1355610	915010	-	-	-	-	-	-	-	-
105	0.5050	0.00458740	0.1267500	894220	-	-	-	-	-	-	-	-
110	0.5236	0.00432111	0.1193920	760795	-	-	-	-	-	-	-	-
115	0.5406	0.00409845	0.1132400	1054502	-	-	-	-	-	-	-	-
120	0.5560	0.00390982	0.1080280	1082567	-	-	-	-	-	-	-	-
125	0.5700	0.00374705	0.1035310	1726868	-	-	-	-	-	-	-	-
130	0.5829	0.00360381	0.0995733	2132329	-	96440	-	96082	-	95775	-	95625
135	0.5947	0.00347548	0.0960274	1453169	110859	105287	104348	120205	103744	103749	103196	103084
140	0.6056	0.00335869	0.0928007	4010320	99904	105232	104911	359058	103501	99483	102589	113865
145	0.6158	0.00325107	0.0898270	2579944	106703	106386	105027	121944	103958	103239	102471	115049
150	0.6252	0.00315088	0.0870590	1688860	114258	114018	112067	117290	109804	97932	96239	109087
155	0.6341	0.00305689	0.0844619	1623503	109132	108649	107158	125765	104061	102762	101464	115855
160	0.6425	0.00296817	0.0820105	2229437	112026	111086	108615	128345	104466	95570	101203	108589
165	0.6504	0.00288403	0.0796857	1768242	103692	101652	89855	121047	95726	92934	86765	105389
170	0.6579	0.00280394	0.0774727	1204210				-				
175	0.6651	0.00272748	0.0753604	1602383				-				
180	0.6719	0.00265434	0.0733394	1357330				-				
185	0.6785	0.00258424	0.0714026	855048				-				
190	0.6848	0.00251696	0.0695436	318710				-				
195	0.6909	0.00245231	0.0677573	362672				-				
200	0.6968	0.00239013	0.0660393	324768				-				
205	0.7025	0.00233028	0.0643856	159500				-				
210	0.7080	0.00227263	0.0627928	260084				-				
220	0.7188	0.00216352	0.0597782	249068				-				
230	0.7290	0.00206205	0.0569745	257480				-				
240	0.7389	0.00196759	0.0543644	270856				-				
250	0.7485	0.00187961	0.0519336	430495				-				
260	0.7580	0.00179768	0.0496700	281616				-				
280	0.7765	0.00165052	0.0456040	289961				-				
300	0.7946	0.00152351	0.0420946	297512				-				

Table B.1 Simulation parameters and statistics of the used ensembles. The configurations were separated by 20 RHMC updates. On each configuration a full eigenvalue analysis has been carried out at both the light and strange masses.[65]

B.2 Padé-Code

```
# Computes a prefactor arising from taking the derivative in padeMulti
function prefactor(up,down)
    u , d = up-1 , down+1
    if u<d return 1 else return prod(u:-1:d) end
end
#Function which generates the system of linear equations(Matrix M)
# which need to be solved in order to get the Pade coefficients:
# Pade_coeff = M \ Taylor_coeffs
# x : keys(x) expansions points
#   : values(x) vector containing the evaluared derivatives
function constructorM_pade_MP(m,n,x::Dict{Number,Vector})
    totalNumOfDiffs=sum([length(diffVals) for (loc,diffVals) in x])
    M=zeros(ComplexF64,m+n+1,m+n+1)
    i=0
    for (loc,diffVals) in x
        for k in 0:(length(diffVals)-1)
            i+=1
            for j in (k+1):(m+1) #P
                M[i,j]=prefactor(j,j-k-1)*loc^(j-k-1)
            end
            for l in 0:k #Q
                if l==0 minexp=1 else minexp=0 end
                minexp , maxexp , fdiff = 1-l , n-l , k-l
                pref = diffVals[fdiff+1]*binomial(k,l)
                place=1
                for exponent in minexp:maxexp
                    if exponent<0 place+=1 ; continue end
                    M[i,place+m+1] -= pref*prefactor(place+1,exponent)*
                                      loc^(exponent)
                    place+=1
                end
            end
        end
    end
    return M
end
```

Quellcode B.1 Julia code used for the construction of the algebraic from Taylor coefficients to Padé coefficients

Bibliography

[1] Kenneth G. Wilson. "Confinement of quarks". In: *Phys. Rev. D* 10 (8 Oct. 1974), pp. 2445–2459. DOI: 10.1103/PhysRevD.10.2445. URL: https://link.aps.org/doi/10.1103/PhysRevD.10.2445.

[2] David J. Gross and Frank Wilczek. "Asymptotically Free Gauge Theories. I". In: *Phys. Rev. D* 8 (10 Nov. 1973), pp. 3633–3652. DOI: 10.1103/PhysRevD.8.3633. URL: https://link.aps.org/doi/10.1103/PhysRevD.8.3633.

[3] Roman Pasechnik and Michal umbera. "Phenomenological Review on QuarkGluon Plasma: Concepts vs. Observations". In: *Universe* 3.1 (2017), p. 7. DOI: 10.3390/universe3010007. arXiv: 1611.01533 [hep-ph].

[4] K. Adcox et al. "Formation of dense partonic matter in relativistic nucleus-nucleus collisions at RHIC: Experimental evaluation by the PHENIX collaboration". In: *Nucl. Phys. A* 757 (2005), pp. 184–283. DOI: 10.1016/j.nuclphysa.2005.03.086. arXiv: nucl-ex/0410003.

[5] J. Schukraft. "First Results from the ALICE experiment at the LHC". In: *Nuclear Physics A* 862863 (July 2011), pp. 78–84. ISSN: 0375-9474. DOI: 10.1016/j.nuclphysa.2011.05.023. URL: http://dx.doi.org/10.1016/j.nuclphysa.2011.05.023.

[6] H. Sazdjian. "Introduction to chiral symmetry in QCD". In: *EPJ Web of Conferences* 137 (2017). Ed. by Y. Foka, N. Brambilla, and V. Kovalenko, p. 02001. ISSN: 2100-014X. DOI: 10.1051/epjconf/201713702001. URL: http://dx.doi.org/10.1051/epjconf/201713702001.

[7] Jana N Guenther. "Overview of the QCD phase diagram: Recent progress from the lattice". en. In: *Eur. Phys. J. A* 57.4 (Apr. 2021), p. 136.

[8] Szabolcs Borsányi et al. "Is there still any T c mystery in lattice QCD? Results with physical masses in the continuum limit III". In: *Journal of High Energy Physics* 2010.9 (Sept. 2010). ISSN: 1029-8479. DOI: 10.1007/jhep09(2010)073. URL: http://dx.doi.org/10.1007/JHEP09(2010)073.

[9] Y. Aoki et al. "The order of the quantum chromodynamics transition predicted by the standard model of particle physics". In: *Nature* 443.7112 (Oct. 2006), pp. 675–678. ISSN: 1476-4687. DOI: 10.1038/nature05120. URL: http://dx.doi.org/10.1038/nature05120.

[10] Gregg Jaeger. "The Ehrenfest classification of phase transitions: Introduction and evolution". In: *Arch. Hist. Exact Sci.* 53.1 (May 1998), pp. 51–81.

[11] Robert B. Griffiths. "Dependence of Critical Indices on a Parameter". In: *Phys. Rev. Lett.* 24 (26 June 1970), pp. 1479–1482. DOI: 10.1103/PhysRevLett.24.1479. URL: https://link.aps.org/doi/10.1103/PhysRevLett.24.1479.

[12] Mikhail Stephanov. *QCD critical point: recent developments*. 2024. arXiv: 2410.02861 [nucl-th]. URL: https://arxiv.org/abs/2410.02861.

[13] Philippe de Forcrand. *Simulating QCD at finite density*. 2010. arXiv: 1005.0539 [hep-lat]. URL: https://arxiv.org/abs/1005.0539.

[14] C. N. Yang and T. D. Lee. "Statistical Theory of Equations of State and Phase Transitions. I. Theory of Condensation". In: *Phys. Rev.* 87 (3 Aug. 1952), pp. 404–409. DOI: 10.1103/PhysRev.87.404. URL: https://link.aps.org/doi/10.1103/PhysRev.87.404.

[15] T. D. Lee and C. N. Yang. "Statistical Theory of Equations of State and Phase Transitions. II. Lattice Gas and Ising Model". In: *Phys. Rev.* 87 (3 Aug. 1952), pp. 410–419. DOI: 10.1103/PhysRev.87.410. URL: https://link.aps.org/doi/10.1103/PhysRev.87.410.

[16] Michael E. Fisher and Michael N. Barber. “Scaling Theory for Finite-Size Effects in the Critical Region”. In: *Phys. Rev. Lett.* 28 (23 June 1972), pp. 1516–1519. DOI: 10.1103/PhysRevLett.28.1516. URL: https://link.aps.org/doi/10.1103/PhysRevLett.28.1516.

[17] David A. Clarke et al. *Searching for the QCD critical endpoint using multi-point Padé approximations*. 2024. arXiv: 2405.10196 [hep-lat]. URL: https://arxiv.org/abs/2405.10196.

[18] D. Bollweg et al. “Taylor expansions and Padé approximants for cumulants of conserved charge fluctuations at nonvanishing chemical potentials”. In: *Physical Review D* 105.7 (Apr. 2022). ISSN: 2470-0029. DOI: 10.1103/physrevd.105.074511. URL: http://dx.doi.org/10.1103/PhysRevD.105.074511.

[19] M. A. Stephanov. “Non-Gaussian fluctuations near the QCD critical point”. In: *Phys. Rev. Lett.* 102 (2009), p. 032301. DOI: 10.1103/PhysRevLett.102.032301. arXiv: 0809.3450 [hep-ph].

[20] Szabolcs Borsányi. *Das Standardmodell der Elementarteilchenphysik*. Lecture notes. 2024.

[21] Volker Koch. *Introduction to Chiral Symmetry*. 1995. arXiv: nucl-th/9512029 [nucl-th]. URL: https://arxiv.org/abs/nucl-th/9512029.

[22] Claudia Ratti and Rene Bellwied. *The deconfinement transition of QCD*. en. 1st ed. Lecture notes in physics. Cham, Switzerland: Springer Nature, June 2021.

[23] S. Navas et al. “Review of particle physics”. In: *Phys. Rev. D* 110.3 (2024), p. 030001. DOI: 10.1103/PhysRevD.110.030001.

[24] KIERAN HOLLAND and UWE-JENS WIESE. “THE CENTER SYMMETRY AND ITS SPONTANEOUS BREAKDOWN AT HIGH TEMPERATURES”. In: *At The Frontier of Particle Physics*. WORLD SCIENTIFIC, Apr. 2001, pp. 1909–1944. ISBN: 9789812810458. DOI: 10.1142/9789812810458_0040. URL: http://dx.doi.org/10.1142/9789812810458_0040.

[25] Jeff Greensite. *An introduction to the confinement problem*. en. 2nd ed. Lecture notes in physics. Cham, Switzerland: Springer Nature, Aug. 2020.

[26] Larry D. McLerran and Benjamin Svetitsky. “A Monte Carlo study of SU(2) Yang-Mills theory at finite temperature”. In: *Physics Letters B* 98.3 (1981), pp. 195–198. ISSN: 0370-2693. DOI: https://doi.org/10.1016/0370-2693(81)90986-2. URL: https://www.sciencedirect.com/science/article/pii/0370269381909862.

[27] André Roberge and Nathan Weiss. “Gauge theories with imaginary chemical potential and the phases of QCD”. en. In: *Nucl. Phys. B*. 275.4 (Dec. 1986), pp. 734–745.

[28] Claudio Bonati et al. “Roberge-Weiss endpoint and chiral symmetry restoration in QCD”. In: *Physical Review D* 99.1 (Jan. 2019). ISSN: 2470-0029. DOI: 10.1103/physrevd.99.014502. URL: http://dx.doi.org/10.1103/PhysRevD.99.014502.

[29] Rajeev S. Bhalerao. *Relativistic heavy-ion collisions*. 2014. arXiv: 1404.3294 [nucl-th]. URL: https://arxiv.org/abs/1404.3294.

[30] M. A. Stephanov. *QCD phase diagram: an overview*. 2006. arXiv: hep-lat/0701002 [hep-lat]. URL: https://arxiv.org/abs/hep-lat/0701002.

[31] Szabolcs Borsányi et al. “Is there still any T c mystery in lattice QCD? Results with physical masses in the continuum limit III”. en. In: *J. High Energy Phys.* 2010.9 (Sept. 2010).

[32] A Bazavov et al. “Chiral and deconfinement aspects of the QCD transition”. In: *Phys. Rev.* 85.5 (Mar. 2012).

[33] J. B. Elliott et al. “Determination of the coexistence curve, critical temperature, density, and pressure of bulk nuclear matter from fragment emission data”. In: *Phys. Rev. C* 87.5 (2013), p. 054622. DOI: 10.1103/PhysRevC.87.054622.

[34] Adam Bzdak et al. “Mapping the phases of quantum chromodynamics with beam energy scan”. In: *Physics Reports* 853 (Apr. 2020), pp. 1–87. ISSN: 0370-1573. DOI: 10.1016/j.physrep.2020.01.005. URL: http://dx.doi.org/10.1016/j.physrep.2020.01.005.

[35] Claudio Bonati et al. “Roberge-Weiss endpoint at the physical point of $N_f = 2+1$ QCD”. In: *Phys. Rev. D* 93.7 (2016), p. 074504. DOI: 10.1103/PhysRevD.93.074504. arXiv: 1602.01426 [hep-lat].

[36] C. Schmidt et al. “Detecting Critical Points from the LeeYang Edge Singularities in Lattice QCD”. In: *Acta Physica Polonica B Proceedings Supplement* 16.1 (2023), p. 1. ISSN: 2082-7865. DOI: 10.5506/aphyspolbsupp.16.1-a52. URL: http://dx.doi.org/10.5506/APhysPolBSupp.16.1-A52.

[37] Shinji Ejiri et al. “Study of QCD Thermodynamics at Finite Density by Taylor Expansion”. In: *Progress of Theoretical Physics Supplement* 153 (2004), pp. 118–126. ISSN: 0375-9687. DOI: 10.1143/ptps.153.118. URL: http://dx.doi.org/10.1143/PTPS.153.118.

[38] Francesco Di Renzo, Marco Aliberti, and Petros Dimopoulos. *On analytic continuation from imaginary to real chemical potential in Lattice QCD*. 2025. arXiv: 2502.03392 [hep-lat]. URL: https://arxiv.org/abs/2502.03392.

[39] Misha A. Stephanov, K. Rajagopal, and Edward V. Shuryak. “Signatures of the tricritical point in QCD”. In: *Phys. Rev. Lett.* 81 (1998), pp. 4816–4819. DOI: 10.1103/PhysRevLett.81.4816. arXiv: hep-ph/9806219.

[40] Boris Berdnikov and Krishna Rajagopal. “Slowing out-of-equilibrium near the QCD critical point”. In: *Phys. Rev. D* 61 (2000), p. 105017. DOI: 10.1103/PhysRevD.61.105017. arXiv: hep-ph/9912274.

[41] M. A. Stephanov. “On the sign of kurtosis near the QCD critical point”. In: *Phys. Rev. Lett.* 107 (2011), p. 052301. DOI: 10.1103/PhysRevLett.107.052301. arXiv: 1104.1627 [hep-ph].

[42] R. Hagedorn. “Statistical thermodynamics of strong interactions at high-energies”. In: *Nuovo Cim. Suppl.* 3 (1965), pp. 147–186.

[43] Vladimir Skokov. “Two lectures on Yang-Lee edge singularity and analytic structure of QCD equation of state”. In: *SciPost Physics Lecture Notes* (Mar. 2025). ISSN: 2590-1990. DOI: 10.21468/scipostphyslectnotes.91. URL: http://dx.doi.org/10.21468/SciPostPhysLectNotes.91.

[44] Simran Singh. “Unconventional probes into the QCD phase diagram using Rational approximations and Lefschetz thimbles”. PhD thesis. Parma U., 2022.

[45] Michael E. Fisher. “Yang-Lee Edge Singularity and ϕ^3 Field Theory”. In: *Phys. Rev. Lett.* 40 (25 June 1978), pp. 1610–1613. DOI: 10.1103/PhysRevLett.40.1610. URL: https://link.aps.org/doi/10.1103/PhysRevLett.40.1610.

[46] M. A. Stephanov. “QCD critical point and complex chemical potential singularities”. In: *Physical Review D* 73.9 (May 2006). ISSN: 1550-2368. DOI: 10.1103/physrevd.73.094508. URL: http://dx.doi.org/10.1103/PhysRevD.73.094508.

[47] Gokce Basar. *On the QCD critical point, Lee-Yang edge singularities and Pade resummations*. 2024. arXiv: 2312.06952 [hep-th]. URL: https://arxiv.org/abs/2312.06952.

[48] John Cardy. *Scaling and Renormalization in Statistical Physics*. Cambridge Lecture Notes in Physics. Cambridge University Press, 1996.

[49] Cyuan-Han Chang et al. “Bootstrapping the 3d Ising stress tensor”. In: *Journal of High Energy Physics* 2025.3 (Mar. 2025). ISSN: 1029-8479. DOI: 10.1007/jhep03(2025)136. URL: http://dx.doi.org/10.1007/JHEP03(2025)136.

[50] Paolo Parotto et al. “QCD equation of state matched to lattice data and exhibiting a critical point singularity”. In: *Physical Review C* 101.3 (Mar. 2020). ISSN: 2469-9993. DOI: 10.1103/physrevc.101.034901. URL: http://dx.doi.org/10.1103/PhysRevC.101.034901.

[51] C. Itzykson, R.B. Pearson, and J.B. Zuber. “Distribution of zeros in Ising and gauge models”. In: *Nuclear Physics B* 220.4 (1983), pp. 415–433. ISSN: 0550-3213. DOI: https://doi.org/10.1016/0550-3213(83)90499-6. URL: https://www.sciencedirect.com/science/article/pii/0550321383904996.

[52] X. An, D. Mesterházy, and M. A. Stephanov. “Functional renormalization group approach to the Yang-Lee edge singularity”. In: *Journal of High Energy Physics* 2016.7 (July 2016). ISSN: 1029-8479. DOI: 10.1007/jhep07(2016)041. URL: http://dx.doi.org/10.1007/JHEP07(2016)041.

[53] Peter J. Kortman and Robert B. Griffiths. “Density of Zeros on the Lee-Yang Circle for Two Ising Ferromagnets”. In: *Phys. Rev. Lett.* 27 (21 Nov. 1971), pp. 1439–1442. DOI: 10.1103/PhysRevLett.27.1439. URL: https://link.aps.org/doi/10.1103/PhysRevLett.27.1439.

[54] P. Dimopoulos et al. “Contribution to understanding the phase structure of strong interaction matter: Lee-Yang edge singularities from lattice QCD”. In: *Physical Review D* 105.3 (Feb. 2022). ISSN: 2470-0029. DOI: 10.1103/physrevd.105.034513. URL: http://dx.doi.org/10.1103/PhysRevD.105.034513.

[55] Christof Gattringer and Christian B. Lang. *Quantum chromodynamics on the lattice*. Vol. 788. Berlin: Springer, 2010. ISBN: 978-3-642-01850-3. DOI: 10.1007/978-3-642-01850-3.

[56] Stefano Capitani, Stephan Dürr, and Christian Hoelbling. “Rationale for UV-filtered clover fermions”. In: *Journal of High Energy Physics* 2006.11 (Nov. 2006), pp. 028–028. ISSN: 1029-8479. DOI: 10.1088/1126-6708/2006/11/028. URL: http://dx.doi.org/10.1088/1126-6708/2006/11/028.

[57] TARO Collaboration and Ph. de Forcrand et al. *Renormalization Group Flow of SU(3) Gauge Theory*. 1998. arXiv: hep-lat/9806008 [hep-lat]. URL: https://arxiv.org/abs/hep-lat/9806008.

[58] Szabolcs Borsanyi et al. “Continuum-extrapolated high-order baryon fluctuations”. In: *Phys. Rev. D* 110.1 (2024), p. L011501. DOI: 10.1103/PhysRevD.110.L011501. arXiv: 2312.07528 [hep-lat].

[59] Szabolcs Borsányi et al. “High-precision scale setting in lattice QCD”. In: *JHEP* 09 (2012), p. 010. DOI: 10.1007/JHEP09(2012)010. arXiv: 1203.4469 [hep-lat].

[60] C. R. Allton et al. “Thermodynamics of two flavor QCD to sixth order in quark chemical potential”. In: *Physical Review D* 71.5 (Mar. 2005). ISSN: 1550-2368. DOI: 10.1103/physrevd.71.054508. URL: http://dx.doi.org/10.1103/PhysRevD.71.054508.

[61] Szabolcs Borsanyi et al. *QCD deconfinement transition line up to $\mu_B = 400$ MeV from finite volume lattice simulations*. 2024. arXiv: 2410.06216 [hep-lat]. URL: https://arxiv.org/abs/2410.06216.

[62] A. Hasenfratz and D. Toussaint. “Canonical ensembles and nonzero density quantum chromodynamics”. In: *Nuclear Physics B* 371.1 (1992), pp. 539–549. ISSN: 0550-3213. DOI: https://doi.org/10.1016/0550-3213(92)90247-9. URL: https://www.sciencedirect.com/science/article/pii/0550321392902479.

[63] M. Giordano et al. “Radius of convergence in lattice QCD at finite μ_B with rooted staggered fermions”. In: *Phys. Rev. D* 101 (7 Apr. 2020), p. 074511. DOI: 10.1103/PhysRevD.101.074511. URL: https://link.aps.org/doi/10.1103/PhysRevD.101.074511.

[64] Philippe de Forcrand. *The Sign Problem in Lattice QCD*. Talk, INT-13-2a, Advances in Quantum Monte Carlo. Available online (PDF). July 2013.

[65] Alexander Adam et al. “High-precision baryon number cumulants from lattice QCD in a finite box: cumulant ratios, Lee-Yang zeros and critical endpoint predictions”. In: (July 2025). arXiv: 2507.13254 [hep-lat].

[66] George A Baker. *Essentials of padé approximants*. en. San Diego, CA: Academic Press, Mar. 1975.

[67] Alan Jeffrey. *Complex analysis and applications, second edition*. 2nd ed. London, England: Chapman and Hall, Dec. 2004.

[68] Avery McIntosh. *The Jackknife Estimation Method*. 2016. arXiv: 1606.00497 [stat.ME]. URL: https://arxiv.org/abs/1606.00497.

[69] Faizan G Mohammad and Will J Percival. “Creating jackknife and bootstrap estimates of the covariance matrix for the two-point correlation function”. In: *Monthly Notices of the Royal Astronomical Society* 514.1 (May 2022), pp. 1289–1301. ISSN: 0035-8711. DOI: 10.1093/mnras/stac1458. eprint: https://academic.oup.com/mnras/article-pdf/514/1/1289/43986041/stac1458.pdf. URL: https://doi.org/10.1093/mnras/stac1458.

[70] Bradley Efron. *The jackknife, the bootstrap and other resampling plans*. Society for Industrial and Applied Mathematics, Jan. 1982.

[71] Carl De Boor. *A practical guide to splines*. en. 1st ed. Applied Mathematical Sciences. New York, NY: Springer, Nov. 2001.

[72] Sebastian Stock. *BSplines: A Julia package for working with B-splines*. https://github.com/sostock/BSplines.jl. 2022.

[73] Raine Yeh et al. “Fast Automatic Knot Placement Method for Accurate B-spline Curve Fitting”. In: *Computer-Aided Design* 128 (2020), p. 102905. ISSN: 0010-4485. DOI: https://doi.org/10.1016/j.cad.2020.102905. URL: https://www.sciencedirect.com/science/article/pii/S0010448520300981.

[74] Szabolcs Borsányi et al. “Chiral versus deconfinement properties of the QCD crossover: Differences in the volume and chemical potential dependence from the lattice”. In: *Phys. Rev. D* 111.1 (2025), p. 014506. DOI: 10.1103/PhysRevD.111.014506.

[75] Wei-jie Fu et al. “Hyper-order baryon number fluctuations at finite temperature and density”. In: *Phys. Rev. D* 104.9 (2021), p. 094047. DOI: 10.1103/PhysRevD.104.094047. arXiv: 2101.06035 [hep-ph].

[76] Yi Lu et al. “Finite density signatures of confining and chiral dynamics in QCD thermodynamics and fluctuations of conserved charges”. In: (Apr. 2025). arXiv: 2504.05099 [hep-ph].

[77] V. Vovchenko, V. V. Begun, and M. I. Gorenstein. “Hadron multiplicities and chemical freeze-out conditions in proton-proton and nucleus-nucleus collisions”. In: *Phys. Rev.* C93.6 (2016), p. 064906. DOI: 10.1103/PhysRevC.93.064906. arXiv: 1512.08025 [nucl-th].

[78] Szabolcs Borsanyi et al. “The QCD crossover at finite chemical potential from lattice simulations”. In: *Phys. Rev. Lett.* 125 (2020), p. 052001. arXiv: 2002.02821 [hep-lat].

[79] Sz. Borsanyi et al. “Leading hadronic contribution to the muon magnetic moment from lattice QCD”. In: *Nature* 593.7857 (2021), pp. 51–55. DOI: 10.1038/s41586-021-03418-1. arXiv: 2002.12347 [hep-lat].

[80] H. Akaike. “A new look at the statistical model identification”. In: *IEEE Transactions on Automatic Control* 19.6 (1974), pp. 716–723. DOI: 10.1109/TAC.1974.1100705.

c

Erklärungen

Eidesstattliche Erklärung

Hiermit erkläre ich, dass ich die von mir eingereichte Abschlussarbeit selbständig verfasst und keine anderen als die angegebenen Quellen und Hilfsmittel benutzt sowie Stellen der Abschlussarbeit, die anderen Werken dem Wortlaut oder Sinn nach entnommen wurden, in jedem Fall unter Angabe der Quelle als Entlehnung kenntlich gemacht habe.

Ort / Datum

Unterschrift

Einverständniserklärung

Hiermit erkläre ich mich damit einverstanden, dass meine Abschlussarbeit wissenschaftlich interessierten Personen oder Institutionen und im Rahmen von externen QualitätssicherungsmaSSnahmen des Studienganges zur Einsichtnahme zur Verfügung gestellt werden kann.
Korrektur- oder Bewertungshinweise in meiner Arbeit dürfen nicht zitiert werden.

Ort / Datum

Unterschrift